Converting Carbon Dioxide into Value Added Chemicals via Low Temperature Atmospheric Pressure Plasmas

Alexander Foote

Doctor of Philosophy

University of York
Physics

June 2018

Abstract

Carbon dioxide is a waste product produced extensively by modern everyday life. In order to combat the growing threat of climate change atmospheric carbon dioxide levels need to be reduced and controlled. If waste carbon dioxide can be converted effectively and efficiently on a commercial basis into valuable chemicals atmospheric carbon dioxide levels can be controlled in a financially viable and potentially appealing manner. Carbon monoxide is a valuable feedstock for the chemical industry and as a base for synthesising renewable fuels. It is currently produced using high temperatures and pressures. Utilising the non-equilibrium nature of low temperature plasmas to convert CO_2 is of growing interest.

Radio-frequency atmospheric pressure plasmas are well known for their ability to produce chemical species at low gas temperatures with high scalability for industrial processes and low operating powers. However, they have not been extensively studied for their application in converting carbon dioxide. The aim of this work was to study the effectiveness of radio-frequency atmospheric pressure plasmas for converting carbon dioxide into value added chemicals and the underlying mechanisms that cause dissociation in order to better understand how to improve the process.

In order to determine the level of conversion of carbon monoxide the Fourier transform infra-red spectroscopy diagnostic was used and the power deposited in the plasma was measured to calculate the energy efficiency of the dissociation. A global model was also developed to provide a greater understanding of the reaction pathways that lead to the conversion of carbon dioxide. The predictions made by the model were then tested using two-photon absorption laser induced fluorescence by measuring both the densities of atomic oxygen and carbon monoxide and comparing them to the model predictions. Finally the ability to utilise the plasma produced carbon monoxide was studied in order to determine how viable these plasmas would be for commercial use. High yields of over 98% were obtained at the expense of energy efficiency; a maximum energy efficiency of 9% was also obtained.

Contents

List of Figures

List of Tables

Declaration

The work presented in this thesis is original and has not been submitted for any other degree at this or another institution. All sources are acknowledged and referenced. The results contained in this thesis are of my own work unless otherwise stated.

Chapter 8 contains work performed in collaboration with James Comerford of the Green Chemistry Center of Excellence at the University of York and some of the contents of Chapters 5 and 6 are intended to be published at a later date and has been presented at conferences.

Chapter 1

Introduction

Current means for the production of global energy needs are largely from non-renewable fossil fuels which contribute substantially to the increase in greenhouse gases in the atmosphere. Carbon dioxide, CO_2, is one such greenhouse gas and is a contributing factor to climate change. The reduction of greenhouse gases and the increased use of renewable or green sources of energy are defining challenges for the 21^{st} century.

The two major challenges in reducing the effects of climate change are reducing the reliance on fossils fuels and reducing the level of greenhouse gases in the atmosphere. There are two methods of reducing CO_2 levels in the atmosphere, the first is carbon capture and storage (CCS) [1]. CCS is fairly well understood but faces many economic challenges in its implementation [2]. CCS is a expensive activity that is unprofitable and so there is little incentive for commercial operators or governments to implement any kind of carbon capture technology. The second option is carbon capture and utilisation (CCU) [3, 4]. CCU is the more attractive option due to the ability to sell its products and potentially the methods used can be profitable and commercially viable.

The utilisation of CO_2 through the conversion of CO_2 into carbon monoxide, CO, has the potential to provide alternative fuels [5, 6] that will be fundamentally renewable as the CO_2 produced using these fuels, and assuming the continuing emissions of CO_2 from other industrial facilities, can be captured and used to create new fuels. The new fuels could provide a cheaper alternative to the energy produced from fossil fuels [7]. Higher hydrocarbon chains can be produced through the creation of synthesis gas or syngas [7–9]. As well as uses for the formation of alternative fuels CO has many uses in the chemical industry as a feedstock [3, 10].

It plays an important role in the manufacture of a variety of chemicals such as acids, esters and alcohols as well as reacting with some metals to form carbonyls [11, 12]. CO_2 will eventually be produced through these processes again and so these methods are reducing the amount of CO_2 in the atmosphere by recycling what is already there as opposed to removing CO_2 from the atmosphere permanently.

However, CO_2 is a very stable molecule and the thermal energy required to dissociate it is large even with the use of a catalyst. Currently the main process used for the conversion of CO_2 into CO is dry reforming of methane which requires temperatures of thousands of Kelvin even with the presence of a catalyst [13]. Alternative electrical means are being studied as a means of generating solar fuels, including electrolysis [10] and plasma based conversion. Many of these methods are still in the early phases and a full cost analysis of these methods, that includes the energy required to recapture the CO_2 that is not converted has needs to be considered. The energy required to capture unconverted CO_2 is high [14] and so economically viable methods of converting CO_2 are likely to need high conversions and selectivity.

In order to overcome the endothermic dissociation reaction of CO_2 the use of many different low temperature plasmas have been studied [15–18]. In a low temperature plasma the neutral gas temperature is kept close to ambient temperatures whilst the electrons are heated to temperatures close to that of the bond energy of CO_2. These energetic electrons are then able to induce the dissociation and convert CO_2 without the need for heating the gas to high temperatures. The range of plasmas studied includes atmospheric [19] and low pressure [20] discharges as well as a range of different driving frequencies from kHz [21] to GHz [22]. The conversions and energy efficiencies obtained by these plasmas demonstrate that there is a trade off between high conversions and high energy efficiencies.

This work will look at the fundamental dissociation processes of the conversion of CO_2 in an atmospheric radio frequency plasma. A radio-frequency plasma was chosen because of the spatial homogeneity and continuous discharge of the plasma making them ideal for global chemical kinetic simulations. Atmospheric pressure plasmas were used in order to minimise the energy required to generate the plasmas and to maximise the throughput of the feed gas to make them more viable for industrial and commercial applications.

Chapter 2

Fundamentals of Low Temperature Plasma Physics

2.1 Plasmas Definition

A plasma is considered to be the fourth state of matter and occurs when electrons become free from atoms and move freely within a gas. This gas then consists of positive ions and negative electrons in nearly equal measure. However being a ionised gas is not enough to be defined as a plasma. A plasma is defined as a quasi-neutral gas consisting of charged and neutral particles which exhibits collective behaviour [23]. Quasi-neutrality is defined simply as the density of negative species, electrons and negative ions, (n_-) being approximately equal to the density of positive species (n_+) in the bulk. Quasi-neutrality does not hold on the microscopic scale.

2.1.1 Debye Length

A plasma is able to screen out electric potentials that are applied to it. If a positively charged ball is lowered into a plasma, the electrons will be attracted to the ball and screen out the positive charge from the rest of the plasma. Similarly if a negatively charged ball is lowered into the plasma the positive species will screen the ball from the rest of the plasma. There is a characteristic length of this shielding called the Debye length, λ_D, and for lengths smaller than the Debye

length quasi-neutrality does not hold. This characteristic length can be derived from Poisson's equation, 2.1, and is given in equation 2.2.

$$\frac{d^2\phi(x)}{dx^2} = \frac{e}{\epsilon_0}(n_i - n_e) \tag{2.1}$$

$$\lambda_D = \left(\frac{\epsilon_0 k_b T_e}{n_e e^2}\right)^{1/2} \tag{2.2}$$

Due to the electrons having considerably less mass than the ions, the electrons are far more mobile. Therefore the ions can be considered as static when determining the Debye length and only the electron temperature, T_e, and the electron density, n_e, are considered. The Debye length also depends on the fundamental charge constant, e, the permittivity of free space, ϵ_0, and the Boltzmann constant, k_b.

To fulfil the second condition of being a plasma collective behaviour must be exhibited. For this to happen the electrons in the plasma must be close enough so that each particle can influence many others and the number of particles within the Debye sphere must be sufficiently large. This criteria is given in equation 2.3 and is fulfilled when $N_D \gg 1$.

$$N_D = n_e \frac{4}{3}\pi\lambda_D^3 \tag{2.3}$$

2.1.2 Plasma Frequency

There is also usually a third condition to define a plasma as a plasma, rather than an ionised gas, which is connected to the collisions in the plasma. For electrostatic interactions to dominate over kinetic effects the plasma frequency, ω_p, must be larger than the collisions frequency in the plasma, ν_c, as shown in equation 2.4. The ions in the plasma are much more massive than the electrons and are therefore slow moving in comparison. The ion plasma frequency, ω_{pi}, is much smaller than the electron plasma frequency, ω_{pe}, and the plasma frequency can be approximated to be just that of the electrons.

$$\nu_c < \omega_p = \sqrt{\omega_{pe}^2 + \omega_{pi}^2} \tag{2.4}$$

The electron plasma frequency can be derived by considering the effect dislocating the electrons, in a plasma of uniform charge density, by a small distance δ in one direction assuming that the ions remain stationary. This leads to a build up of charge, one positive and one negative, between the ions and the electrons. This induces an electric field which will accelerate the dislodged electrons back towards the ions but due to the momentum which the electrons have they overshoot the ions. A region of negative charge now forms on the opposite side of the ions and the electrons will continue to oscillate as there are no damping forces acting on them. The characteristic frequency of this oscillation is the characteristic electron plasma frequency given in equation 2.5.

$$\omega_{pe} = \sqrt{\frac{n_e e^2}{m_e \epsilon_0}} \tag{2.5}$$

The ion plasma frequency takes the same form as the electron plasma density but with the ion density and mass. Since the plasma is quasi-neutral the electron and ion densities are approximately the same and therefore the higher mass of the ions leads to a smaller ion plasma frequency.

2.1.3 Plasma Sheath

To maintain quasi-neutrality in a plasma the fluxes of the positive and negative species leaving the plasma must be the same. Due to the smaller mass of the electrons compared to the ions they have a larger thermal velocity. Electrons are able to reach the walls confining the plasma faster than ions. This leads to a breakdown of quasi-neutrality near the walls of the plasma. There is a region of net positive charge at the edge of the plasma. This net positive region is known as the plasma sheath. The plasma sheath pushes electrons back into the plasma bulk, due to the build up of negative charge on the walls, and accelerates ions towards the surface in order to satisfy there being zero net charge flux at the wall.

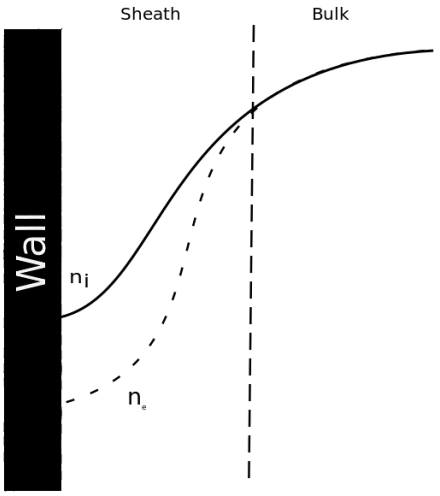

FIGURE 2.1: A depiction of the plasma sheath charge. In the bulk plasma the positive ion density is roughly equal to the negative ion and electron density and quasineutrality is held. Quasineutrality breaks down in the sheath region due to the electron being lighter and more mobile than the positive ions. This causes a net positive charge in the plasma sheath region and a negatively charged wall.

2.2 Electron Energy Distribution Functions

Low temperature plasmas characteristicly have low degrees of ionisation where the electrons are accelerated through externally applied electric fields up to temperatures in the region of tens of thousands of Kelvin. However the ions and the neutral gas temperature remains small, in the region of hundreds of Kelvin. The plasma is therefore far from thermal equilibrium and the ionisation and excitation processes that are important to sustaining the plasma are driven by the energetic electrons described by the Boltzmann equation given in equation 2.6. Where f is the electron energy distribution function (EEDF) in six dimensional phase space, $\boldsymbol{v}_e$ is the electron velocity distribution, $\boldsymbol{E}$ is the electric field, $\boldsymbol{\nabla}_v$ is the velocity-gradient operator and the right hand side of the equation is the rate of change of the EEDF due to collisions in the plasma.

$$\frac{\partial f}{\partial t} + \boldsymbol{v_e} \cdot \boldsymbol{\nabla} f - \frac{e}{m_e} \boldsymbol{E} \cdot \boldsymbol{\nabla}_{\boldsymbol{v}} f = \left(\frac{\partial f}{\partial t}\right)_c \tag{2.6}$$

If the electrons in the plasma are in thermal equilibrium with each other and the degree of ionisation is high, the EEDF is Maxwellian. However this is not the case in the types of plasmas studied in this work. The degree of ionisation is very low in these plasmas, 10^{-8}, and the plasmas studied are not dominated by electron

electron collisions. Low temperature plasmas are dominated by inelastic collisions of electrons with heavy particles. This causes a depletion of the high energy tail of the distribution and a deviation from a Maxwellian distribution. This depletion of the high energy tail of the distribution leads to a Druyvesteyn distribution of electron energies. This distribution is often a more accurate distribution of electron energies for plasmas with low degrees of ionisation. However, in a Druyvesteyn distribution it is assumed that elastic collisions dominate and the effect of inelastic collisions is insignificant. In an elastic collision with atoms, the direction of motion of electrons is changed but due to the large difference in mass between electrons and atoms the energy of the electrons remains unchanged. In inelastic collisions the energy of the electrons is changed and these collisions often lead to excitation or ionisation of the atoms or molecules in the plasma.

In a plasma that includes molecules as well as atoms there are many degrees of freedom for excitation of the molecules, including bending, stretching and vibrational modes and electronic excitation. Therefore in the plasmas studied the effect of the inelastic electron collisions in the plasma cannot be assumed to be insignificant and in order to accurately determine the EEDF, which is vital for computing reaction rates used in modelling the plasma, the Boltzmann equation, 2.6, can be solved.

2.2.1 Solving the Boltzmann Equation

The EEDF can be calculated for the discharge conditions from the collision cross-section data for the plasma species by solving the Boltzmann equation. This is commonly done for several values of reduced electric field, E/N, which is the ratio of the electric field strength to the number density of particles in the gas. Then the mean electron energy for the value of the reduced electric field can be compared to the mean electron energy in the model and the corresponding EEDF can be used to calculate the reaction rates for the collisional processes in the plasma.

In order to be able to solve the Boltzmann equation, equation 2.6 must be simplified as described in [24]. The first simplification is that the electric field and collision probabilities are spatially uniform on the scale of the mean free path. The electron distribution is then symmetric in velocity space and only varies along the direction of the electric field, obtaining equation 2.7.

$$\frac{\partial f}{\partial t} + v cos\theta \frac{\partial f}{\partial z} - \frac{e}{m_e} E\Big(cos\theta \frac{\partial f}{\partial v} + \frac{sin^2\theta}{v} \frac{\partial f}{\partial cos\theta}\Big) = \Big(\frac{\partial f}{\partial t}\Big)_c \tag{2.7}$$

A common approach to solve equation 2.7 is to expand the electron distribution, f, in terms of Legendre polynomials of cos θ. A two term approximation is often enough to give valuable results for the EEDF and is used in most Boltzmann equation solvers including the ones used in this work. This approximation fails at high values of E/N when elastic collisions start to dominate but is valid for the range used here. In this approximation the distribution function, f, depends on velocity, v, θ, the angle between the electron velocity, v, and the electric field, time, t, and the position along the electric field direction, z. The θ dependence is simplified using the two term approximation, and the time dependence is simplified by assuming a steady state where the electric field and electron distribution are stationary. Through these simplifications and considering the effect of the collisional processes that occur in plasmas the EEDF can be calculated and used to find the appropriate reaction rates for the electron impact reactions in the plasma. More detail on the two term approximation and calculating the EEDF is given in [24].

2.3 Radio Frequency Plasmas

To successfully ignite a plasma a voltage is applied across an electrode gap filled with a gas. Ignition is achieved if the mean free path of the electrons, λ_e, is large enough so that the electrons can gain sufficient energy from the electric field to ionise the gas. If more electrons cause ionisation events than are lost an electron avalanche occurs, travelling towards the anode, and the plasma can become self-sustaining. The plasma becomes self-sustaining because of the difference in mass between the electrons and ions. Radio frequency plasmas operate in the high frequency region of the RF spectrum. These frequencies are too fast for the ions to respond to but not too fast for the electrons. This means that almost all of the electrical energy can be coupled into the electrons, causing them to have a much higher temperature than the ions. The AC field also acts to better confine the electrons in a plasma so that the plasma can be more readily self-sustaining. In a simplified picture the AC field causes the electron bulk to oscillate between the two electrodes. The AC field is driven, typically, at 13.56 MHz which has been

designated by the International Telecommunications Union as a frequency for use for industrial, commercial or scientific purposes. The second and third harmonic, 27.12 and 40.68 MHz respectively, are also free to use for industrial and scientific purposes [25].

The almost exclusive coupling of energy to the electrons over the ions causes a significant difference in the temperature of the species. The electron temperature, T_e, is much higher than the ion temperature, T_i, and the gas temperature, T_g. The electron temperature is usually on the order of 30 000 K, whilst the ions and neutral gas are on the order of 300 K. Therefore there is a large difference in temperature between the plasma species and they are clearly not in thermodynamic equilibrium, and consequently these types are plasmas are referred to as 'non-thermal plasmas'. The electron temperature is usually expressed in terms of electronvolts, eV, where 1 eV is approximately 11 600 K.

The electron temperature refers to the mean electron energy of the plasma and exists in a distribution as described in the above section. Most of the electrons in these plasmas do not have enough energy to cause ionisation of plasma species but can produce radical species, excited species or even cause dissociation of molecular species [26–29]. The plasma chemistry that occurs within plasmas is therefore electron driven and will depend on the electron density and the EEDF. This enables non-thermal plasmas to perform chemical reactions in conditions where the reaction would usually be energetically unfavourable.

2.3.1 Operating Regimes

There are two distinct operating modes that can be observed in radio frequency plasmas. The two modes can be distinguished visually by their differences in the emission of light. They also have different governing ionisation processes that produce the electrons sustaining the plasma. The first operating regime is α mode. In this regime the ionisation in the plasma is predominantly in the plasma bulk. This regime is referred to as alpha mode because the electron production is governed by the first Townsend coefficient, α. This coefficient describes how the electron avalanches, that produce the electrons required to sustain the plasma, evolve. The second operating regime in radio frequency plasmas is called γ mode. In γ mode secondary electron emission from the sheath region starts to become a dominant source of electrons. The probability of the production of secondary

electrons is given by the second Townsend coefficient γ. In γ mode the electron density increases, as there is a new source of electrons.

2.3.2 Atmospheric Pressure Radio Frequency Plasmas

This work will focus mainly on radio frequency plasmas that can operate at atmospheric pressure. The main benefits of using atmospheric pressure plasma come from not needing to use expensive vacuum technology and being able to produce chemical radicals. Atmospheric pressure plasmas are highly collisional and as such the electron temperatures and densities tend to be lower than in low pressure plasmas. This is due to collisions reducing the mean free path of the electrons and causing them to gain less energy from acceleration through the electric field. Since the electrons have in general a lower energy they are also less likely to have enough energy to ionise the background gas and therefore the electron density tends to be lower. However, the highly collisional nature of the plasma means that the electrons are more likely to collide and excite the background gas. This can lead to more chemical radicals and the production of reactive species that make atmospheric pressure plasmas desirable.

2.3.2.1 Paschen Criterion

A certain voltage is required across the electrodes in order to cause breakdown in a gas. This breakdown voltage is often expressed as a function of the pressure length product, pd, according to the Paschen criterion, see Figure 2.2. In order to design a vessel where a plasma can be successfully ignited both the pressure and the inter electrode distance must be considered. To enable a plasma to be ignited at atmospheric pressure the gap between the electrodes must be very small, usually 1 mm. If the plasma is to be used at low pressure, larger electrode gaps can be used, usually to the order of a few centimetres. However, the length scale used must be significantly larger than the Debye length if the discharge is to produce a plasma and maintain quasi-neutrality.

The deduced sheath width for a typical radio frequency atmospheric pressure plasma is approximately 200 μm and so it is important that the electrode gap is kept larger than this distance despite the reduction in breakdown voltage that

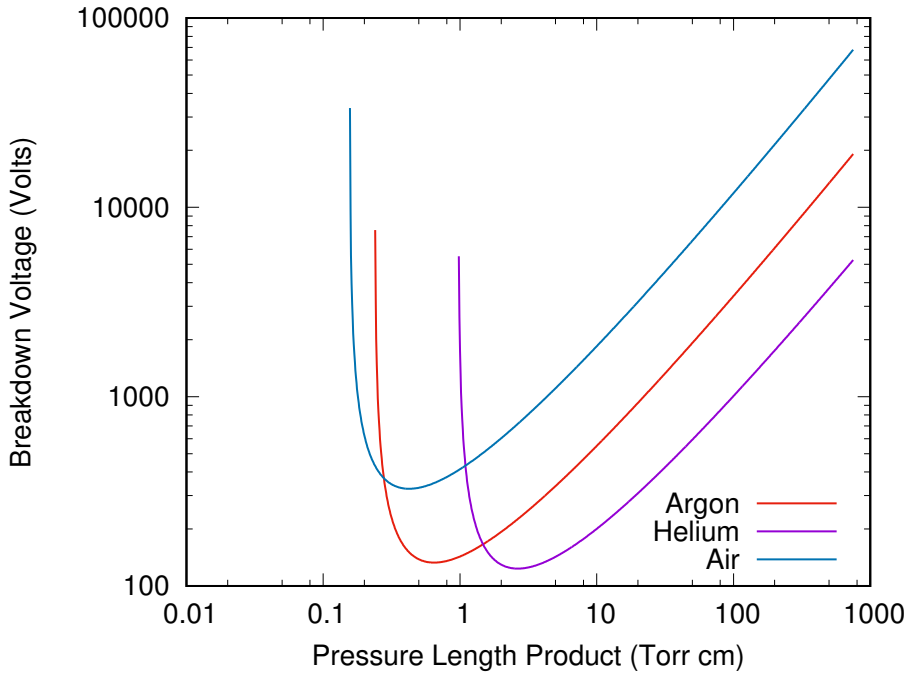

FIGURE 2.2: The breakdown voltage of different gases as a function of the pressure length product. For this study the pressure length product is 38 Torr cm and so the plasma will be most easily ignited in helium and then argon. Values taken from [30, 31]

could be achieved at atmospheric pressure using such small distances. If an electrode gap smaller than the sheath width was used the plasma would not have a bulk region and would exist as just a single sheath region [32]. Due to the highly collisional nature of atmospheric pressure plasmas the kinetic effects of the gas also dominate over the electrostatic interactions that dominate in collisionless plasmas. At standard temperature and pressure the electron collisions frequency with the background gas is found to be orders of magnitude larger than the electron plasma frequency. Instead of oscillating at the plasma frequency the electron path is more accurately defined by a drift velocity, v_d, given in equation 2.8, where ν_m is the collision frequency. The drift distance trough one RF cycle is still less than the electrode spacing. The ions undergo collisions that will stop them oscillating at the plasma frequency, but as their mass is larger than that of the electrons and they do not 'see' the oscillating electric field, they follow the kinetics of the background gas.

$$v_d = \frac{eE}{m_e \nu_m} \tag{2.8}$$

Chapter 3

Non-thermal Plasmas for CO_2 Conversion

3.1 Thermal Dissociation of CO_2

The dissociation of CO_2 is an endothermic reaction, meaning that the reaction requires heat in order to occur. Figure 3.1 was calculated using the NASA CEA code [33, 34] at atmospheric pressure. It is clear that CO_2 will not begin to dissociate until the temperature reaches 2000 K and significant dissociation of CO_2 is not achieved until temperatures are over 3000 K. Between 3000 and 3500 K the molar fractions of CO and O_2 are maximised. The maximum energy efficiency that can be achieved in the thermal plasma dissociation of CO_2 is 43% [35].

Using high temperatures to convert CO_2 also leads to a significant molar fraction of atomic oxygen in the gas. Atomic oxygen is a highly reactive species that would ideally be used to react with CO_2 to produce more CO and molecular oxygen O_2, however at high temperatures the reverse reaction of atomic oxygen recombining with CO is favourable and depending on how the gas is cooled after thermal decomposition a significant portion of the CO yield can be lost due to the reverse reaction. Therefore the use of plasmas to convert CO_2 into CO appears ideal as the non thermal nature of certain plasmas means that the neutral CO_2 can be kept cold and the thermal electrons can be used to convert the CO_2. Keeping the CO_2 cold should reduce the amount of recombination seen from the reactive atomic oxygen species and potentially be more energetically efficient.

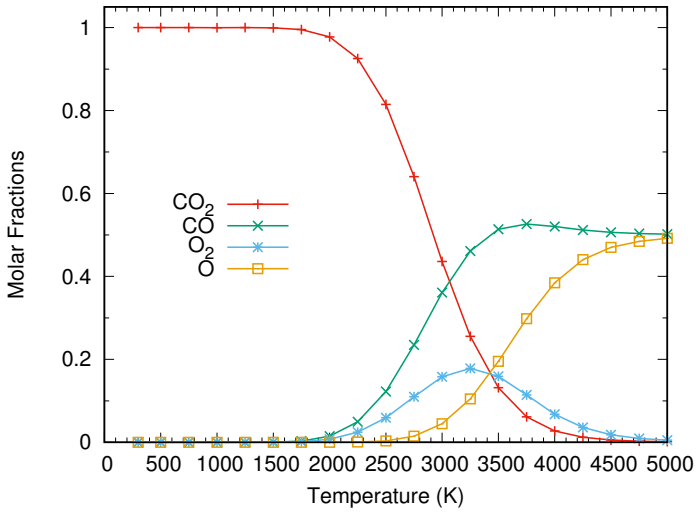

FIGURE 3.1: The molar fractions of CO_2 and its' dissociative products as a function of temperature calculated using the NASA CEA code [33, 34]. Significant dissociation of CO_2 begins for temperature above 2000 K but dissociation of all CO_2 requires temperatures of 5000 K. For higher temperatures complete CO_2 dissociation will occur and carbon will be produced.

3.2 Plasma Dissociation of CO_2

The prospect of an industrial plasma for converting CO_2 into value added chemicals would have many advantages over current industrial methods. In general due to the high power densities of plasmas the reactors, particularly at atmospheric pressure, are compact and have low costs. Plasma chemistry also happens on a fast time scale, with residences times typically on the order of milliseconds. A wide variety of plasmas have been studied for the conversion of CO_2, ranging from both atmospheric [22] to low pressure [36] and driving frequencies from kHz-GHz [17, 18, 37].

A comprehensive review of the current plasma CO_2 conversion technology has been performed by Lebouvier [38]. Lebouvier shows that the current challenge in making plasma based CO_2 conversion viable is how to sufficiently overcome the trade off seen between the yield of CO and the energy efficiency of the conversion. For plasmas which are able to achieve high conversions, of nearly 90%, the corresponding energy efficiency is only a fraction of a percent [39]. For plasmas with high energy efficiency, of nearly 60%, the corresponding conversion is less than 10% [40].

3.2.1 Dielectric Barrier Discharges

One common method of plasma based CO_2 conversion is the use of a dielectric barrier discharge (DBD) [41–49]. In a DBD at least one of the two electrodes is covered by a dielectric and can occur in many different reactor designs, most being either planar or cylindrical. The discharges in a DBD are filamentary, which means that the plasma breakdown occurs at different positions in the reactor at the same time in small lighting like streams. The plasma is therefore far from spatially homogeneous. DBDs have a driving frequency in the region of kHz which is not high enough to sustain a constant plasma discharge and the driving voltages are in the order of kV. A DBD will appear to be a constant plasma to the naked eye but with a high speed camera it is possible to see the plasma turning on and off with the electric field.

Due to the high driving voltages used in DBDs they are able to operate in pure CO_2 even at atmospheric pressure [50] but they have also been studied with the addition of noble gases, namely helium and argon [51]. DBDs have higher conversions than energy efficiencies. Conversions in DBDs tend to be able to reach conversions of up to 30% [50] for high input powers in pure CO_2 with the conversion increasing up to 40% [51] with the addition of argon. However, for the highest conversions the corresponding energy efficiency is only 3%. The effect of the addition of a nobel gas is to increase the total conversion of CO_2 at the expense of energy efficiency, as there is a specific energy input per CO_2 molecule. The energy efficiencies achieved in DBDs are not as high, reaching a maximum of around 10% for the low input power cases [52] with conversion of only 6%. Some studies have found that the less filamentary discharges produce greater conversions of CO_2 [53].

3.2.2 Microwave Plasmas

Microwave plasmas have a driving frequency in the region of GHz and have proved promising in terms of high energy efficiency but as such have lower conversions of CO_2 [54]. Microwave plasmas can also operate in pure CO_2 both at low pressure [36] and in an argon CO_2 mixture at atmospheric [22]. For an atmospheric pressure microwave discharge [22] the maximum energy efficiency achieved was 20%, double what was achieved at atmospheric pressure in a DBD. The corresponding

conversion however was only 10%, although this is still higher than the conversion achieved for the most energetically efficient DBD. The highest conversion achieved in an atmospheric pressure microwave discharge was nearly 50%, which again is an improvement over the highest conversion achieved using a DBD. The corresponding energy efficiency was only at 5% which is a very similar value to that of the highest conversion DBD case. The input power in the microwave case is also on the order of kW. However microwave discharges have a tendency to heat the neutral gas to very high temperatures [36, 55] with the rotational gas temperatures in the above cases reaching 6000 K, where Figure 3.1 shows CO_2 will thermally decompose.

For moderately low pressures energy efficiencies of nearly 50% are achieved [36, 56], which again is a vast improvement over the maximum atmospheric pressure microwave plasma and the corresponding conversion for these efficiencies are approaching 15%, which is also the maximum conversion achieved. The pressures used to achieve these results are of the order of hundreds of millibar, typically between 100-200 mbar. As with the atmospheric pressure microwave plasma the gas temperature in the moderately low pressure microwave plasmas is in the order of 2500-3500 K where CO_2 will thermally decompose. This brings into question how effective the plasma is in the dissociation as the maximum efficiency achieved in these plasma is very similar to the maximum thermal efficiency. The gas temperature is also shown to decrease with reduced pressure but remains in the order of thousands of Kelvin.

Low pressure microwave plasmas have also been studied at very low pressure [57], 7 Torr, using input powers of only 400 W. The conversion and energy efficiency were found to be much lower than in the moderate pressure cases. The highest energy efficiency was over 15% and the corresponding conversion was also the maximum found at over 10%. The highest energy efficiencies achieved in these types of plasmas were achieved in the 1980s and the energy efficiency achieved was upwards of 90% [58], supported theoretically [59], however these values have not been repeated. Even with high gas temperatures energy efficiencies this high suggest more than just thermal decomposition and the understood mechanism for more efficient CO_2 dissociation is through the vibrational excitation of a C-O bond in the CO_2 molecule.

3.2.3 Vibrational Excitation of CO_2

There are three main forms of vibrational excitation in a CO_2 molecule. These are symmetric stretching, asymmetric stretching and bending modes. In symmetric stretching of CO_2 the two oxygen atoms in the molecule vibrate in a way that means no dipole moment is ever formed in the molecule. That is to say that the two oxygen atoms remain the same distance from the carbon atom throughout the vibration. The symmetric stretch of CO_2 is the most short lived and often decay through vibrational-translational relaxation and as such they generally do not lead to the dissociation of the CO_2 molecule and act only as a loss channel for the electron energy. The dissociation of CO_2 via vibrational excitation has been found to overcome electron impact dissociation for low values of reduced electric field, E/N [60].

In the asymmetric stretch of CO_2 however, the two oxygen atoms do not always remain the same distance away from the carbon atom and as such generate a dipole moment on the molecule. The asymmetric stretch does not relax through vibrational-translation relaxation as quickly as the symmetric stretch of CO_2 and as such vibrational energy up-pumping can occur. In the up-pumping process vibrational energy is transferred between two CO_2 molecules to the effect of increasing the vibrational energy of one CO_2 molecule until it reaches the dissociation limit of 5.5 eV and the molecule can dissociate. This method of populating high energy asymmetric states of CO_2 that then lead to dissociation is the most efficient path for the dissociation of CO_2 and the theoretical basis for this has been studied in some detail [61]. This method of dissociation is thought to become competitive with direct electron impact dissociation for plasmas with high values of vibrational temperature [62].

Fridman [61] sets out three reasons why the asymmetric stretch of CO_2 is the most energetically efficient method for dissociation. Firstly, for the electron temperatures typically seen in non-thermal plasmas, 1-2 eV, a majority of the electron energy can be transferred into the asymmetric stretch over the other excitations in the plasma. Secondly, the vibrational energy of the CO_2 molecule is able to lower the activation energy that must be overcome for the endothermic CO_2 dissociation reaction to occur, as shown in equation 3.1. Thirdly, vibrational excitation requires only the dissociation energy of 5.5 eV whilst direct electron

impact dissociation of CO_2 requires over 7 eV due to the Frank-Condon principle. Direct electron impact dissociation requires excitation into an electronic state whose energy is more than that of the dissociation energy for it to relax into a dissociative state.

$$k = A_0 exp\Big(- \frac{E_a - \alpha E_v}{T_g} \Big) \tag{3.1}$$

Where k is the rate constant for the reaction, A_0 is the Arrenhius coefficient, E_a and E_v are the activation energy of the reaction and the vibrational energy of the reactant respectively, T_g is the gas temperature in Kelvin and α is a parameter to determine the efficiency of lowering the required energy according to the Fridman-Macheret α-model [61]. The lowering of a reactions activation energy due to the vibrational energy of the CO_2 molecule allows for the atomic oxygen produced in the dissociation of CO_2 to be recycled to create more CO and O_2 as the CO_2 reaction with atomic oxygen is faster than the three body recombination of atomic oxygen [61].

The energies of the CO_2 vibrational levels have been calculated using an anharmonic oscillator [63] up to the dissociation energy of CO_2 [64]. However cross sectional data and reaction rates for the highly excited CO_2 molecules are not known and must be approximated. The Fridman approximation [61] provides a means to approximate the cross sections for electron impact reactions for CO_2 stretches according to the low energy states that can be measured. There are also scaling laws used to scale the vibrational energy transfer reactions according to the energy of the state [64, 65]. The bending modes of CO_2 are also not important in the dissociation process of CO_2 as they are quenched by vibrational-translational reactions quickly as with the symmetric stretches. The quenching of these states is too quick to lead to dissociation. The dissociation of CO_2 via vibrational states has been extensively modelled [49, 64–66]

3.2.4 Enhancing Vibrational Excitation of CO_2 using N_2

CO_2 lasers work by populating the asymmetric stretches of CO_2 by the transfer of vibrational energy through collisions with vibrationally excited N_2 molecules [67]. Helium also has a role to play in CO_2 laser excitation, but rather than enhancing the CO_2 asymmetric vibrational excitation, it increases the electron temperature

which in turn favours the vibrational excitation of N_2 and CO_2. Many studies have been performed on the effect N_2 has on populating the asymmetric stretches of CO_2 in a plasma [18, 20, 68]. These studies have found that the production of high energy asymmetric states is important for the dissociation of CO_2 and is more important than direct electron impact dissociation and dissociative recombination, which is dominant in an N_2 discharge [69].

A study of the chemical kinetics of CO_2 and N_2 discharges [18] reports that increasing the N_2 admixture in the plasma increases the conversion of CO_2. However since increasing the fraction of N_2 decreases the CO_2 fraction the effective conversion reduces. Therefore the energy efficiency decreases in general with increasing N_2 admixture in the discharge as the specific energy input per CO_2 molecule increases with constant power input. It is also reported that the main destruction pathway of N_2 is through a reaction with atomic oxygen, which is not desired as the recycling of atomic oxygen to produce more CO and O_2 from CO_2 is desired for efficient dissociation. It is concluded that while vibrationally excited N_2 is effective at populating CO_2 asymmetric vibrational levels, the extent to which this happens does not have a significant effect on the energy efficiency of CO_2 dissociation. This addition of N_2 also inevitably increases the formation of by-products through reactions with oxygen and nitrogen.

3.3 The Radio-frequency Atmospheric Set-up

Previous radio frequency plasmas have focussed on low pressure discharges [37, 70–73]. Some been found to be very effective at converting CO_2 with conversions reaching 90%. However there is always a trade of with the energy efficiency and the corresponding energy efficiency was less than 0.5% [37] using a driving frequency of 13.56 MHz and operating powers of up to 1 kW. The maximum energy efficiency achieved in the radio frequency discharge was 3% with a corresponding conversion of nearly 20%. The high conversions fore a single pass of CO_2 through the reactor mean that radio-frequency plasmas could be viable if the energy cost of capturing CO_2 can be reduced [14] or the energy efficiency of the plasma improved. The high conversion means that as a source of CO for industrial chemical processes, where throughput matters more than efficiency, the radio frequency plasma may be a viable and desirable option. Previous radio frequency plasmas were performed at low pressure, 80-280 mTorr, and as such would not produce particularly high

throughput of CO but by operating at atmospheric pressure it is possible to greatly increase this and potentially enable high-volume in-line production [74, 75].

To enable the plasma to operate with a carrier gas of both helium and argon an electrode gap of 0.5 mm has been used in the set-up. As mentioned in the previous chapter the breakdown voltage required to ignite the plasma depends on the pressure and the length. By reducing the electrode gap from the usual 1 mm [76–78] size to 0.5 mm the breakdown voltage becomes low enough for ignition to occur in argon gas as well as helium. The electrodes themselves have dimensions of 50 mm x 5 mm are made of copper as shown in 3.2. A borosilicate glass tube is used to both prevent arcing between the electrodes and to enclose the plasma from ambient area, to reduce impurities in the plasma and prevent CO flowing into the ambient air. A driving frequency of 40.68 MHz, from an Advanced Energy Caesar 403 generator, is used as using higher harmonics of the standard 13.56 MHz was found to be more efficient at converting CO_2 due to the effective confinement of electrons. Small admixtures of CO_2, up to 2.5%, are added to the carrier gas as the voltage across the electrode is not high enough to cause breakdown in pure CO_2. Fourier Transform Infra-red (FTIR) Spectroscopy, Thermo Fisher Nicolet iS50, is utilised as the main diagnostic for analysing both the conversion of CO_2 and the production of CO.

Mass flow controllers, MKS MF-1, are used to control both the overall gas flow and the admixture of CO_2 in the flow. A voltage and current probe, SOLAYL SAS Vigilant Sensor VSN-500X-50-1M-1F-100, are used to measure the voltage and current in the plasma to enable the plasma power to be measured. Radio-frequency atmospheric pressure plasmas remain relatively cool during operation compared to microwave plasmas for instance, with the gas temperatures remaining below 350 K. The power used to generate and sustain the plasma is also less than 100 W which is also smaller than with other plasmas used for CO_2 conversion which typically use hundreds of watts. However the specific energy input per molecule of CO_2 in the radio-frequency plasmas is usually higher than other methods.

3.4 Fourier Transform Infra-red Spectroscopy

Both CO_2 and CO are highly stable molecules and can be measured in the far effluent using Fourier transform infra-red (FTIR) spectroscopy. This means that

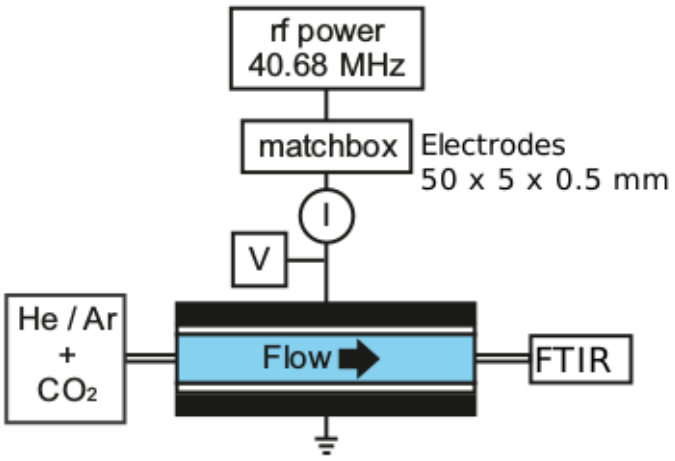

FIGURE 3.2: A schematic of the experimental set-up. The plasma reactor design is a slightly modified version of the standard atmospheric pressure plasma[79]. The electrodes are 50 by 5 mm in area and there is a 0.5 mm gap between the pieces of borosilicate that is between the electrodes, this gap size enables the effective use of argon as a carrier gas. The driving frequency of 40.68 MHz enables higher electron powers and densities in the plasma which should favour conversion of CO_2. A voltage and current probe is also placed between the matchbox and the plasma in order to calculate plasma power and the gas lines lead to an FTIR for analysing the gas.

the plasma itself will not be disturbed by any diagnostic used to measure the plasma species. Measuring in the far effluent also means that any CO that would recombine into CO_2 after it leaves the plasma and would not be measured in the yield values. Therefore if the plasma were to be used as an in-situ source of CO, what is measured in the FTIR would be available for use in a laboratory setting. Stainless steel pipes are used to ensure that the gas that leaves the plasma is not exposed to the air before it reaches the FTIR and to ensure that as few impurities as possible enter the gas cell.

One of the main advantages of using FTIR spectroscopy is that measurements of the concentrations of CO_2 and CO in the sample can be performed at the same time. This is made possible through the use of a broadband infra-red (IR) source that means that a broad range of wavelengths is sampled in a single measurement. The FTIR scans in the mid infra-red region, 4000-400 cm^{-1}. This region covers the absorption range of both the bending and asymmetric stretching modes of CO_2, CO and O_3. O_2 does not appear on IR spectroscopy measurements due to being

a homo-nuclear diatomic molecule. Homo-nuclear diatomic molecules have a zero change in dipole moments when they rotate or vibrate and are therefore infra-red inactive. Due to there being no change in dipole moment during a symmetric vibration of CO_2, the symmetric stretch of CO_2 is infra-red inactive and is not detected using FTIR spectroscopy.

3.4.1 Michelson Interferometer

A Michelson interferometer is the core part of an FTIR that allows the FTIR to scan a large wavelength range in one sample. In a Michelson interferometer the IR beam is split into two and the two beams then travel along different paths. Each of the two paths for the beam lead to a separate mirror, one of which is static, the other is movable. The two beams then reflect back to the beam-splitter and recombine and are sent to a detector. A diagram of a Michelson interferometer is shown in Figure 3.3.

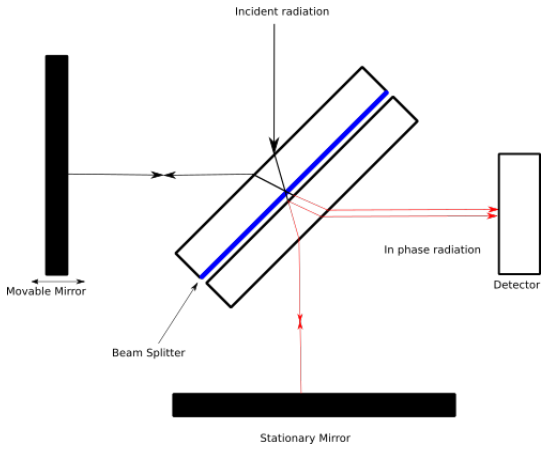

FIGURE 3.3: A diagram of the Michelson interferometer, an integral part of FTIR spectroscopy. A beam splitter splits the infra-red beam, from an IR source, into two that then travel towards two different mirrors. One of the mirrors is movable and this allows for one of the beams to travel a different distance to the other and therefore interfere with the other and produce a cosine wave known as an interferogram.

The movable mirror enables one of the IR beams to travel a different distance than the other. The different distances travelled by the two IR beams means that either constructive or destructive interference, or a mixture of both, will occur when the two beams recombine. Since the mirror moves throughout the sampling the intensity of signal changes and a cosine wave is measured by the FTIR. This cosine wave is known as an interferogram.

The interferogram exists as a function of time and as such it can be Fourier transformed into the frequency domain, which then needs to be deconvolved to obtain the IR spectrum. An example interferogram and IR spectra are shown in figure 3.4. Due to many different molecules been infra-red active, such as H_2O and CO_2, IR spectra can be quite noisy and some care must be taken in analysing the data. The FTIR itself is not completely sealed from external conditions and the spectra can change depending on humidity levels. The FTIR itself is purged with dry air but nevertheless water cannot be completely removed and there is also a background level of CO_2 in the spectra. Water is a problem in the spectra due to it being highly active in the infra-red and much of the CO_2 bands used overlap with water. Therefore, before measurements can be undertaken a background spectra must be undertaken so that the background humidity and CO_2 levels do not affect the measurements. To measure the amount of CO_2 that is converted by the plasma FTIR measurements are taken when the plasma is off as well as on.

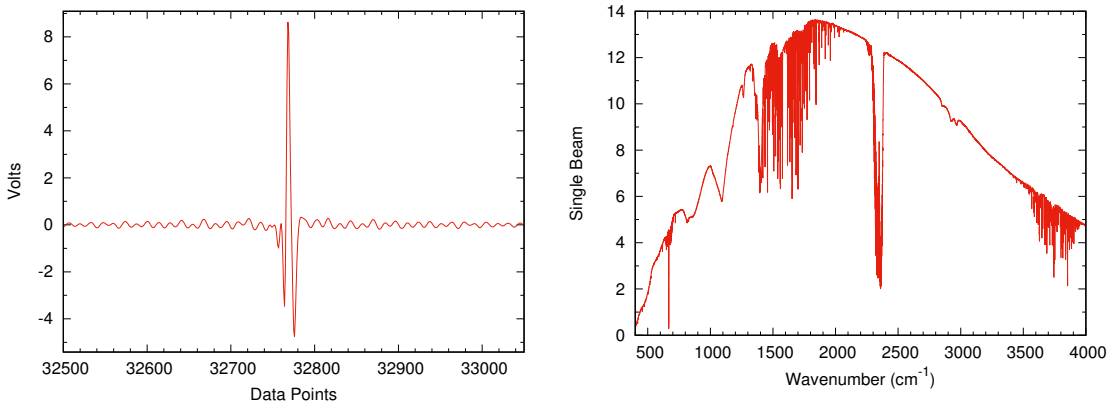

FIGURE 3.4: An interferogram from the FTIR is shown on the left and an example of the background signal in the FTIR is shown on the right. The interferogram is Fourier transformed as shown in the figure on the right. The background scan in the FTIR shows that there is a lot of moisture and background CO_2 in the FTIR that must be considered when taking measurements of the far plasma effluent. The background spectra is subtracted from the sample spectra to leave only the CO_2 and CO coming from the plasma and not the ambient air in the FTIR.

3.4.2 Calibration of the Absorption Areas

The calibration curves for both CO_2 and CO are given in Figure 3.5. Since the volume of the gas cell and the path length in the gas cell is constant the absorption area in the IR spectra is dependent only on the concentration of the species of

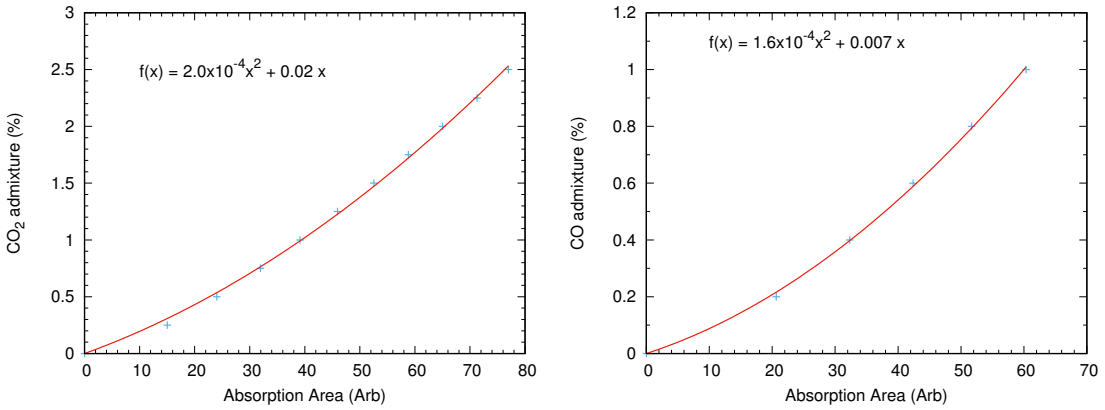

FIGURE 3.5: The calibration of CO_2 absorption area with respect to CO_2 admixture is shown on the left whilst the CO calibration is on the right. The absorption areas of CO_2 and CO were found to be quadratic, with a linear component, with respect to admixture to a reasonable approximation. The calibration curves allow for the admixture of the species to be calculated and therefore the concentration in the gas in the FTIR and from that conversions can be calculated.

interest in the gas cell. The area under the CO_2 and CO absorption spectra can be calibrated to known quantities of the species of interest and is referred to as the absorption area here on in. Then from the calibration curve it is possible to find the concentration of CO_2 and CO in the gas cell from the measured absorption area. The calibration curves were found to be quadratic with a linear component, which is consistent with the first two terms of a Taylor expansion of the Beer-Lambert law given in equation 3.2, where A is the absorbance and I is the intensity of light and I_0 the initial intensity of light.

$$A = -log\left(\frac{I}{I_0}\right) \tag{3.2}$$

3.4.3 Calculating the Yield and Energy Efficiency of Dissociation

The yield of carbon monoxide is readily calculated using equation 3.3, and is defined as the amount of carbon monoxide measured after the gas has passed through the plasma over the amount of carbon dioxide present before the plasma. These can be measured in the FTIR by measuring the absorption area of CO_2 whilst the plasma is not on and measuring the CO absorption area whilst the plasma is on. There should not be any carbon monoxide present in the FTIR

spectra when the plasma is not on and so it is unnecessary to measure it to calculate the yield. The concentration of CO_2 whilst the plasma is running can also be measured and used to calculate the selectivity of carbon monoxide. The selectivity is the amount of converted CO_2 becoming CO and therefore a selectivity of 100% means all converted CO_2 becomes CO. The selectivity has not been the focus of this work due to it being found to be constantly at 100% within error and no carbon deposits observed on the glass tubes.

$$Y = \frac{CO_{out}}{CO_{2in}} \tag{3.3}$$

The energy efficiency, μ, can be readily calculated using equation 3.4, and is simply the ratio of the energy required to dissociate CO_2 and the energy inputted, S_E, multiplied by the yield, Y, of carbon monoxide. The enthalpy of the dissociation reaction of CO_2, ΔH, and the specific energy input per molecule of CO_2 is defined in equation 3.5. In order to be perfectly efficient a specific energy input per molecule of CO_2 is required to be equal to the enthalpy of the dissociation reaction of CO_2, which is 2.9 eV/molecule [61], whilst also converting all CO_2 into CO.

$$\mu = \frac{\Delta H}{S_E} Y \tag{3.4}$$

$$S_E = \frac{P_p/e}{\frac{N_A}{V} Q f} \tag{3.5}$$

In equation 3.5 P_p is the plasma power in W, or J/s, and is divided by the electron charge constant to convert the plasma power into eV/s. N_A is Avogadro's number and is divided by the volume occupied by 1 mole of an ideal gas at standard temperature and pressure. This term therefore gives the number of molecules per litre of 1 mole of an ideal gas at standard temperature and pressure. Q is the flow rate of the gas through the plasma in standard litres per second. Then by multiplying the terms on the bottom by the CO_2 admixture, f, the energy input per molecule of CO_2 is calculated with units of eV per molecule of CO_2.

3.5 Measuring Plasma Power

In an atmospheric pressure plasma the amount of power that is coupled into the plasma can be significantly smaller than the power supplied by the generator. In order to obtain accurate specific energy inputs per molecule of CO_2 required to calculate the energy efficiency of the conversion of CO_2 accurately. In order to mitigate as many as the unknown power losses as possible the voltage and current are measured, using an oscilloscope, after the matching network and just before the plasma itself. However this results in the phase angle between the current and voltage being close to $-\frac{\pi}{2}$ which can lead to very large errors in the power measurement. This is due to the voltage and current being both sinusoidal for an RF power supply and to calculate the power the integral of the product of the voltage, V, and current, I, is taken over one period. Equation 3.6 shows how power is calculated for an AC system.

$$P = \frac{VI}{2} cos(\theta) \tag{3.6}$$

Due to the small period of oscillation in radio frequency plasmas, particularly for 40.68 MHz driving frequencies, modern oscilloscopes do not have a high enough sampling rate to measure the phase difference between the current and voltage accurately enough. In order to obtain a sufficiently accurate measurement of the phase difference one robust and quick method is to take a fast Fourier transform (FFT) [80]. Taking an FFT of the waveforms allows for the amplitude of the voltage and current to be taken at only the driving frequency and measure the phase difference for this frequency only. This is assuming that the harmonics of the driving frequency has an insignificant contribution to the power deposition. The phase difference between the voltage and current can then be measured by calculating the difference between their individual phases.

The method for calculating the power deposited in the plasma itself is known as the subtractive method [80]. In the subtractive method the plasma power is measured by measuring the power deposited in the system from when the plasma is on and subtracting the power deposited in the system for the same current value when there is no plasma. Since the power that is deposited in the system is constant between the two measurements, the power deposited just in the plasma can

be measured using equation 3.7. This method has been previously implemented for small volume atmospheric pressure plasmas [81, 82].

$$P = \frac{V_{on} I_{on}}{2} cos(\theta) - I_{on}^2 R_{off} \tag{3.7}$$

To measure the power deposited in the system when there is no plasma, the plasma chamber is filled with nitrogen which will not breakdown with the applied voltages. The input power is then varied over a range of current and voltages so that a value of the resistance can be calculated using $P = I^2R$. The phase is assumed to be constant for the plasma off system and so the simpler equation for power can be used. By plotting power against the square of the current the resistance can be obtained from the gradient and then used to subtract the power deposited in the circuit for the case when the plasma is on.

However the measurement of the phase angle is not as simple as calculating the difference in phases of the voltage and current amplitudes at the driving frequency. There is an instrumental phase that causes a large difference in the measured and true phase angle. If a circuit with a known phase is used the instrumental phase shift can be calculated and accounted for in the measurements. The plasma is very similar to a capacitor, as it is essentially two parallel electrodes across a gap, and the phase angle is very similar to that of a capacitor even when the plasma is on. The phase angle of a capacitor is very close to -90°. However the plasma system is not a perfect capacitor, especially since there is a dielectric between the electrodes, and so the phase angle of the system was measured using a vector network analyser (VNA). Using the VNA the phase angle of the plasma system was found to be -89.5°. By knowing what the phase angle of the system is the instrumental phase shift can be calculated by subtracting the phase angle measured from the FFT from the true phase angle measured using a VNA. The typical value of the instrumental phase shift of this plasma was found to be -48.24°.

This calibration factor should remain constant as long as everything in the circuit remains constant. Even the settings of the oscilloscope need to remain constant as changing the number of volts per division on the display can alter the internal relay circuitry and effect the instrumental phase. This change may only be small but it can have a noticeable affect on the measured powers at the high frequency used in this study. By knowing the plasma power not only is the specific

energy input per molecule of CO_2 known to a much greater accuracy, but it also allows for a more accurate input parameter for global models.

Chapter 4

Zero Dimensional Global Model

The zero dimensional global model used for this work was Global_Kin [83]. Global_Kin consists of three main modules, a plasma reaction chemistry and transport module, a Boltzmann equation solver, and an ordinary differential equation (ODE) solver. Global models provide a computationally cheap method of understanding complex plasma chemistry [84, 85]. The have been extensively used in the field to study complex chemistry systems [86–92]. The plasma reaction chemistry module constructs differential equations for the evolution of the density of the plasma species, the electron temperature, and the gas temperature. Electron temperature dependent rate coefficients are calculated using the Boltzmann equation solver. The Boltzmann equation solver solves the Boltzmann equation for a range of different E/N values which are then interpolated to find the corresponding rate coefficients for the electron temperature calculated by the plasma chemistry reaction module. The differential equations are then integrated by the ODE solver [93].

The plasma chemistry module constructs continuity equations for the neutral 4.1 and charged 4.2 species. N_i and $N_i^{\pm}$ are the densities of the neutral and charged species respectively, D_i and $D_{a,i}$ are the regular and ambipolar diffusivities of species i in the mixture. f_{ji} is the returned fraction of species j when species i hits the wall and γ_j is the wall sticking coefficient of species j and S_i is the reaction source term for a species i and is defined in equation 4.3. The final term represents diffusion due to the gas temperature T_g. The wall sticking coefficients are often not well known but can have a considerable impact on the simulations [94]. In equation 4.3 a_{ij} are the stoichiometric coefficients of species i in reaction j on the

right hand side, RHS, and left hand side, LHS, k_j is the reaction rate coefficient for reaction j.

$$\frac{dN_i}{dt} = -\nabla \cdot \big(- \nabla(D_i N_i) + \sum_j \nabla \cdot (D_j N_j)\gamma_j f_{ji}\big) + S_i - \frac{N_i}{T_g}\frac{dT_g}{dt} \tag{4.1}$$

$$\frac{dN_i^{\pm}}{dt} = -\nabla \cdot [-\nabla(D_{a,i} N_i)] + S_i \tag{4.2}$$

$$S_i = \sum_j (a_{ij}^{RHS} - a_{ij}^{LHS}) k_j \Pi_l N_l^{a_{ij}^{LHS}} \tag{4.3}$$

Equation 4.1 can be simplified by assuming a spatially uniform plasma. Then the second order partial derivatives can be approximated by substituting in a diffusion length Γ, defined in equation 4.4, where x is the length of the reactor, y the width and d the gap between the electrodes. This assumption is justified in a radio frequency plasma as the discharge is continuous and fills the entire plasma reactor. The simplified continuity equation for the neutral species is given in equation 4.5

$$\frac{1}{\Gamma^2} = \left(\frac{\pi}{x}\right)^2 + \left(\frac{\pi}{y}\right)^2 + \left(\frac{\pi}{d}\right)^2 \tag{4.4}$$

$$\frac{dN_i}{dt} = \frac{1}{\Gamma^2}\big(- D_i N_i + \sum_j D_j N_j \gamma_j f_{ji}\big) + S_i - \frac{N_i}{T_g}\frac{dT_g}{dt} \tag{4.5}$$

The diffusivities of the species are estimated from Lennard-Jones potentials and are calculated as a function of the local gas composition for each species. The ambipolar diffusion coefficients are obtained from experimental databases for ions and calculated from the EEDF for electrons. The average gas temperature is obtained from equation 4.6 by accounting for elastic and inelastic collisions with electrons and the enthalpy of heavy particle reactions. Where N is the total gas density, c_p is the specific heat and ΔH_j is the change in enthalpy of reaction j. The first and second terms of equation 4.6 determine the heating due to momentum transfer collisions with electrons and dissociative electron impact processes which are responsible for Frank-Condon heating.

$$\frac{d}{dt}(Nc_pT_g) = \sum_i \frac{3}{2} n_e v_{mi} \frac{2m_e}{M_i} k_b(T_e - T_i) + \sum_j n_e k_j N_j \Delta\epsilon_j - \sum_j \Delta H_j \qquad (4.6)$$

The electron temperature is obtained from equation 4.7 from the energy gained by Joule heating and lost from elastic and inelastic collisions. Where **J** and **E** are the current density of electric field in the discharge, v_{mi} is the electron momentum transfer collision frequency with species i. k_l is the reaction rate coefficient of the l^{th} electron impact process and N_l is the density of the gas phase collision partner and $\Delta\epsilon_l$ is the change in electron energy.

$$\frac{d}{dt}\left(\frac{3}{2} n_e k_B T_e\right) = \mathbf{j} \cdot \mathbf{E} - \sum_i \frac{3}{2} n_e v_{mi} \left(\frac{2m_e}{M_i}\right) k_B(T_e - T_i) + \sum n_e k_l N_l \Delta\epsilon_l \qquad (4.7)$$

In order to account for the flow conditions seen in the experimental set-up the global model, Global_Kin, has been converted to a pseudo-one-dimensional plug flow model with the introduction of a flow velocity v_x and taking account of the gas expansion at a constant pressure. The change in the speed of the gas is obtained using the conservation of mass flux and is given in equation 4.8 where ρ is the mass density, obtained from the averaged molecular weight and number density. By integrating the flow velocity it is possible to give the location of a gas particle as a function of time.

$$\frac{dv_x}{dt} = -\frac{v_x}{\rho} \frac{d\rho}{dt} \qquad (4.8)$$

As the composition of gases within the plasma is constantly changing throughout the operation the Boltzmann solver can be called periodically to generate new rates for the electron impact reactions to accurately represent the changing electron temperature of the plasma. This is because as the gas composition changes the electron energy distribution function changes.

4.1 CO_2 Plasma Global Model

Two different reaction sets were created for the argon and helium discharge with CO_2 with a full list of the included species given in Appendix A. The full reaction set is given in Appendix B. The species included are ground state neutrals, vibrationally and electronically excited neutrals, positive and negative ions and electrons. The reactor in the model has the same dimensions as in the experiment and both the flow and plasma power are also input parameters. The model can be assumed to accurately reflect reality if the plasma chemistry closely matches the species densities measured in the experiment. It is then possible to determine the underlying mechanisms of the plasma chemistry by analysing the reaction rates calculated by the model. Detail of the reaction rates and cross-sections used are provided later in the thesis when analysing the chemical reaction pathways.

4.2 Pathway Analysis, Pumpkin

Global_Kin includes a pathway reduction method for plasma kinetics models module called PumpKin [95]. In plasma chemistry systems long lived species of interest are often produced by very short lived species to create the conditions necessary for usually unfavourable reactions to occur. PumpKin allows for the short lived species to be combined between the long lived species. In the context of CO_2, PumpKin will show the pathway between CO_2 to CO and the intermediate steps, whether that is electronic impact excitation or vibrational energy exchange, etc.

A pathway in PumpKin is defined as a linear combination of reactions, each of which is weighted by a natural number. PumpKin builds a pathway so that it has zero net production of fast species which is defined by the time of interest parameter in the model. In order to obtain the pathways the algorithm used by PumpKin starts by creating a set of pathways consisting of one reaction each, including all reactions. Then the pathways that produce the species with the shortest lifetime are combined with the pathways that destroy it to produce a pathway with zero net production. This then continues until all the species with a lifetime shorter than the defined longest lifetime to be considered have been put into pathways. The pathways that then have a rate lower then a certain value are ignored to avoid an overly large list of reactions.

Chapter 5

A Comparison of Carrier Gases

5.1 Comparison of Yield and Energy Efficiency against specific energy per molecule

In this chapter ex-situ FTIR results are presented for the atmospheric pressure radio frequency plasma using both argon and helium as a carrier gas. The FTIR is used to measure the concentrations of both CO and CO_2 in the far effluent to ensure that the gas is under standard temperature and pressure during the measurements, as the calibration gases would be. It is also possible to measure the amount of ozone, O_3, in the FTIR if the concentration is high, but this has not been a focus of this work, though plasmas of this type are known to produce significant amounts of ozone [96].

The FTIR was used to measure the CO_2 and CO concentrations before the plasma was ignited and during the running of the plasma in order to calculate the yield of CO, the energy efficiency and the specific energy input per molecule of CO_2. The specific energy input per molecule of CO_2 depends on a number of factors including, the admixture of CO_2, the plasma power and the flow rate of the gas. For the purposes of these results the plasma power is 30 W and the gas flow rate is one standard litre per minute, slm, unless otherwise stated. Figures 5.1 and 5.2 show the yield and energy efficiency, respectively, for both argon and helium carrier gases and experiment and simulations. The simulations were performed using the species and reaction set defined in appendices A and B. The plots are with respect to the specific energy input per molecule of CO_2

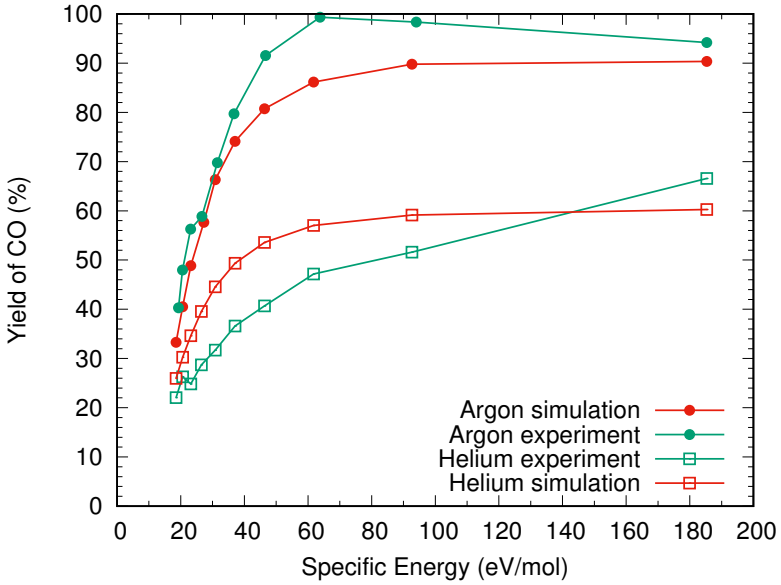

FIGURE 5.1: The yield of the radio frequency atmospheric pressure plasma with respect to the specific energy per molecule of CO_2. To vary the specific energy per molecule of CO_2, the CO_2 admixture, in either a helium or argon carrier gas, is varied between 0.25 and 2.5%. The plasma power and flow rate were kept constant at 30 W and 1 slm respectively. It is clear that as the specific energy is reduced the yield of CO will in general reduce. Greater yields are also seen in an argon carrier gas in comparison to helium.

and clearly demonstrate the trade off between yield and energy efficiency seen in plasma based conversion of CO_2 [38].

Figure 5.1 shows that the yield decreases with decreasing specific energy inputs per molecule of CO_2. This is to be expected because as the energy input per molecule of CO_2 decreases the conversion of CO_2 would be expected to decrease by considering an energy balance. For the highest specific energy inputs the yield starts to remain constant as the specific energy input increases. In the case of the experiment for the argon carrier gas, this can be explained simply by the yield reaching nearly 100% meaning that either there is some recombination in the effluent that cannot be avoided or simply there are the errors in the FTIR measurements. For the argon simulations the yield does not quite reach the 98% maximum seen, but it does reach just below 90% yield before becoming constant with specific energy input increases. This can be explained by the inaccuracy in the reaction rates used for the conversion of CO_2. It could also be due to the lack of knowledge in the quenching rates for vibrationally excited CO_2 molecules with the carrier gas. For the small admixtures of CO_2 the mean electron energy is quite high, between 2-3 eV, meaning that direct electron impact dissociation from all

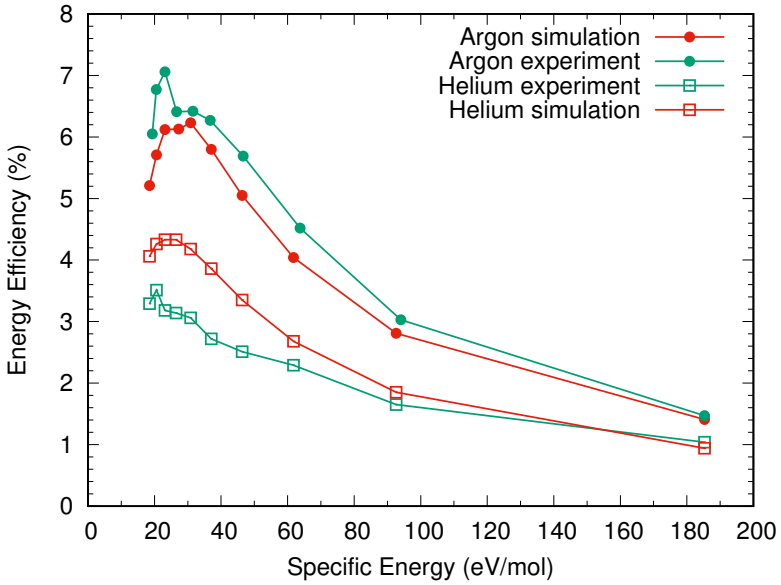

FIGURE 5.2: The energy efficiency of the radio frequency atmospheric pressure plasma with respect to the specific energy per molecule of CO_2. To vary the specific energy per molecule of CO_2, the CO_2 admixture, in either a helium or argon carrier gas, is varied between 0.25 and 2.5%. The plasma power and flow rate were kept constant at 30 W and 1 slm respectively. It is clear that as the specific energy is reduced the energy efficiency of the conversion of CO_2 will in general increase. Greater efficiencies are also seen in an argon carrier gas in comparison to helium.

states of CO_2 is much more likely and the cross sections for direct electron impact reactions of CO_2 are not well known [97].

In the case of helium the yield of CO is significantly lower for all values of specific energy input as seen in microwave plasmas at pressures of 0.5 Torr [98]. The reasons for this will form a large part of the thesis. However a very similar trend is seen in the yield becoming independent of energy input for very high specific energy inputs. As the specific energy input in this figure is only varied by changing the admixture this means at a certain point decreasing the CO_2 admixture in order to increase the electron temperature is not leading to a significant increase in the yield. The reasons for this will be explained in detail throughout this and the subsequent chapter.

In Figure 5.2 the opposite trend is seen in energy efficiency compared to the yield. In general the energy efficiency of the conversion of CO_2 increases with decreasing specific energy input. However in all cases there is a maximum seen in the energy efficiency where increasing the CO_2 admixture to lower the specific energy input causes such a decrease in the yield of CO that the energy efficiency

decreases. Since the energy efficiency for constant flow rates and plasma powers will only depend on the yield of CO, argon is shown to be the much more efficient choice of carrier gas for these plasmas. Since only the admixture of CO_2 is varied in order to vary the specific energy input, the specific energy input is not the ideal parameter to plot in these graphs to explain the features seen. However the specific energy input is independent of plasma reactor choice and so is a useful parameter to include for comparison with other plasma sources. The plasmas that have reported the highest energy efficiencies have specific energy inputs per molecule of CO_2 of less than the 2.9 eV required to convert CO_2 into CO [61]. This limits the yield but is considered the best method for obtaining very high energy efficiencies [61]. This plasma however clearly shows that reducing the specific energy input to such levels will not provide higher energy efficiencies and in fact a plasma is unlikely to be obtained for the very high CO_2 admixtures needed for such low specific energy inputs.

5.2 Comparison of Yield and Energy Efficiency against admixture

5.2.1 Yield

Plotting the yield of CO with respect to CO_2 admixture shows much the same trend as with the plot against specific energy input, as shown in Figure 5.3. For the high admixtures of CO_2, 2% and over, there is a clear discontinuity in the trend of the yield for the argon experimental data and a similar effect is seen in helium for admixtures over 2%. However, this effect is not seen in the simulations. This discontinuity can be explained by the plasma transitioning from alpha mode into a hybrid gamma mode.

In this mode secondary electron emission from the sheath starts to become a important source for electrons and the electron density increases [99]. Since the conversion of CO_2, in plasmas of this type, is believed to be due to electron impact reactions it is expected that by transitioning into gamma mode and increasing the electron density an increase in the yield of CO would be observed. The transition into gamma mode can also be observed by an increase in the emission of light from the plasma and this increase in light can clearly be seen in Figure 5.5, the

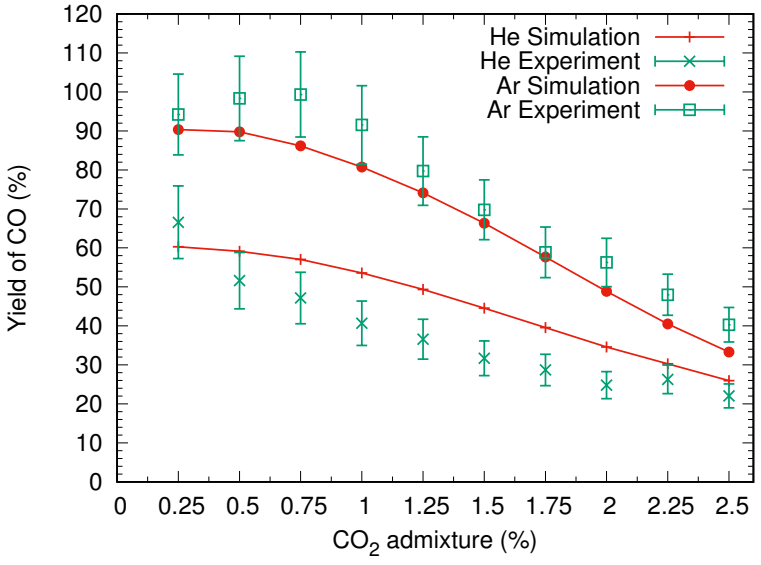

FIGURE 5.3: The yield of the radio frequency atmospheric pressure plasma with respect to the admixture CO_2 in either a helium or argon carrier gas. The admixture is varied between 0.25 and 2.5%. The plasma power and flow rate were kept constant at 30 W and 1 slm respectively. It is clear that as the admixture of CO_2 is increased the yield of CO will in general decrease.

alpha to gamma mode transition has been previously observed in atmospheric pressure plasmas [77, 100, 101]. Figure 5.5 also shows that the increased emission is not throughout the whole plasma and so the plasma is said to be in a hybrid gamma mode. The simulations do not take into account gamma mode as they use a single electron energy distribution function for the entire plasma and this has been shown to not properly take into account the effects gamma mode has on the sheath [102]. The largest source of error in the measurements comes from the fit of the calibration curve with the mass flow controllers and voltage and current probe measurements also providing a source of error.

5.2.2 Energy Efficiency

It is shown in Figure 5.4 that the maximum in energy efficiencies seen occur at specific CO_2 admixtures. This means that they are an effect of the reduced electric field, E/N, and not the electron density, which is difficult to determine in a plot against the specific energy input. In the case of argon there are two peaks in the energy efficiency for the experimental results. This is again due to the plasma entering a hybrid gamma mode for the CO_2 admixtures of 2% and higher. The increase in the electron density from gamma mode causes more CO_2

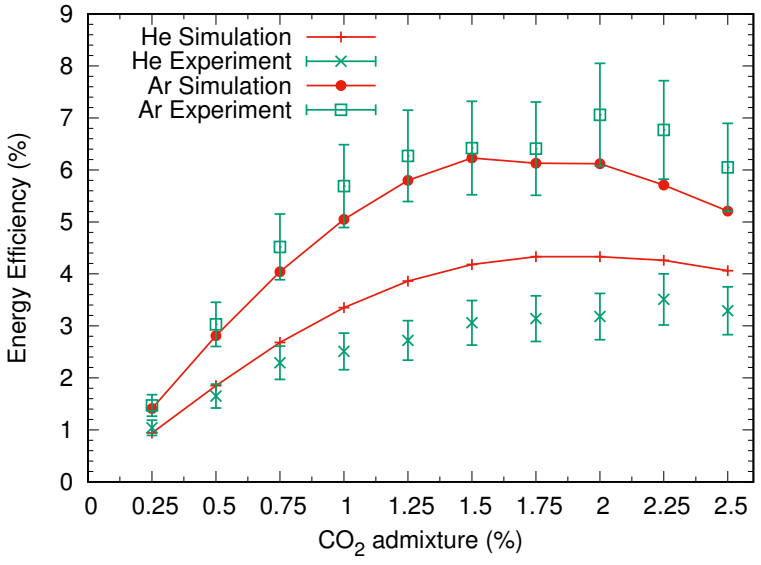

FIGURE 5.4: The energy efficiency of the radio frequency atmospheric pressure plasma with respect to the CO_2 admixture in either a helium or argon carrier gas. The admixture is varied between 0.25 and 2.5%. The plasma power and flow rate were kept constant at 30 W and 1 slm respectively. When the admixture of CO_2 is varied the energy efficiency can also vary considerably with the maximum in the energy efficiency not corresponding to the maximum CO_2 admixture. This is because of a trade off between the increasing number of molecules of CO_2 from the increasing admixture and the electron temperature decreasing as the CO_2 admixture is increased.

to be converted than would be expected in alpha mode for the same plasma power and the increase in yield is enough to also increase the energy efficiency. All of the simulations are run in alpha mode and so we only see a single peak in the energy efficiency for a CO_2 admixture of 1.5% which is in a very similar point to the observed maximum alpha mode peak in the experiments. This means that there is some confidence that the simulations are accurately simulating the electron dynamics and the reduced electric field in alpha mode. This maxima is different from what has been reported in other CO_2 argon plasmas [103], where a one to one ratio was found to give the best yields, nearly 80%. This was however for a nanosecond pulsed plasma and so the plasma dynamics are very different.

For the case of helium in Figure 5.4 the energy efficiency is much lower than for the argon case. This is due to the yield of CO being lower than in argon. Since the plasma power and flow rate are held constant the only factor effecting the energy efficiency between the two carrier gases is the yield. There is not as much of a defined peak for the helium case showing that the carrier gases give very different reduced electric fields as well as electron densities. For the helium carrier

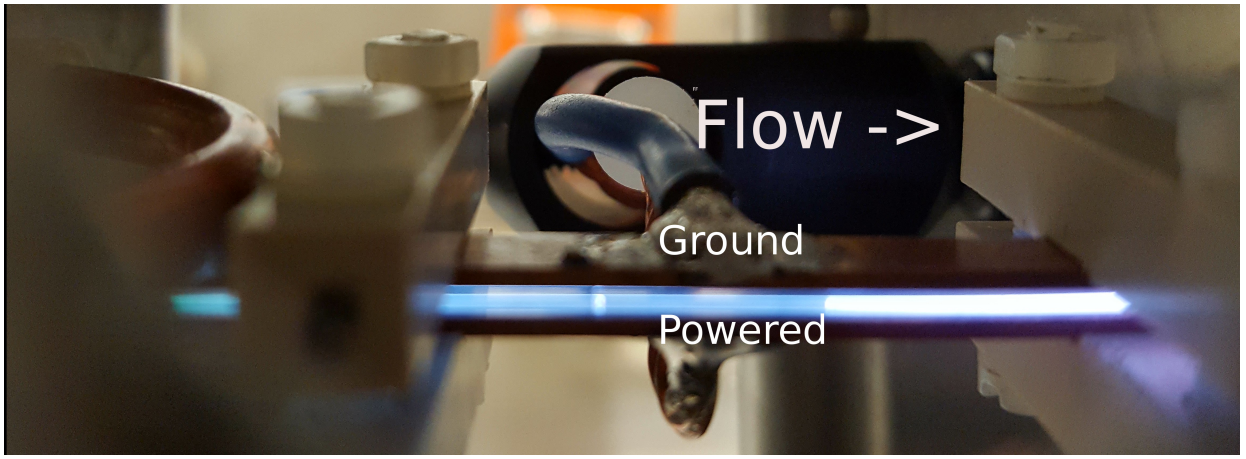

FIGURE 5.5: A photo of the plasma showing the difference between alpha and gamma mode observed for high CO_2 admixtures. This is known as a hybrid gamma mode as the plasma exists in both alpha mode and gamma mode in different regions. In gamma mode an increase in the electron density is expected and this leads to an increase in the yield of CO and hence the energy efficiency of the conversion.

gas simulations the peak in the energy efficiency is found to be for a CO_2 admixture of 2% whilst for the experiments it is difficult to see exactly where the maximum in the energy efficiency would occur due to the presence of a hybrid gamma mode for the highest CO_2 admixtures. There is also a much smaller difference in-between data points in the case of helium meaning that the determining of a peak in the energy efficiency is much more susceptible to errors in the measurements.

Changing the reduced electric field has the effect of changing the mean electron energy, and therefore electron temperature, of the plasma. In general the more degrees of freedom a gas has in a plasma the lower the mean free path the electrons will have and this will reduce the mean energy of the electrons. Therefore noble gas plasmas like argon and helium have higher electron temperatures than plasmas with di or tri-atomic molecules. Adding in more CO_2 to the plasma has the effect of reducing the electron temperature of the plasma and since the electron temperature of these plasmas is lower than the dissociation energy of CO_2 and therefore multiple steps are needed in order to dissociate CO_2 for the majority of electrons in the plasma. The lowering of the electron temperature then has the effect of making fewer electrons hot enough to be able to excite CO_2 in a manner that will cause dissociation. There are still a small number of electrons that are energetic enough to directly dissociate CO_2.

However increasing the CO_2 admixture also increases the number of molecules

in the plasma that can be converted and there is a trade off between the hotter electron temperatures and the number of CO_2 molecules in the plasma. Since this effect is due to the reduced electric field changing the plasma power has no effect on where the peak occurs but it will change the absolute values of the yield and energy efficiency for each admixture. The plasma power has no effect on the peak in the energy efficiency because the energy the electrons gain in the plasma is from being accelerated in the electric field, which is determined by the mean free path and the pressure length product. Changing the plasma power will only affect the electron density and not its energy. Therefore changing the plasma power does have an effect on the yield and the energy efficiency as increasing the power increases the electron density for the same electron temperature means that there are more electrons able to dissociate CO_2 and the yield will increase. Since the specific energy input per molecule of CO_2 is increasing with increasing power the energy efficiency may not in-fact increase. The electron density scales approximately linearly with plasma power and so the effect on the yield is also expected to be linear [104].

5.3 Absolute Density of CO

The trends seen in the energy efficiency plots with respect to CO_2 admixture are very similar to the trends seen in absolute CO density for the conditions, shown in Figure 5.6. The maximum in the CO density occurs at the same point as the maximum in the energy efficiency. It is expected that there would be a peak in the CO density for an admixture variation as a plasma cannot be ignited for very high admixtures or pure CO_2, in this set-up, and therefore a plasma of very unenergetic electrons would be expected for admixtures close to the maximum possible that would produce little CO. Consequently, the peak in the energy efficiency is seen because there is a certain admixture of CO_2 that produces the most CO and this is the most energetically favourable admixture. This does not explain why adding more CO_2 into the plasma does not yield more CO. The peaks occurring at a certain admixture suggest that the maximum in CO density is an effect of the reduced electric field, E/N.

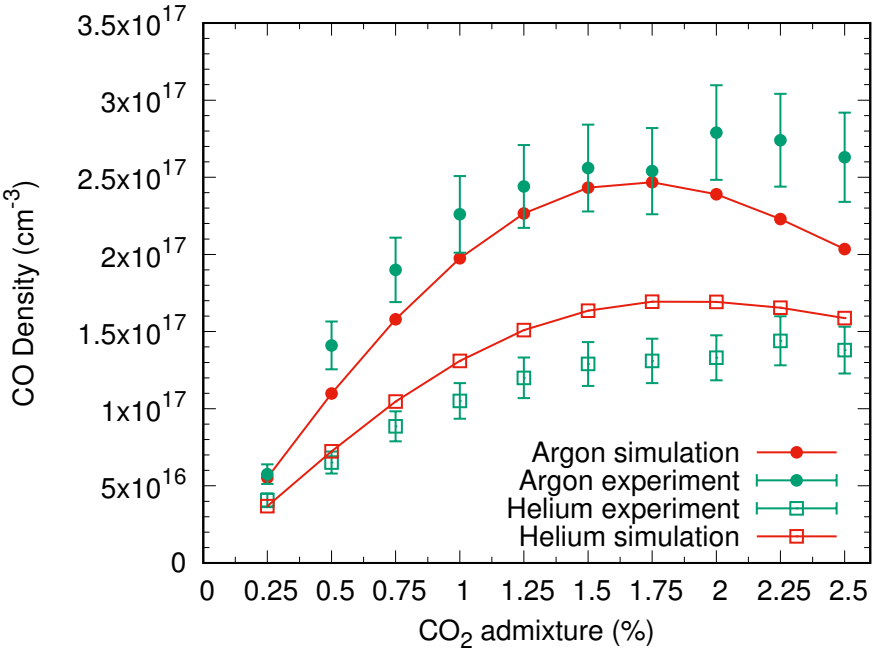

FIGURE 5.6: The absolute densities of CO for argon and helium plasmas with a plasma power of 30 W and a flow rate of 1 slm. The trend of the absolute densities of CO follows a very similar trend to that of the energy efficiencies. Where the maximum in the energy efficiency occurs there is a maximum in the CO density, meaning that in order to maximise the energy efficiency of an admixture variation the CO density must also be maximised.

5.4 Electron Temperature and Densities for the Two Carrier Gases

Due to helium and argon having different ionisation energies and reaction rates the electron density for the same admixture of CO_2 will be different. Figure 5.7 shows the difference between both the electron density and electron temperature of the two different carrier gases. The electron temperature and density are higher in argon compared to helium and this will partly explain the higher yields of CO seen in the argon carrier gas. A higher electron density is expected in an argon plasma due to argon having a lower ionisation energy than helium. However the higher electron temperature observed in the argon plasma is not at first intuitive because lower ionisation energies tend to lead to an electron energy distribution function with more electrons having lower energies. In general a plasma consisting of a gas with higher ionisation energy will have a higher electron temperature.

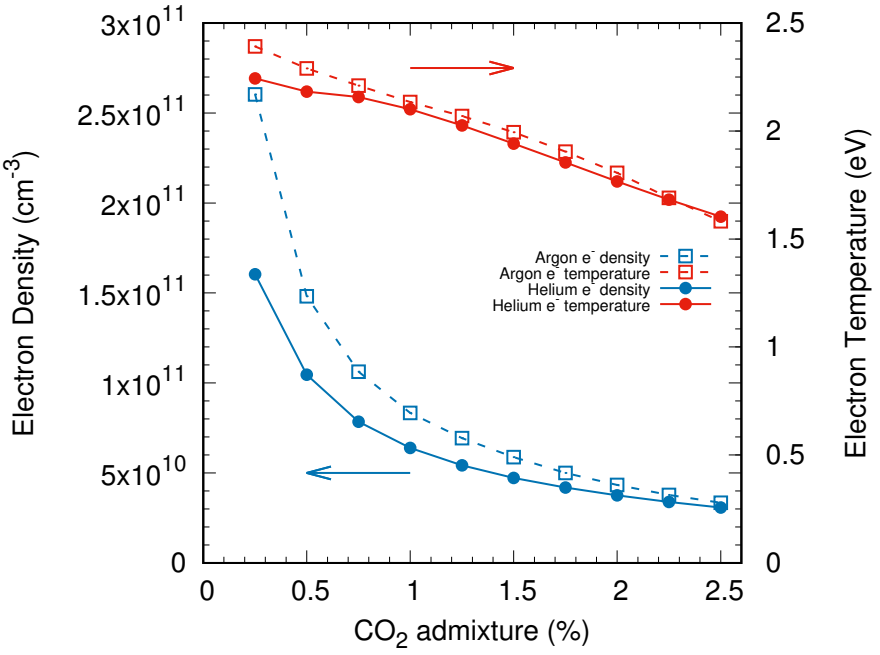

FIGURE 5.7: Both the electron temperature and density decease with increasing CO_2 admixture for both a helium and an argon carrier gas. The electron density is higher and temperature is higher in argon than in helium and this provides at least part of the explanation for the difference observed in the yield of CO.

5.4.1 Carbon Monoxide Density as a Function of Electron Density

Figure 5.8 shows the carbon monoxide density of the argon plasmas as a function of the electron density in the simulations. This figures shows that not only is there not a linear dependence on electron density but the simulations with higher electron densities do not yield the highest carbon monoxide densities. This is because as the CO_2 admixture is increased there is more CO_2 to convert, however increasing the CO_2 admixture also lowers the electron density and temperature. This is in part due to the increased likelihood of electron recapture occurring with higher CO_2 admixtures leading to higher negative ion densities and therefore lower electron densities as negative charge density must equal positive charge density for quasi-neutrality to hold. This figure shows that it is important to consider both the electron temperature and density in order to understand plasma chemistry.

If direct electron impact dissociation were the main cause of dissociation in these plasmas a more linearly dependence on electron density would be expected for the carbon monoxide density. The carbon monoxide density is clearly not

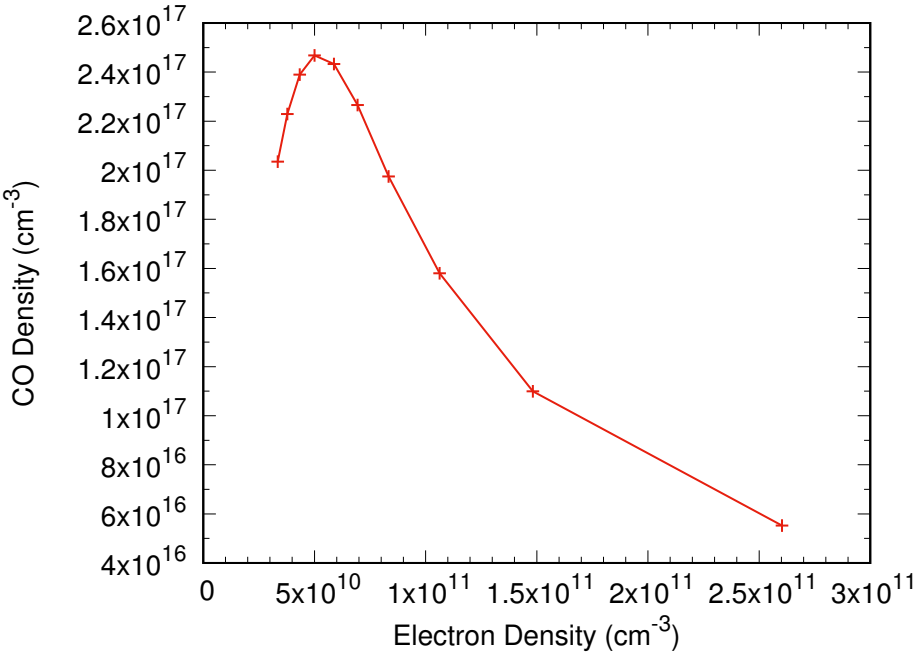

FIGURE 5.8: The carbon monoxide density as a function of electron density for the simulated argon case. The carbon monoxide density does not depend linearly on the electron density and therefore it is likely that vibrational states of CO_2 are responsible for causing the dissociation of CO_2 as if direct electron impact dissociation were responsible a linear dependence would be expected.

linearly dependent on the electron density and therefore it appears that the vibrational states of CO_2 are important for the dissociation of CO_2 in these plasmas. Direct electron impact dissociation depends on the electron density and the CO_2 density as well as the energy of the electrons and therefore increasing the CO_2 admixture should increase the direct electron impact dissociation with a linear dependence on the electron density, assuming that the electron energy distribution function keeps roughly the same shape with changing CO_2 admixture.

5.4.2 Electron Energy Distribution Functions

For a helium plasma a higher electron temperature is expected compared to an argon plasma because the ionisation energy is higher in helium than argon. In order for electron losses, to the walls for instance or in attachment reactions, to be balanced by production the EEDF must have a higher energy tail in helium, as shown in Figure 5.9. However this assumes that the main ion in the plasma is either helium or argon and this is not the case in either plasma. In both cases the dominant ion in the plasmas come from species in the admixture. Therefore less

energetic electrons are required to balance the production and loss of electrons in both argon and helium plasmas. In the argon case the dominant positive ion is CO_2^+ and in helium it is O_4^+, as observed in helium oxygen plasmas [86], produced from O_2^+. Both of the dominant ion species have ionisation energies much lower than helium and similar to each other and therefore would provide similar electron temperatures. In addition to this the electro-negativity of a plasma can increase the electron temperature of a plasma as fewer electrons to ionise species must be balanced with higher energies. The argon plasma was found to be slightly more electronegative than the helium plasma with O_3^- the dominant negative ion in both cases. This would lead to slightly higher electron temperatures in argon plasmas as observed in Figure 5.7.

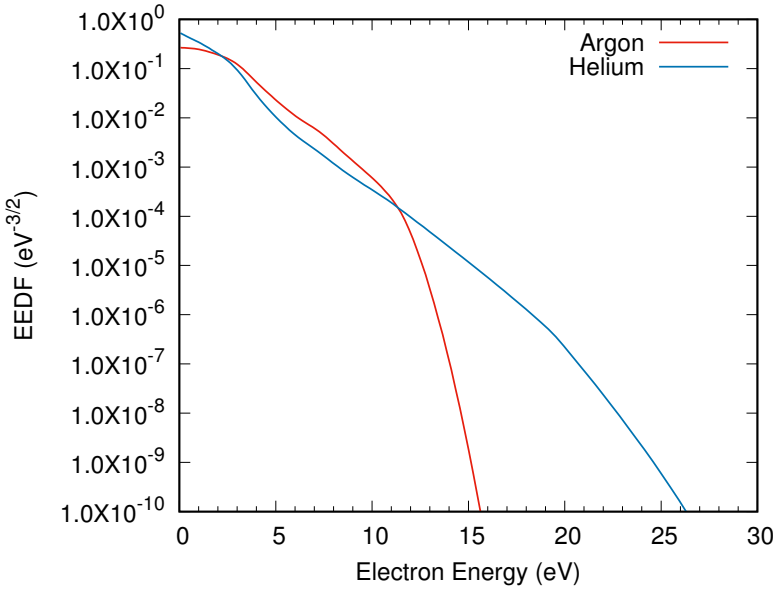

FIGURE 5.9: The electron energy distribution functions of an argon plasma with a 1.5% CO_2 admixture and a helium plasma with a 1.5% CO_2 admixture. The helium plasma has more electrons distributed in the high energy tail and the very low energy electrons however these areas are not advantageous for CO_2 dissociation. Since CO_2 has a dissociation energy of 5.5 eV electrons close to this value are the most important and in this region argon plasmas are more favourable.

The higher electron temperatures in argon can also be explained by looking at the electron energy distributions functions (EEDF) for two plasmas with the same admixture as shown in Figure 5.9. Both EEDF's in this figure were calculated using a 1.5% CO_2 admixture, in Bolsig+ [24], and the same power deposition with a mean electron energy corresponding to the same mean electron energy as in Figure 5.7. The most obvious difference between the two cases is that the tail of the EEDF in helium continues on to much higher energies than in argon. The

threshold energies for inelastic energy losses are higher in the case of helium and so to obtain a numerical solution for the power balance equation in steady state more electrons of high energy are required than in the case of argon. Significant inelastic losses can occur in helium plasmas even for relatively low electron temperatures. In the case of a Maxwellian EEDF for both helium and argon the shape of the EEDF is the same and then a higher electron temperature is observed in helium compared to argon, as expected. However the main conclusion to be drawn by looking at the differences between the helium and argon plasmas is that merely the electron temperature and density do not provide enough information from which to draw a conclusion and the EEDF is far more important in determining the processes that govern plasma chemistry.

5.5 The Evolution of the Plasma Species

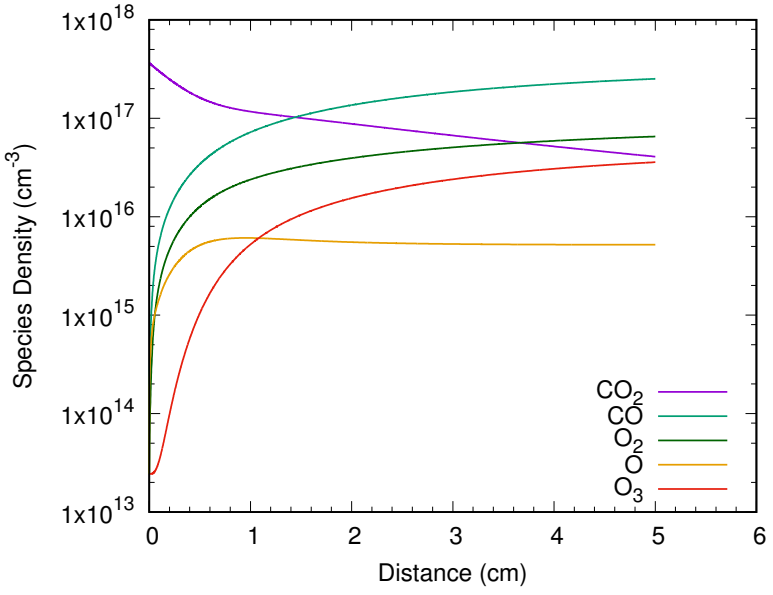

FIGURE 5.10: The density evolution of the main chemically active ground state neutral plasma species. The simulation was performed in an argon plasma with a 1.5% CO_2 admixture and a plasma power of 30 W. It is clear that most of the CO_2 converted is forming into CO and O_2 which are the desired products. There is also a significant amount of ozone formation from the atomic oxygen and molecular oxygen produced by the dissociation.

Although the global model simulations are zero dimensional in space because there is a fixed known flow rate it is possible to equate the time step with a change in distance. It is possible to plot the evolution of the plasma species as a function of distance through the plasma, as shown in Figure 5.10. In this figure the main

neutral ground state plasma species, excluding argon, densities are shown as a function of their distance through the plasma. The simulation was performed with an argon carrier gas and a 1.5% CO_2 admixture with a constant power of 30 W and a flow rate of 1 slm. It is evident that the main products of the plasma chemical reactions are CO and O_2, as expected for the dissociation of CO_2. How the molecular oxygen formed is of interest in determining the most efficient means of dissociating CO_2. Molecular oxygen in this plasma will be formed in one of two ways, either atomic oxygen produced from CO_2 dissociation will recombine with another atomic oxygen or the oxygen atom can further react with another CO_2 and produce more CO and O_2. Using atomic oxygen to produce more CO will lead to more efficient dissociation as the product of the first dissociation reaction is being used to cause further dissociation and due to the chemical potential energy the oxygen atom possesses, the secondary reaction will require less energy.

There is also a significant amount of ozone produced throughout the plasma which is known to be formed through the three body recombination of atomic and molecular oxygen. This is an unfavourable reaction as it prevents the atomic oxygen being used to further dissociate CO_2 and produces an undesirable product. Ozone can also react very strongly with CO, potentially destroying the desired product. However this reaction is only likely in the presence of a catalyst [105] and is not a problem in the set-up used in the experiments, due to the lack of a catalyst. It is also possible to easily remove ozone from the effluent through the use of a scrubber. Ozone scrubbers are also common and cheap to produce and so the ozone produced is easy to remove from the effluent without affecting the CO produced and is therefore only of concern for the recycling of atomic oxygen.

5.5.1 Simulations of the Effluent

In order for the experimental measurements in the FTIR to be as accurate as possible a large amount, up to two metres, of swagelok piping was placed between the plasma and the gas cell of the FTIR. This is to ensure that the gas temperature for the plasma measurements is at standard temperatures as the calibration gas was. Therefore there is a question as to whether there is a significant amount of recombination of CO back into CO_2, in the effluent, before the measurement is taken.

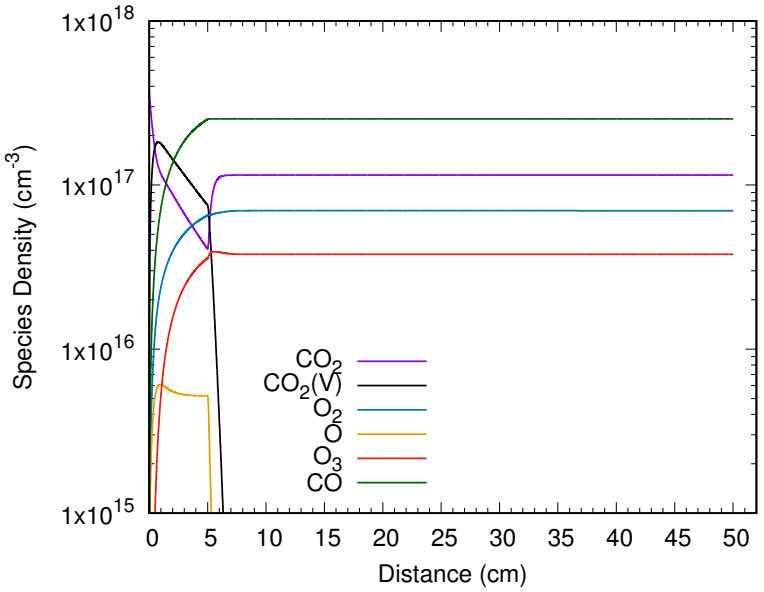

FIGURE 5.11: The density evolution of the main chemically active ground state neutral plasma species extended into the effluent. The simulation was performed in an argon plasma with a 1.5% CO_2 admixture and a plasma power of 30 W. There is no significant recombination of CO back into CO_2 seen in the simulation meaning that the CO densities at the end of the simulation can be compared to the CO densities measured in the FTIR. There is also a very rapid quenching of the remaining vibrationally excited CO_2 levels back to the ground state and a very sharp drop off in atomic oxygen density. The remaining atomic oxygen is combining with molecular oxygen to form ozone in the effluent which is remaining relatively stable. This is to be expected since ozone can be detected by the FTIR.

It is possible in the model to turn off the input power after a certain time and continue the simulation for longer, this enables simulations of the plasma and the effluent to be performed. Figure 5.11 shows the 1.5% CO_2 admixture in argon shown in the previous figure continued into the effluent. This figure clearly shows that the density of CO is not significantly changed throughout the effluent and there is very little recombination of CO into CO_2. There are however significant changes in other species. The atomic oxygen density drops off drastically and quickly, largely forming ozone through the three body recombination with O_2 [86]. The ozone density then remains largely stable in the effluent which is expected as it can be detected in the FTIR. There is also a large change in the density of CO_2. At first this appears to be at odds with the change seen in the density of CO but the CO_2 density shown is just the ground state density and the large increase seen is from the quenching of vibrationally excited species, shown in black. The figure also shows that CO_2 is very strongly quenched and quickly returns to the ground state after leaving the plasma. The vibrational density of CO_2 in the plasma

is very high and is almost always higher than the ground state CO_2 density in the plasma. The vibrational density of CO_2 shown in the figure is the sum of all vibrational CO_2 states, symmetric and asymmetric. Although the total vibrational CO_2 density is quite high the majority is comprised of low energy asymmetrical and symmetric stretches that are far from the dissociation energy of CO_2.

5.5.2 Evolution of Species in Helium

The evolution of the species densities in helium is much the same as in argon, as shown in Figure 5.12. The simulation shown in the figure is for the same conditions as the argon case above, 1.5% CO_2 admixture, 30 W plasma power and 1 slm flow rate. The Figure also shows that the evolution of the plasma species shown is very similar to the argon case only the species take longer to reach higher densities and as a result do not reach as high densities for the same period of time. In both cases the species densities have yet to reach equilibrium values meaning that the yield of CO could potentially be increased. However if the flow rate is halved to try and increase the yield, the yield must double to attain the same energy efficiency as before.

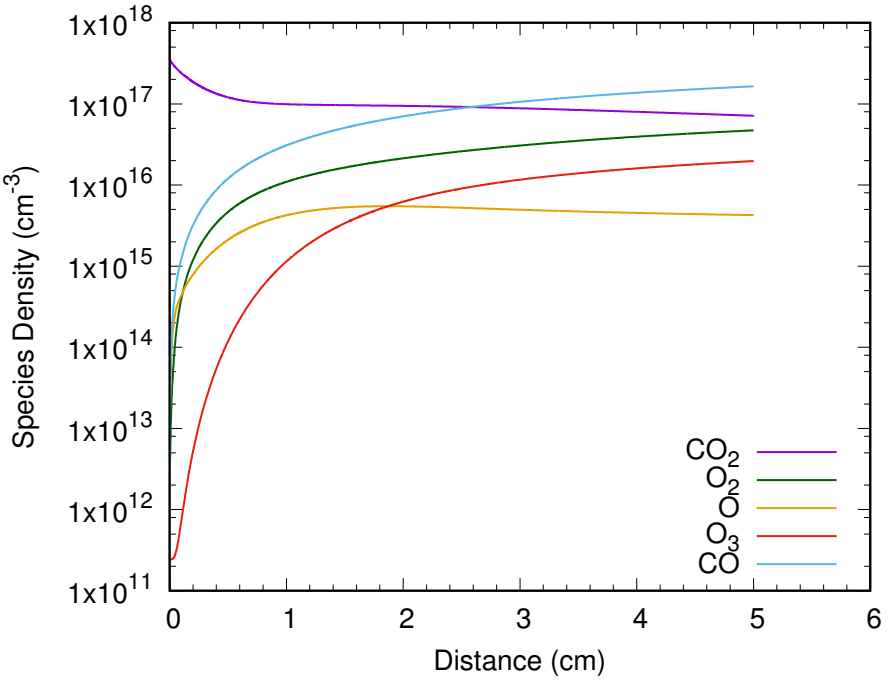

FIGURE 5.12: The evolution of the main chemically active ground state neutral plasma species in a helium carrier gas with a 1.5% admixture of CO_2, a plasma power of 30 W and a flow rate of 1 slm. The species densities evolve in a very similar manner to the argon plasmas however the conversion is clearly slower.

Since the species densities evolve in a very similar manner it may reasonably be construed that the processes behind the dissociation of CO_2 are very similar between helium and argon. This would mean that the main differences between the CO_2 conversions observed in helium and argon plasmas are caused by the electronic properties of each plasma, such as the EEDFs and electron temperatures and densities.

5.6 Varying the Flow Rate

The figures of the evolution of the plasma species show that the carbon monoxide density is not saturated at the end of the plasma for the 1 slm flow rate. The yield of CO could be increased by decreasing the flow rate and would also decrease by increasing the flow rate. Figure 5.13 shows the simulation and experimental results for a flow variation of a 1.5% CO_2 admixture with a constant plasma power of 30 W.

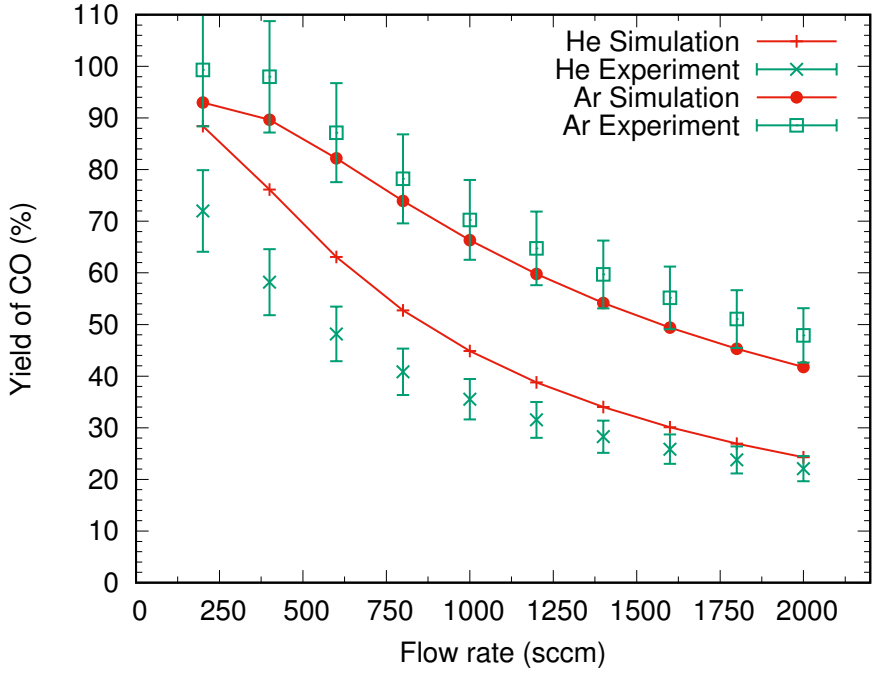

FIGURE 5.13: The yield of CO as a function of flow rate. The CO_2 admixture was kept constant at 1.5% and the plasma power was kept at 30 W. The simulation and experimental results are in good agreement for argon and once again the helium simulation over-predicts the yield of CO but the agreement becomes much better for high flow rates. The figure shows that an increased residence time increases the yield of carbon monoxide even for relatively high CO_2 admixtures.

Decreasing the flow rate has the effect of increasing the residence time and if the gas spends a longer period of time in the plasma it is expected that more CO_2 would be converted and therefore more CO produced as the figure shows. Figure 5.13 shows that even for relatively high CO_2 admixtures used in these measurements the maximum yield obtained is over 90% and therefore if energy efficiency is unimportant and the focus of the application is the density of CO produced simply increasing the residence can obtain almost 100% yields. These results also show that for applications were different ratios of CO to CO_2 are desired the flow rate through the plasma can be changed to get a wide range of different mixtures with the potential to increase the flow rate further.

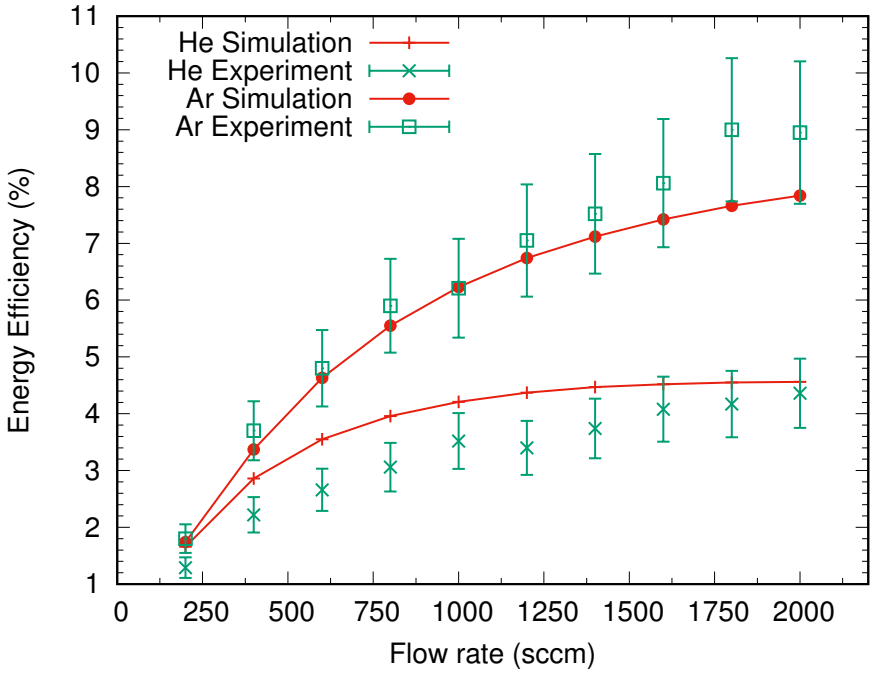

FIGURE 5.14: The energy efficiency of the conversion of CO_2 as a function of flow rate. The CO_2 admixture was kept constant at 1.5% and the plasma power was kept at 30 W. The simulation and experimental results are in good agreement and the energy efficiency is shown to keep increasing, within error, with increasing flow rate with a new maximum energy efficiency of 9.00% obtained for a 1.8 slm flow rate in an argon carrier gas.

If the residence time is increased the specific energy input per molecule of CO_2 would increase and the energy efficiency would decrease and the opposite would be true for decreasing the residence time. Figure 5.14 shows that the energy efficiency does indeed decrease with decreasing flow rate despite the increase in yield and the increase in the flow rate up to a new maximum energy efficiency of 9.00% for the 1.8 slm flow rate in argon. The energy efficiency is likely to keep increasing with

flow rate with the 1.8 slm peak being within the error of the measurement and due to the error in the plasma power as the 1.8 slm measurement had a plasma power of 28.75 W whilst the 2 slm measurement had a plasma power of 30.12 W and this difference produces the peak not seen in the simulation. Since the conversion remains higher in argon the energy efficiency once again remains higher. In order to greater understand the trends observed in this chapter it is possible to calculate the reactions in the model that provide the greatest yields of species to gain insight into the plasma that is not possible to measure experimentally.

Chapter 6

Pathway Analysis

6.1 Main Dissociation Channels in CO_2

The main idea behind the efficient dissociation of CO_2 is through the population of highly energetic vibrational states of CO_2 as this will negate the need to use very high temperatures and would also be more efficient than direct electron impact dissociation which requires energies higher than the dissociation energy. Through analysing the reaction rates of all the reactions in the global model it is possible to determine the most prominent reaction pathways and determine whether the reactions desired for efficient CO_2 are responsible for most of the dissociation of CO_2 or whether direct electron impact dissociation or thermal effects dominate.

The accuracy of the pathway analysis results depends on the accuracy of the reaction rates of the model [106]. Since not all the reaction processes of vibrationally excited CO_2 states are known and those that are not necessarily known with complete certainty, the results of the pathway analysis must be taken in context and whilst they are unlikely to give an exact picture of the exact contributions from different pathways it is possible to determine with some degree of accuracy whether the asymmetric states of CO_2 play a role in the dissociation process.

6.1.1 Dissociation Pathways of CO_2 in Argon

Figure 6.1 shows the main dissociation pathway of the argon CO_2 plasma for admixtures varied between 0.25 and 2.5%. The figure shows that most of the

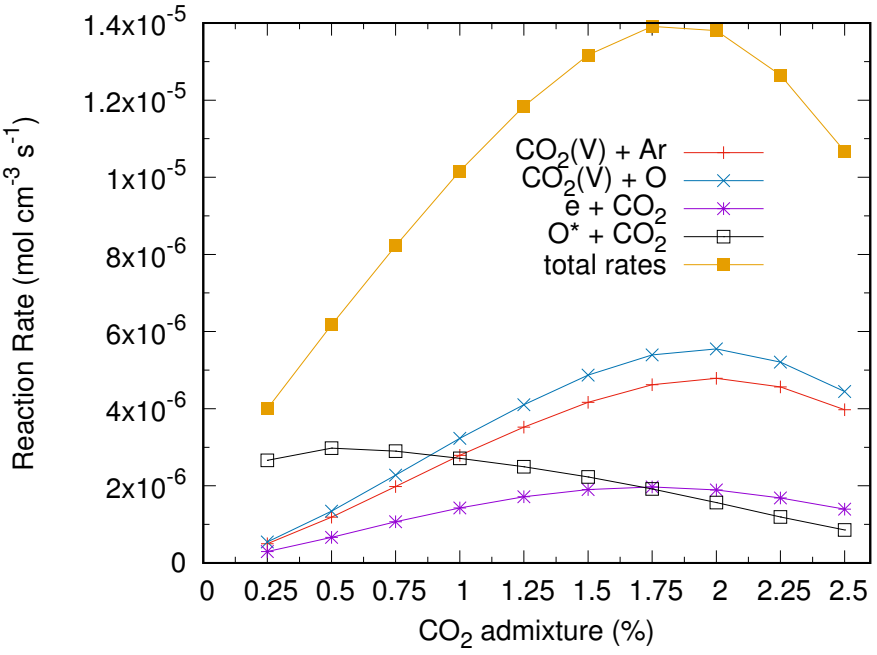

FIGURE 6.1: The main dissociation pathways of CO_2 in an argon carrier gas for admixtures ranging from 0.25 to 2.5% admixtures. The main dissociation pathways are shown to be collision with the carrier gas and oxygen atoms. These will only cause dissociation if the CO_2 molecule is very highly vibrationally excited, above 4.5 eV, which is caused by electron impact reactions. There is also a significant amount of dissociation caused by direct electron impact dissociation which requires electron energies higher than the dissociation energy.

CO_2 is dissociated by highly asymmetrically vibrationally excited CO_2 colliding with either the carrier gas or atomic oxygen produced from the initial dissociation of CO_2. There is also a significant amount of CO produced from direct electron impact dissociation and an excited oxygen atom reacting with CO_2. The recycling of the atomic oxygen to produce more CO is a particularly interesting result as it is using the chemical energy of the oxygen atom to dissociate more CO_2 instead of just recombining with other oxygen atoms and will improve the energy efficiency. Avoiding the reverse reaction of atomic oxygen and carbon monoxide combining is important in obtaining high yields and efficiencies [17]. The pathway analysis was undertaken over the course of the entire plasma to take account of the overall processes. Looking at just part of the plasma may tell a slightly different story as the atomic oxygen reaction cannot occur until other dissociation processes have taken effect. The full reactions and their rate coefficients are given in table 6.1, these are also the main pathways for helium and so the carrier gas is included as M rather than distinguishing each.

Dissociation Reactions	Reaction Rate (cm^3 s^{-1})	Number in Reactions List
$CO_2 + e^- \rightarrow CO + O(^1D) + e^-$	$\sigma(\epsilon)$	30 [107]
CO_2 (0 0 V) + M $\rightarrow$ CO + O + M	1.49×10^{-11} $T_g^{-0.58}$ $e^{\frac{65000}{T_g}}$	305 [108]
CO_2 (0 0 V) + O $\rightarrow$ CO + O_2	2.8×10^{-11} $e^{\frac{26500}{T_g}}$	307 [109]
CO_2 + O(1D) $\rightarrow$ CO + O_2	2.0×10^{-10}	256 [110]

TABLE 6.1: The reaction rates for the three most prominent dissociation reactions of CO_2. A full list of the reactions is available in Appendix B.

In order for the carrier gas to dissociate CO_2 the CO_2 molecules need to be very highly vibrationally excited, at least 4.5 eV, close to the dissociation energy of 5.5 eV. For vibrationally excited CO_2 molecules of 4.5 - 5.25 eV the chemical energy of the oxygen atom is enough to overcome the remaining energy required to cause dissociation. For the very highest asymmetrically vibrationally excited CO_2 molecule the gas temperature is sufficient energy to cause CO_2 to dissociate. The asymmetrically vibrationally excited CO_2 are also shown from the pathway analysis to be produced by electron impact reactions and not vibrational up-pumping. Most of the CO_2 is excited from the ground state due to the ground state being the most populated state of CO_2.

At atmospheric pressure the plasma is highly collisional and relaxation of the vibrational states of CO_2 is common. Although exact relaxation rates for asymmetrically vibrationally excited CO_2 are difficult to find argon is known to be an effective quencher [111] and since it has similar atomic mass as CO_2 it should also be an effective quencher of CO_2. Vibrational relaxation rates for argon in the model have been approximated using known rates for helium and the ratio of known relaxation times of CO_2 in argon and helium carrier gases [111–113]. The vibrational up-pumping rates of CO_2 are also approximated using published theories [61] for the reaction rates and this model shows that the relaxation reactions from the carrier gas have higher rates than the up-pumping reactions, at least for the high energy states leading to dissociation. Since the gas temperature is low for these plasmas only single quantum transitions are considered in the up-pumping reactions [65]. Although the reaction rates are thought to increase for the up-pumping reactions for more energetic states the density of these species drops dramatically and so the excited CO_2 stays energetic enough for dissociation are not populated by vibrational up-pumping. The carrier gas is also orders of magnitude higher in density than any of the excited states of CO_2 and remains constant throughout the plasma and is very effective at depopulating excited CO_2

states.

The reaction rates also show a similar trend to the CO density for the admixture variation. Most of the peaks in the reaction rates occur for the same CO_2 admixture, which corresponds to the peak seen in CO density. This again shows the effect the reduced electric field has on the dissociation of CO_2. Since the CO_2 states that are reactants in the two main channels are populated via electron impact reactions, these species and the electrons in the direct electron impact reaction depend heavily on the electron dynamics and so when the electron temperature becomes too low to populate these species despite the increased density the reaction rates begin to drop and less CO is produced. Seeing the peak in the rates in the expected places in the pathway analysis gives some confidence in the data as although the exact reaction rates may not be accurate the model and the reactions are showing the same trends in results that depend on the electron dynamics which are unique to each plasma. Except for the reaction of O(1D) metastable state with CO_2, which becomes less prominent as the CO_2 admixture is increased. The electron temperature decreases as CO_2 admixture is increased and therefore the production of O(1D) reduces and the reaction rate decreases also. For the smallest CO_2 admixtures the reaction with O(1D) is the single highest contributor to the production of CO. The density of the O(1D) state decreases with increasing CO_2 admixture and results in this reaction becoming less important for higher CO_2 admixtures. Heidner [110] reports that the reaction of O(1D) with CO_2 is an exothermic reaction producing the products CO and O_2, in the ground state, whereas the O(1S) state does not. Therefore this reaction does not require vibrationally excited CO_2 to occur and the effective production of the O(1D) state in the plasma, through electron impact excitation and direct electron impact dissociation of CO_2, causes this reaction to become prominent for low CO_2 admixtures. For higher CO_2 admixtures the production of O(1D) through electron impact excitation is significantly lowered and so the reaction becomes less important. However Heidner also reports that the reaction rate constant measured is two orders of magnitude higher than was previously reported and a difference of two orders of magnitude on this reaction rate coefficient would have substantial consequences on the reaction rate and reduce the importance of this reaction.

Figure 6.2 shows the main dissociation pathways of CO_2 on an energy level

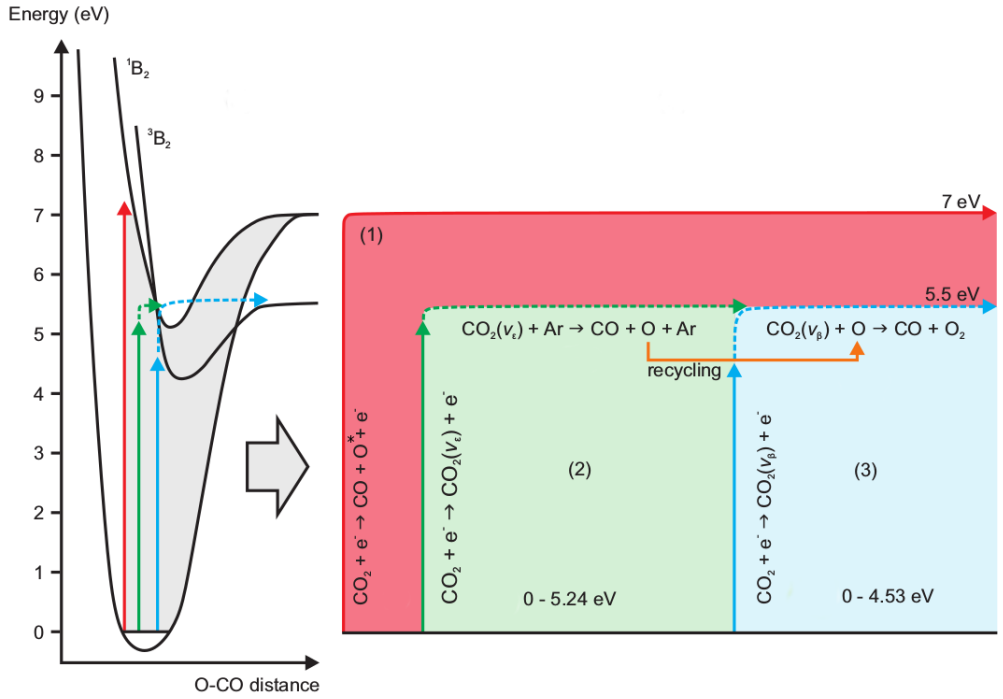

FIGURE 6.2: An energy level diagram of the main dissociation pathways of CO_2 in argon. The vast majority of the dissociation is done by highly excited vibrational states of CO_2 which are produced through direct electron impact dissociation. The figure also shows the energy levels required for carrier gas collision reactions and recycling of atomic oxygen reactions to occur.

diagram. It shows the energies of the vibrational states of CO_2 that cause the majority of the dissociation and the energy required for each pathway to become energetically feasible. Due to the gas temperature in the plasma being close to room temperature only single quantum transitions are considered in the vibrational-vibrational energy exchange reactions. This means that in order for the high energy states, that cause dissociation, to be populated through vibrational up-pumping of CO_2 there must be a collision with a vibrational state just one energy level lower [65]. The density of the high energy states drops considerably from the lower energy states with vibrational energies close to that of the mean electron energy or lower and therefore the vibrational up-pumping is also much lower for high energy states. As such whilst there is some vibrational up-pumping for lower energy states the densities of the high energy states is too low for it to have a significant impact on the production of CO_2 levels that cause dissociation. Single quantum transitions between dissociative vibrational levels is also not common due to the reaction rates of dissociation being higher than those for up-pumping in the pathway analysis, largely because the densities of argon and atomic oxygen are orders of magnitude higher than high vibrational energies of CO_2.

6.1.2 Dissociation Pathways of CO_2 in Helium

Figure 6.3 shows the main dissociation pathways in helium and how they are very similar to the argon pathways. This is because the rate coefficients used for the reaction processes are the same for each carrier gas. In the case of direct electron impact dissociation and the recycling of atomic oxygen the same reaction cross sections should be used as neither of the reactants are the carrier gas, but for the dissociation of CO_2 by collision with the carrier gas little data is available for a helium carrier gas. These reaction rates are usually calculated in shock experiments with a noble gas used as a background gas [108]. These experiments have been done with a number of different noble gas backgrounds but not with helium.

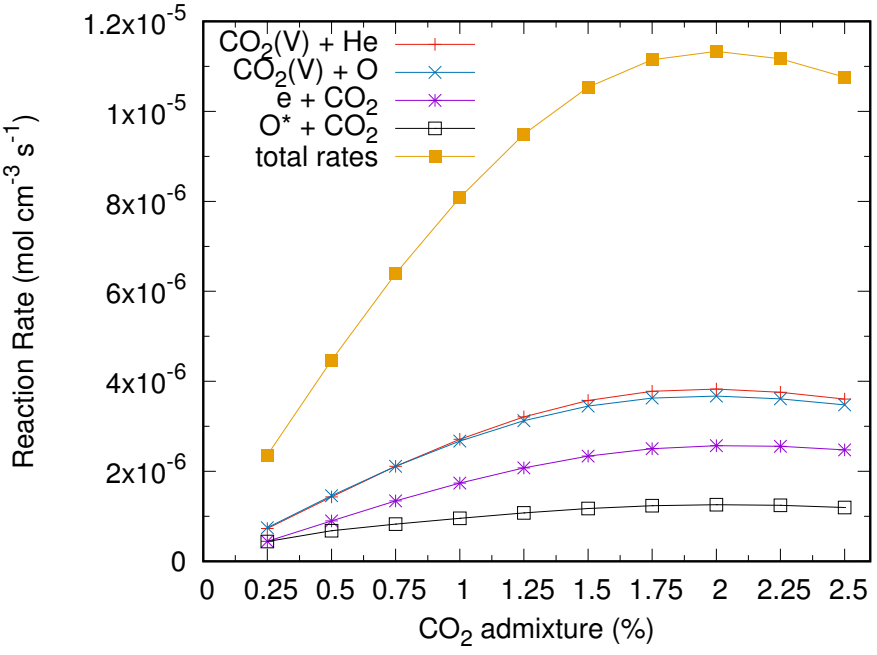

FIGURE 6.3: The main dissociation pathways of CO_2 in an helium carrier gas for admixtures ranging from 0.25 to 2.5% admixtures. The main dissociation pathways are shown to be collision with the carrier gas and oxygen atoms. These will only cause dissociation if the CO_2 molecule is very highly vibrationally excited, above 4.5 eV, which is caused by electron impact reactions. There is also a significant amount of dissociation caused by direct electron impact dissociation which requires electron energies higher than the dissociation energy.

For both helium and argon the main dissociation channels are through a collision with the carrier gas followed by recycling of the oxygen atom produced. The curve of the helium rates also follows the same trend as the carbon monoxide density for an admixture variation. The peak in the rates in the case of helium occurs

at the same point as the peak in carbon monoxide density for a CO_2 admixture of 2.0%. The rate of direct electron impact reaction is higher in helium than in argon because of the higher energy tail of the helium electron energy distribution function. There is a higher rate for the dissociation of CO_2 for the reactions involving highly vibrationally excited CO_2. Due to the EEDF in argon favouring electrons with energies in this region. The biggest difference in the rates comes from the reaction of O(1D) with CO_2, which is far more prominent in helium. The higher electron temperatures observed in argon favour the production of O(1D) and cause higher reaction rates.

The reaction rate coefficients for the dissociation through collisions with the carrier gas, do not vary with different carrier gases since the dissociation is caused only by collisions and not a chemical reaction. The reaction rate coefficient may vary depending on the mass of the background gas and may be different for helium and argon. Since the data is not available for the different carrier gases it is not possible to distinguish a rate between the two and the same is used for each [108]. This is likely to overestimate the rate for dissociation in collision with helium and explains why the yield is consistently higher in the helium simulations compared with the experiment. Lowering the rate for collision with the carrier gas would also reduce the rate of atomic oxygen recycling as the carrier gas reaction produces the atomic oxygen for the recycling reaction.

The reaction rates for the main dissociation pathways were carefully chosen. Since the activation energy of the reactions is lowered with the vibrational energy of the CO_2 state it is important to choose a reaction rate with an appropriate activation energy. The reaction rate coefficients are lowered according to equation 3.1 [114] by the vibrational energy of the CO_2 state. The values for the coefficient α are set according to the Fridman-Macheret α model [61]. For the dissociation reaction through collisions with the carrier gas a value of $\alpha = 1$ was used so that there is no activation energy for the highest CO_2 asymmetric vibrational state due to its energy been only 300 K below the dissociation limit. Therefore it is important to choose a reaction rate with an activation energy equal to that of the dissociation limit of CO_2, as this is the energy barrier to overcome. Some reaction rates available in the literature can have a lower activation energy than this, most likely because it was used a fitting variable to experimental data and not using the theoretical value, which would cause more CO_2 vibrational levels to have sufficient energy to dissociate and increase the yield of CO. The activation energy in the

reaction rate is therefore an important parameter to choose accurately as it will have a large affect on the conversion of CO_2 and the pathway analysis results.

For the recycling of atomic oxygen reaction a value of $\alpha = 0.5$ was used as it is a thermoneutral reaction, in accordance with other studies [61, 64, 65]. For exothermic reactions with next to no activation energy a value of $\alpha = 0$ was used. If reaction rates with inaccurate activation energies are used this can have a large effect on the reaction rate coefficient for different vibrational CO_2 states. The value of α essentially determines which CO_2 states will have sufficient energy to dissociate and so using reactions rates with low activation energies will cause lower energy CO_2 vibrational states to dissociate and increase the yield. Due to the good agreement between the model and the experiment the reaction rates chosen for this work appear to accurately reflect the plasma chemistry, however there are always errors in these reaction rates and also in the values of α used and this has a substantial affect on the model and the pathway analysis. The reaction of CO_2 and O used [109] was determined from thermal kinetics and was in equilibrium with the reverse reaction. The plasma is not hot enough for this reaction to be in equilibrium with the reverse reaction and so becomes a large source of CO. It stands to reason that if completely different reaction rates from the literature were chosen the pathway analysis results would also be completely different and therefore it is vitally important to validate the model against as many experimental parameters as possible to be confident in the findings.

For the carrier gas collision reaction there is no chemical energy involved and so the activation energy of the reaction should be the bond energy of the CO_2 molecule. As the reaction rates are written in arrheinus format the activation energy is a simple variable to determine if a reaction rate is appropriate. As the reaction rates are usually determined by fitting to experimental data it is important to find a reaction rate that has the activation energy equal to bond energy and not one that has just been used as a fitting parameter. By using a rate with an activation energy which is the same as the bond energy, only the highest asymmetric vibrational level of CO_2 will have almost no energy barrier to overcome. Using a reaction rate with a poorly chosen activation energy could lead to many vibrationally excited CO_2 levels dissociating just from collisions even though the gas temperature is calculated to be less than 350 K in the simulations.

For the recycling of atomic oxygen reaction it is important to choose a reaction rate that represents the plasma. Many of the reactions rates for this reaction are

determined in thermodynamic equilibrium where the forward reaction is in equilibrium with the backwards reaction where carbon monoxide and oxygen would react to form carbon dioxide and atomic oxygen. This is not the case in these plasmas as the gas temperature is not hot enough for the backwards reaction to occur and the forward reaction will only occur with sufficiently high vibrational energy in the CO molecule instead of thermal energy. It is important to understand that although the reaction rate used is from a thermodynamic equilibrium scenario this plasma [109], at least, is not in thermodynamic equilibrium and is not in equilibrium with the reverse reaction due to vibrational excitation. The activation energy of the reaction is very important as it will determine which vibrational states have sufficient energy to dissociate. Since the reaction rates have an exponential dependence on the activation energy using an activation energy that is too high or too low will affect which vibrational level can dissociate and will have a dramatic effect on the achieved yields as the pathway analysis shows that the asymmetric states of CO_2 play a very important role in the production of CO.

6.1.3 Determining the cross section for direct electron impact dissociation

The model has been using the 7 eV electronic excitation of CO_2, from the Phelps database [115], as an approximation for direct electron impact dissociation. This like the other two prominent dissociation cross sections has been carefully chosen to try and give the most accurate results. Even though direct electron impact dissociation is important in many types of plasmas, particularly those with high reduced electric fields, such as dielectric barrier discharges [116], the dissociation cross-section is not well understood. Many different databases provide data for the electronic excitation of CO_2, however the shape and the magnitude of the cross sections with respect to the electron energy vary considerably as reported in [97] and is shown in Figure 6.4.

Since the electronic excitation of CO_2 requires more energetic electrons than vibrational excitation, it is far more likely to occur in plasma with high reduced electric fields so the measurements of the 7 eV electronic state are conducted for E/N values higher than are observed in the plasmas studied in this thesis. Figure 6.4 shows that there is a large difference in the magnitude of the rate

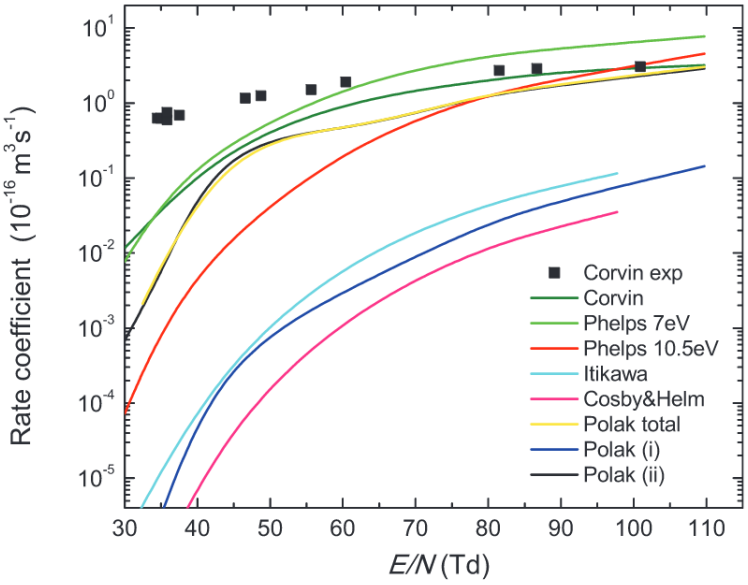

FIGURE 6.4: Rate coefficients for the direct electron impact dissociation of CO_2 calculated from electron excitation cross-sections with respect to the reduced electric field and a comparison to the experimental measurements of Corvin [117]. The 7 eV electronic excitation of CO_2 for the Phelps database reasonably conforms with the experimental dissociation rate coefficient and has the best agreement for the lower reduced electric fields. Figure taken from [97].

coefficients calculated from the different cross-sections and many of the cross-sections do not conform to the experimental value for the rate coefficient. The 7 eV electronic excitation of CO_2 for the Phelps database reasonably conforms to with the experimental dissociation cross-section and has the best agreement for the lower reduced electric fields and so has been used as an approximation for direct electron impact dissociation in the model. It is also clear that the 10.5 eV electronic excitation cross-section from the Phelps database does not accurately provide a rate coefficient for the direct electron impact dissociation and can be assumed not to contribute.

6.2 Pathways for the production and destruction of atomic oxygen

6.2.1 Production Pathways of Atomic Oxygen

Since the reaction of atomic oxygen with vibrationally excited CO_2 is seen to be very important in the dissociation process in these plasmas as well as for an

efficient dissociation process, it is important to determine the main production pathways of atomic oxygen.

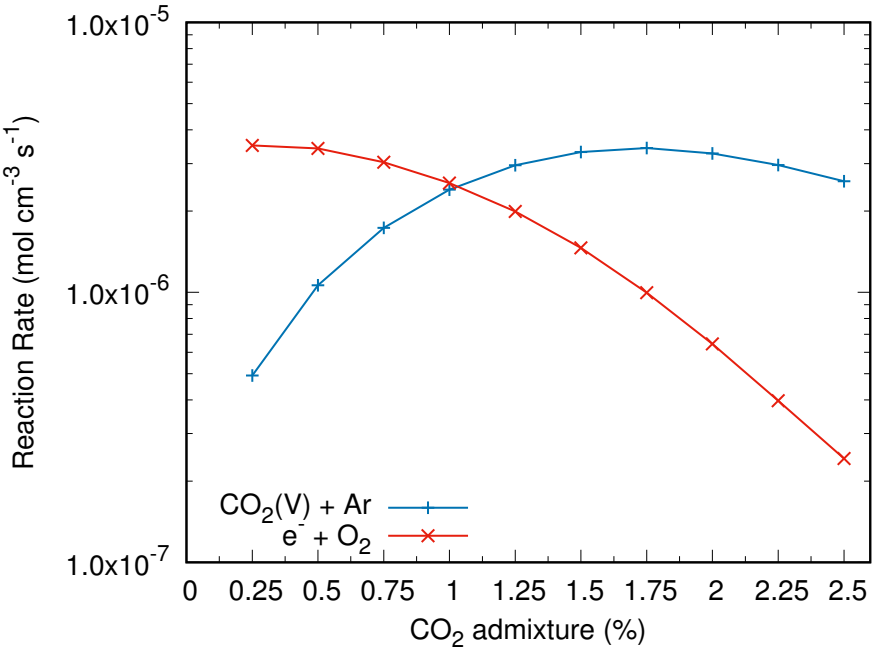

FIGURE 6.5: The two main production pathways of atomic oxygen in an argon plasma with respect to CO_2 admixture. The vast majority of atomic oxygen is produced through either the dissociation of vibrationally excited CO_2 through collisions with the carrier gas and or direct electron impact dissociation of CO_2. For plasmas with low CO_2 admixtures the electron temperature is higher and direct electron dissociation is more likely.

Figure 6.5 shows the two main production pathways of ground state atomic oxygen, which are through the dissociation of CO_2 from the collision with the carrier gas and direct electron impact dissociation of O_2. Direct electron impact dissociation of CO_2 produces O(1D) and the quenching of this state is not one of the main sources of ground state atomic oxygen. The production of atomic oxygen through direct electron impact dissociation is the main source of atomic oxygen in plasmas with small CO_2 admixtures. This is due to the higher electron temperatures in the small CO_2 admixture plasmas. The bond energy of O_2 is slightly lower than CO_2 at only 4.77 eV and so many electrons are energetic enough to be able to dissociate O_2. The atomic oxygen produced through direct electron impact dissociation of CO_2 is in an excited state and so is not included as a pathway in this analysis but the relaxation of the excited state is and that relaxation reaction was found not to be prominent. This is in a large part due to the reaction of the excited 1D state of atomic oxygen reacting with CO_2 [110]

which is found to be the forth highest contribution for the production of carbon monoxide. However the electronic energy in the 1D state of atomic oxygen is not energetic enough to account for the dissociation energy of CO_2 and the reaction rate was determined at low pressure. There is some question, therefore, of how valid the reaction rate for this plasma system is. The full reactions and their rate coefficients are included in table 6.2.

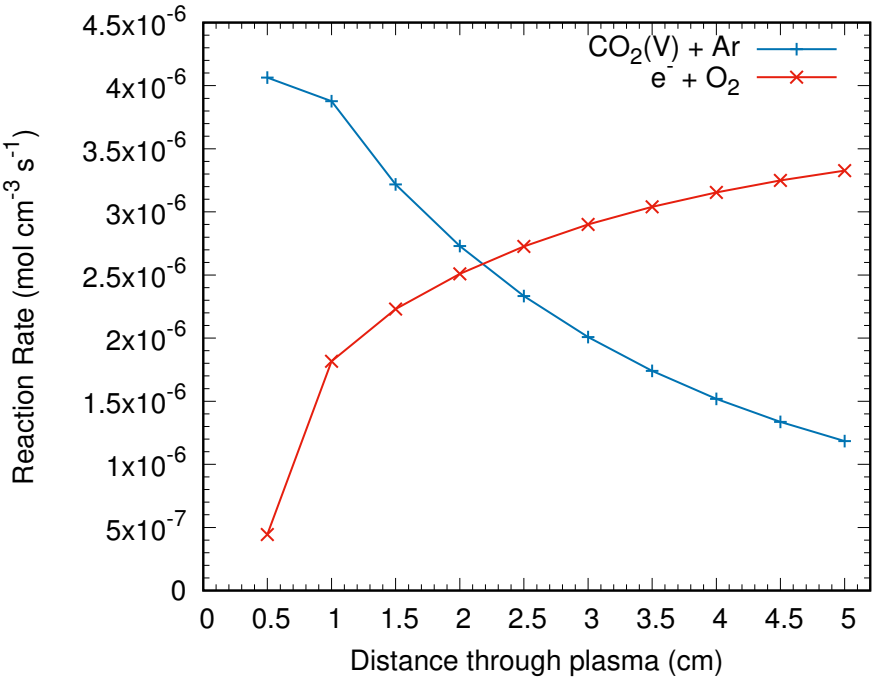

FIGURE 6.6: The two main production pathways of atomic oxygen as a function of distance in the plasma for the 1.5% CO_2 admixture in an argon plasma. Each data point is analysed over the previous 0.5 cm of the plasma and is not an accumulation of the rate throughout the plasma. In the early part of the plasma most of the production of atomic oxygen comes from the dissociation of vibrationally excited CO_2 through collisions with the carrier gas. As the O_2 density increases the CO_2 density decreases the production of atomic oxygen through direct electron impact dissociation becomes much more prominent.

Since the nature of the plasma changes considerably throughout the plasma as the contents of the admixture considering the production pathways as a function of distance in the plasma will provide insights into how to optimise the plasma. Figure 6.6 shows the two main production pathways of atomic oxygen throughout the 1.5% CO_2 admixture argon plasma. The pathway analysis was performed in intervals of 0.5 cm so that each data point shows the rate from the last point and not a cumulative rate to more clearly show how the plasma chemistry changes throughout the plasma. In the early part of the plasma most of the atomic oxygen is produced through the dissociation of CO_2 due to the density of CO_2 being

much higher than the density of O_2. The pathway analysis of the production of atomic oxygen shows that most of the atomic oxygen produced comes from the dissociation of CO_2 and not the dissociation of CO. CO has a much higher bond energy than CO_2 and very few electrons in the plasma are energetic enough to dissociate CO.

The production of atomic oxygen through the dissociation of molecular oxygen is an unavoidable consequence of the production of molecular oxygen from the dissociation process. The process does not directly affect the yield of carbon monoxide since the bond energy of molecular oxygen is of a similar magnitude to the energy of the vibrational states of CO_2 that lead to dissociation and therefore electrons that could potentially cause more CO_2 to dissociate are being used to dissociate O_2 to no effect. This has an impact on the energy efficiency of the process but is a consequence of having high yields of CO in the plasma. Since the recycling of atomic oxygen is very important to the dissociation of CO_2 the destruction pathways of atomic oxygen are more important than production to trying to optimise the plasma to enhance the yield and energy efficiency.

Dissociation Reactions	Reaction Rate ($cm^3\ s^{-1}$)	Number in Reaction List
$O_2 + e^- \rightarrow O + O + e^-$	$\sigma(\epsilon)$	44 [115]
CO_2 (0 0 V) + M $\rightarrow$ CO + O + M	$1.49 \times 10^{-11}\ T^{-0.58}\ e^{\frac{65000}{T}}$	305 [108]

TABLE 6.2: The reaction rates for the most prominent production reactions of O. A full list of the reactions is available in Appendix B.

6.2.2 Destruction Pathways of Atomic Oxygen

Figure 6.7 shows the four main destruction pathways of atomic oxygen in an argon plasma with a 1.5% CO_2 admixture. The pathway analysis was performed in intervals of 0.5 cm so that each data point shows the rate from the last point, as in the previous figure. Since the recycling of atomic oxygen is important to both the production of carbon monoxide and the energy efficiency of the dissociation of CO_2 it is useful to see how atomic oxygen is consumed throughout the plasma to try and tailor the plasma to favour carbon monoxide production. The full reactions and their rate coefficients are given in table 6.3

At the inlet of the plasma most of the atomic oxygen is lost to the desirable reaction where atomic oxygen reacts with excited CO_2 to produce carbon monoxide

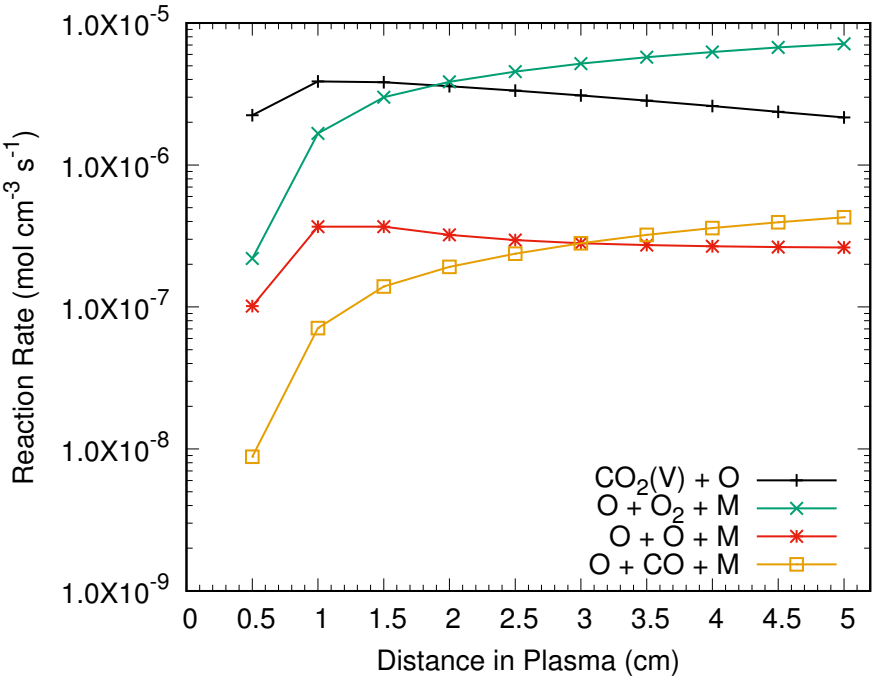

FIGURE 6.7: The main destruction pathways of atomic oxygen in an argon plasma with a 1.5% CO_2 admixture. Each data point is analysed over the previous 0.5 cm of the plasma and is not an accumulation of the rate throughout the plasma. Of the four main destruction pathways of atomic oxygen only one pathway is desirable, the reaction with vibrationally excited CO_2 molecules. Very early on in the plasma this is the main destruction pathway due to the low densities of other species. However as the plasma chemistry develops more atomic oxygen is lost to the production of ozone.

and molecular oxygen. This is due to the small densities of the reactants in the other pathways and atomic oxygen being the by product of dissociating CO_2 into CO. This continues as one of the most prominent destruction pathways throughout the plasma. If the cumulative rates are considered instead of small sections of the plasma this desirable reaction is the most prominent in the plasma due to the very low rates of the other channels in the early part of the plasma. This means that the recycling of atomic oxygen to produce more carbon monoxide is naturally the most prominent reaction even for a plasma where there is a significant amount of dissociation of CO_2 with a high density of carbon monoxide and molecular oxygen at the end of the plasma.

However after two centimetres the production of ozone starts to become the most prominent destruction pathway of atomic oxygen. This is the case because the reaction of atomic oxygen with carbon dioxide produces molecular oxygen and so as the neutral gas continues to move through the plasma the density of molecular oxygen begins to increase and the three body collision of atomic and molecular

oxygen with the background gas becomes more likely as the production of ozone starts to increase. Pathway analysis of the production and destruction pathways of ozone show that this reaction is almost the only source of ozone and most of the destruction of ozone comes from electron impact dissociation [118, 119]. Since the production of ozone is from neutral gas species prominent in the plasma it is difficult to prevent the formation of ozone in atmospheric pressure plasmas and it is also quite a reactive species that could pose problems for the utilisation of the carbon monoxide produced.

The three body recombination of two oxygen atoms into molecular oxygen [83, 120] is not as prominent as the three body recombination of atomic oxygen and molecular oxygen [121] in part due to the reaction rate coefficients but also because of the density of the reactants. In the early plasma the reaction rates of these two three body reactions are very close to each other. As the molecular oxygen density increases, due to both reactions producing molecular oxygen and it is inherently more stable than atomic oxygen so the species lasts longer, and the three body recombination reaction into molecular oxygen falls in prominence in favour of ozone production. Finally the three body recombination to reform CO_2 is the least prominent destruction pathway of atomic oxygen. This is again favourable for the efficient production of carbon monoxide as it means that again most of the atomic oxygen produced is used to create more carbon monoxide and does not have the reverse reaction to reproduce carbon dioxide. This reverse reaction is strongly endothermic and in a thermal plasma the reverse reaction is very prominent and reduces the yield and energy efficiency of the process.

Only the results for one particular argon case are shown here due to the all of the reactants of the main pathways being neutral gas species and independent of the carrier gas. Consequently the rate coefficients of the reactions will be the same between the two plasmas and for different admixtures. The only differences expected will be due to the different species densities of the reactants between the different variables and the main pathways will not change only the value of their rates.

Dissociation Reactions	Reaction Rate ($cm^{3(6)}$ s^{-1})	Number in Reaction List
$CO + O + M \rightarrow CO_2 + M$	1.70×10^{-33} $e^{\frac{1510}{T}}$	265 [109]
$O + O_2 + M \rightarrow O_3 + M$	6.90×10^{-34}	262 [121]
CO_2 (0 0 V) $+ O \rightarrow CO + O_2$	2.8×10^{-11} $e^{\frac{26500}{T}}$	307 [109]
$O + O + M \rightarrow O_2 + M$	5.21×10^{-35} $e^{\frac{900}{T}}$	260 [109]

TABLE 6.3: The reaction rates for the most prominent destruction reactions of O. A full list of the reactions is available in Appendix B.

6.3 Pathways for the Destruction of Carbon Monoxide

Even though these plasmas have been shown to be able to produce very high yields of carbon monoxide in the far effluent it is important to consider the destruction pathways of carbon monoxide. Figure 6.8 shows the two main destruction pathways of carbon dioxide which are: the three body recombination of carbon monoxide with atomic oxygen and direct electron impact dissociation of carbon monoxide, in an argon plasma with a 1.5% CO_2 admixture. Carbon monoxide has a much higher bond energy than carbon dioxide, 9.77 eV to 5.5 eV for carbon dioxide, and as a consequence far more energetic electrons are required to directly dissociate carbon monoxide. The complete dissociation of CO_2 to produce carbon is shown to not be very prominent in the model and carbon monoxide is very unlikely to further dissociate, this conforms with the experimental data where no carbon deposits are visually observed in the plasma or effluent and the selectivity of carbon monoxide is at a constant 100 % within error. The full reactions and their rate coefficients are given in table 6.4.

The reverse reaction of carbon monoxide and atomic oxygen to produce carbon dioxide [109] is the highest rate for carbon monoxide losses and is shown to be almost an order of magnitude lower in reaction rate compared to the forward reaction and therefore far more carbon monoxide is produced than lost in the plasma. The destruction pathways of atomic oxygen also showed that the reverse reaction with carbon monoxide is not the most likely reaction to occur for atomic oxygen. Therefore the reverse reaction of carbon monoxide and atomic oxygen is of little importance in the plasma and looking at the reaction rates for the production of ozone compared to the reverse reaction. In the effluent it is far more likely that the remaining atomic oxygen will produce ozone instead of CO_2. This is largely due to the gas temperature of the plasma. Since the gas temperature in these

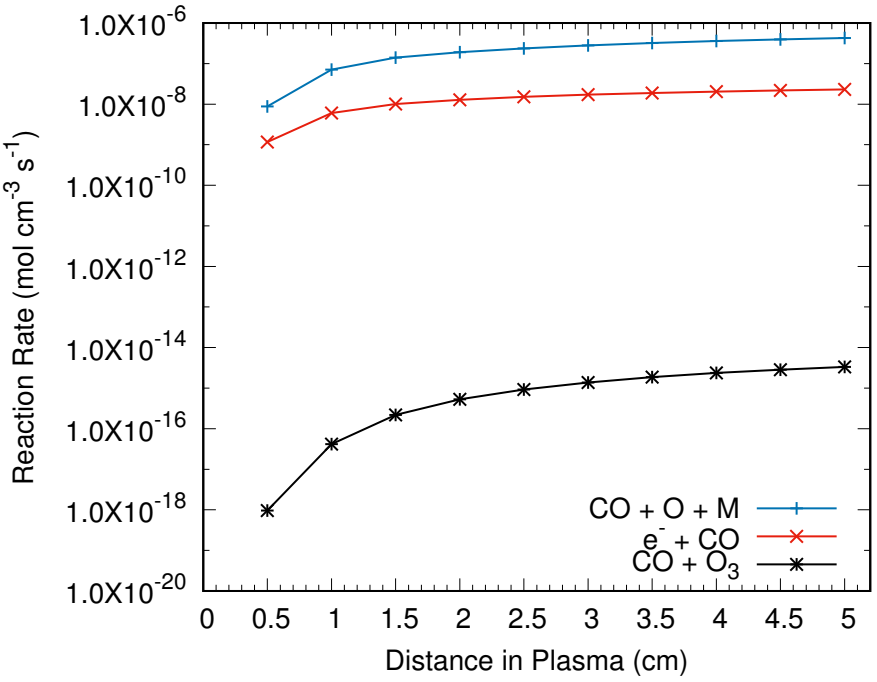

FIGURE 6.8: The destruction pathways of carbon monoxide in an argon plasma with a 1.5% CO_2 admixture. The two main destruction pathways of carbon monoxide are the three body recombination of carbon monoxide and atomic oxygen and direct electron impact dissociation of carbon monoxide. The carbon monoxide destruction rates are at least an order of magnitude lower than the production of carbon monoxide showing that most of the carbon monoxide produced is not lost to further reactions.

plasma is very low, reaching at most 325 K in the simulations, the reverse reaction is not very likely as it is endothermic.

Finally the reaction of carbon monoxide and ozone is included as it may be expected that the reactive species ozone may strongly react with carbon monoxide. However this reaction has been shown to only occur strongly under the presence of a catalyst [105, 122]. Therefore whilst the production of ozone is undesired due to its consuming atomic oxygen and thus preventing the atomic oxygen from being recycled it does not pose any issue in the plasma or the effluent in terms of reducing the yield of carbon monoxide and can be easily removed from the effluent gas using a catalytic ozone scrubber that removes the ozone without having any effect on the CO or CO_2 densities. When a catalytic scrubber was included in the gas line to the FTIR the ozone bands in the spectra were reduced to undetectable levels whilst the yield of CO remained constant.

The pathway analysis has shown that the dissociation of CO_2 in these plasmas is largely via the desired routes of vibrational excitation and the low energy

Dissociation Reactions	Reaction Rate ($cm^{3(6)}$ s^{-1})	Number in Reaction List
$CO + O + M \rightarrow CO_2 + M$	1.70×10^{-33} $e^{\frac{1510}{T}}$	265 [109]
$CO + e^- \rightarrow C + O + e^-$	$\sigma(\epsilon)$	35 [123]
$CO + O_3 \rightarrow CO_2 + O_2$	4.00×10^{-25}	264 [105]

TABLE 6.4: The reaction rates for the most prominent destruction reactions of CO. A full list of the reactions is available in Appendix B.

efficiencies are caused by the high specific energy inputs. However the pathway analysis has not clearly shown why such differences in the yield of CO are observed for the two different carrier gases. In order to determine why these differences are observed it is necessary to look into the energy loss fractions of the two gas compositions to see where the electron energy is being deposited.

6.4 Energy Loss Fractions

In order to achieve dissociation of CO_2 in a plasma the electron energy needs to be distributed into channels that will lead to dissociation. In order to better tailor the experimental set-up to increase both the yield and the energy efficiency of CO a greater understanding of the underlying processes is required. Electron energy loss fractions are calculated when solving the Boltzmann equation to gain the EEDF of the plasma and they can also be used to determine where the greatest electron losses are and how the set-up can be tailored to ensure the electron energy is deposited in channels that will cause dissociation. This information can then be used when trying to tailor the EEDF by using harmonics in the driving frequency [124].

Since the global model calculates the EEDF and energy loss fractions for a range of differently reduced electric field values, and interpolates between these values to obtain the EEDF and loss fractions for the exact electron temperature of the point in the simulation, it is difficult to obtain a highly resolved confirmation of the loss fraction across a large range of reduced electric fields. Bolsig+ [24] however has far more flexibility and can produced energy loss fractions for a large range of reduced electric fields with a high resolution using exactly the same cross-sections as in the global model. The outputs of Bolsig+ also provide an electron temperature for each value of the reduced electric field this means that it is then

much easier to compare single data points in the Bolsig+ simulation to the global model simulations.

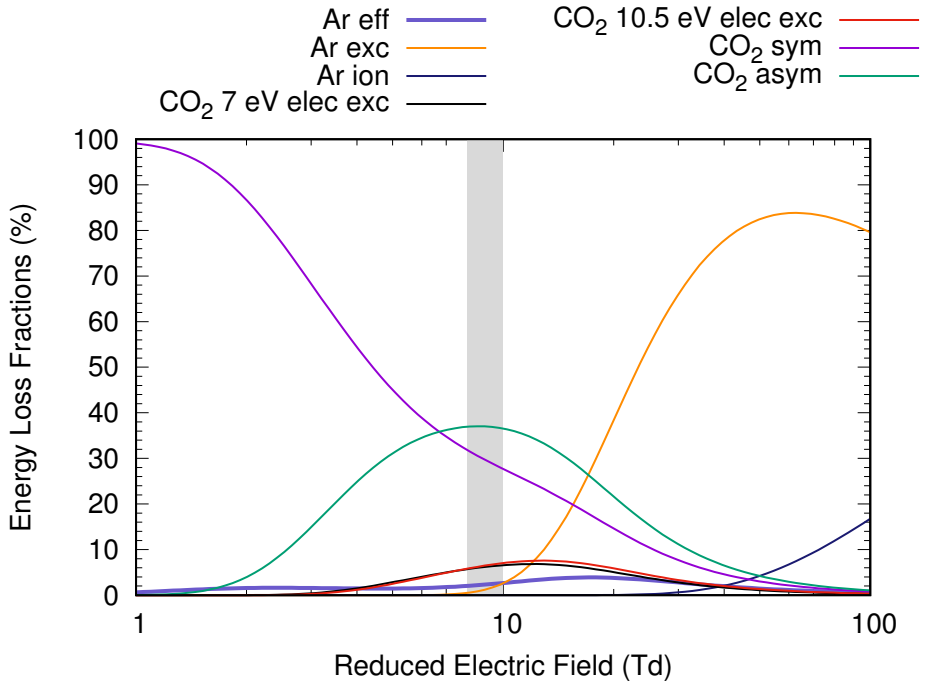

FIGURE 6.9: The energy loss fractions for the argon electron impact reactions, the electronic excitation of CO_2, as well as the symmetric vibrational excitation and asymmetric vibrational excitations above 4.5 eV, loss channels in an argon plasma with 1.5% CO_2 as an admixture as a function of the reduced electric field. The energy loss fractions were calculated using Bolsig+ using the same cross sections as in the global model.

Figure 6.9 shows the energy loss fractions for a 1.5% CO_2 admixture in argon. There are many processes included when solving the Boltzmann solver and only a select few are shown for ease of understanding. The symmetric stretches of CO_2 are included in a single line as a sum of the individual processes, and only very high energy asymmetric stretches of over 4.5 eV are included. The loss fractions for processes such as CO_2 ionisation are not included due to having very low values in the region of interest. The region of interest, the shaded area, is the region where the electron temperature corresponds to the simulations and is therefore the area where the electron energy losses are relevant. The region of interest covers a substantial range of E/N values due to the interpolation of the model between different E/N values and the changing electron temperature in the model as the contents of the admixture changes due to dissociation of CO_2.

The first thing of note in the energy loss fractions in Figure 6.9 is that the electron energy lost in the effective momentum collision with the carrier gas is less

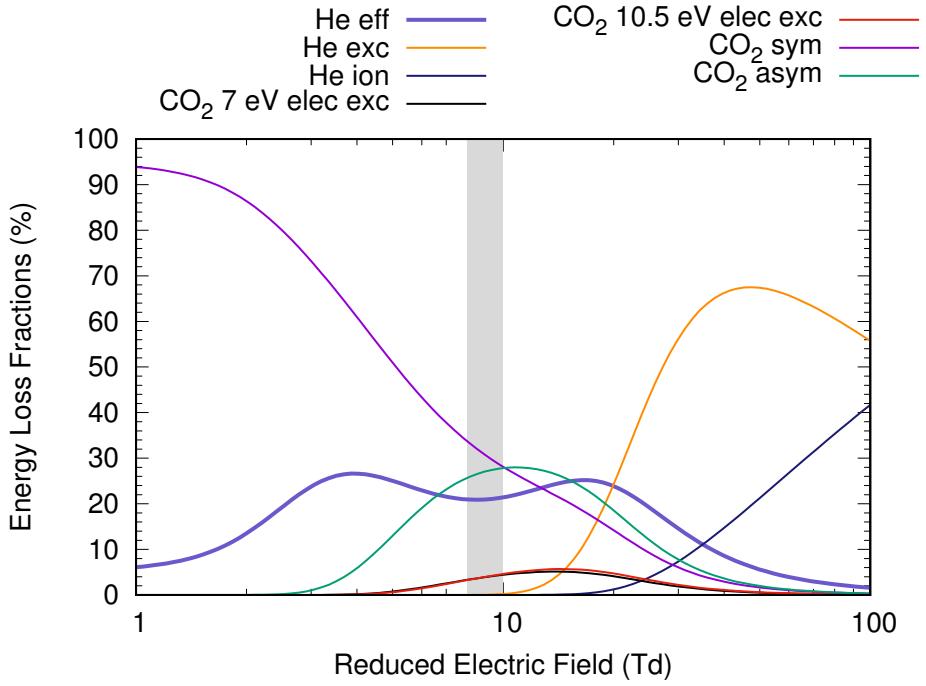

FIGURE 6.10: The energy loss fractions for the helium electron impact reactions, the electronic excitation of CO_2, as well as the symmetric vibrational excitation and asymmetric vibrational excitations above 4.5 eV, loss channels in a helium plasma with 1.5% CO_2 as an admixture as a function of the reduced electric field. The energy loss fractions were calculated using Bolsig+ using the same cross sections as in the global model.

than 5% of the total energy losses. This is stark contrast to Figure 6.10 where the effective momentum transfer accounts for nearly 30% of the electron energy losses. This means that in an argon plasma the carrier gas is essentially 'invisible' to the electrons and they are only in effect colliding with the CO_2 molecules. Whilst in the helium plasma a considerable amount of the electron energy is lost in collisions with the carrier gas which wastes energy. This is one of the main causes of the large difference in yields for the two carrier gases and is due to the Ramsauer minimum.

6.4.1 Ramsauer Minimum

Figure 6.11 shows the cross sections for the effective momentum transfer for both argon [125] and helium [126] for a range of different electron energies. There is a clear dip in the argon cross section for relatively low electron energies. Considering the mean electron energies in these plasma is on the order of 2-3 eV this dip in the cross section will have an effect on the calculated rates. Since the cross section for

the collision is lower in argon than in helium and each carrier gas has the same number density in its respective plasma, the reaction rate for argon, and therefore the loss fraction, will be lower and more of the electrons will collide inelastically with CO_2 molecules.

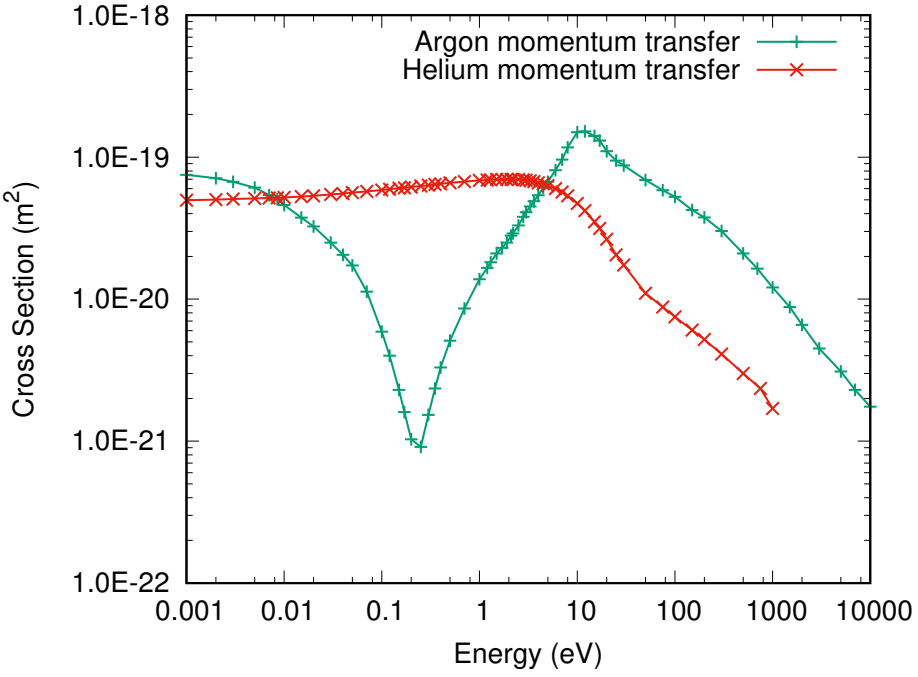

FIGURE 6.11: Effective momentum cross sections for argon [125] and helium [126], demonstrating the Ramsauer minimum.

The reason for this dip in the cross section is due to quantum mechanical effects of the electrons interaction with the noble gas atoms and cannot be explained by classical physics [127]. In a classical scenario the elastic scattering cross section is expected to decrease with increasing electron energy, which figure 6.11 shows for very high electron energies. However the behaviour of the low energy electrons, those with energies comparable to the electron energies in the plasmas studied, do not behave as expected. By considering the wave properties of electrons it is possible to show that reflected electrons destructively interfere with the incoming electrons resulting in a net transmission of electrons through the atom [128]. In order for this to occur the potential barrier created by the atom must be equal to some integer value of half the electron wavelength. This can be calculated by solving a simple one dimensional well using the time independent Schrödinger model. Helium does not have a high enough potential barrier for this effect to occur and so elastic scattering is much more likely for low energy electrons.

6.5 Desirable Electron Energy Loss Channels

The energy loss fractions can also provide an insight into how CO_2 is dissociated. In considering Figure 6.12 and 6.13 for the range of reduced electric fields that correspond to the simulations there are two loss channels shown in bold. These channels are the asymmetric stretches of CO_2 with a vibrational energy over 4.5 eV and the 7 eV electronic excitation of CO_2, which is used as an approximation for a direct electron impact dissociation cross section.

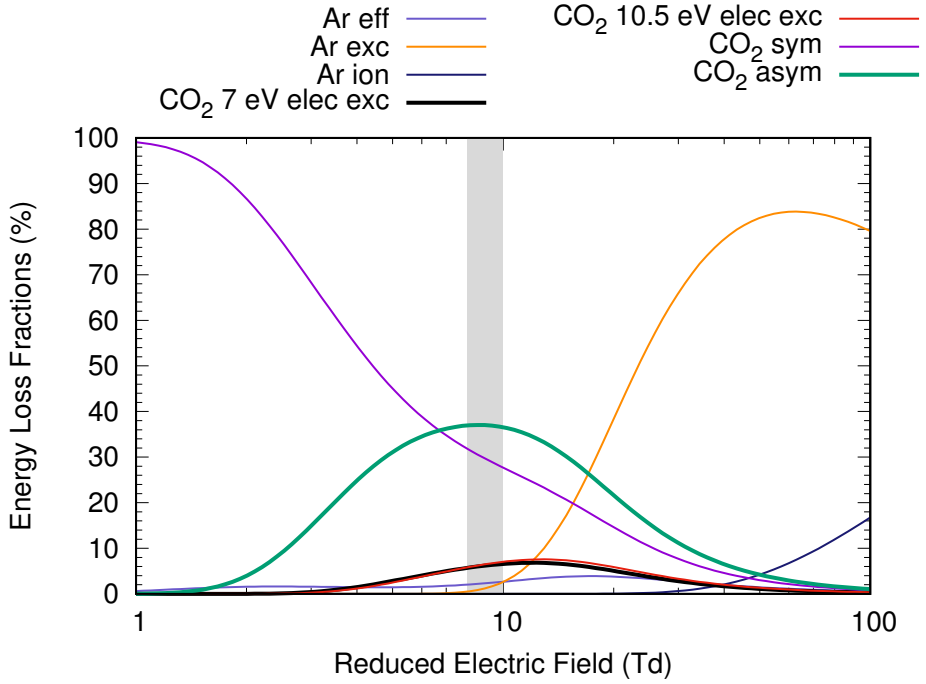

FIGURE 6.12: The energy loss fractions for the argon electron impact reactions, the electronic excitation of CO_2, as well as the symmetric vibrational excitation and asymmetric vibrational excitations above 4.5 eV, loss channels in an argon plasma with 1.5% CO_2 as a admixture as a function of the reduced electric field. The vibrational excitations above 4.5 eV are the ones found to cause dissociation and so only the loss fractions to dissociative asymmetric stretches are shown. The energy loss fractions were calculated using Bolsig+ using the same cross sections as in the global model. The desirable electron energy loss fractions are shown in bold in this figure.

The loss fractions in bold are the ones shown by the pathway analysis to be the cause of the majority of the production of carbon monoxide. For the reduced electric fields that correspond to the simulations, the highlighted region, a significant amount of the electron energy is now going into the desired loss channels in the case of an argon plasma. In the case of argon over 50% of the electron energy losses are into pathways that the pathway analysis showed would lead to

dissociation. This means that the electron energy is been quite efficiently deposited into the CO_2 and the reason for the low energy efficiency of the dissociation is due to the very low partial pressure of CO_2. Although the plasma is ignited at atmospheric pressure due to only using admixtures of up to a few percent the partial pressure of CO_2 is only a few percent of atmospheric pressure. As a result the energy input per molecule of CO_2 is large, much larger than the enthalpy of the dissociation reaction, and although the electron energy is being deposited in the desirable channels the number of CO_2 molecules is too low to achieve high energy efficiencies seen, for instance, in microwave plasmas [36, 56].

However increasing the admixture of CO_2 will affect the mean electron energy of the plasma and therefore the reduced electric field. The effect that increasing the CO_2 admixture has on the mean electron energy is to reduce it as there are many more degrees of freedom in CO_2 than argon. Therefore electrons are more likely to collide with CO_2 and more likely to collide inelastically with CO_2. Lower mean electron energies mean lower reduced electric fields and therefore it has the effect of moving the region of interest to the left on figures 6.12 and 6.13. This means that less electron energy is going into the desired channels for dissociation and the yield of CO will decrease.

Diluting the CO_2 in a carrier gas such as argon or helium increases the mean electron energy compared to a pure CO_2 atmospheric pressure plasma and enables a plasma to be ignited and sustained at atmospheric pressure using a radio frequency driving frequency. It is only due to the dilution of CO_2 in the carrier gas that the reduced electric field is such that most of the electron energy is going into desired channels. Consequentially whilst the low partial pressure of CO_2 is the reason for the low energy efficiencies it is also the reason for the high yields in the case of argon. Therefore in order to overcome the thermodynamic limits of CO_2 dissociation a plasma needs to be designed in a way that provides a reduced electric field where most of the electron energy is going into the channels that lead to dissociation for a pure CO_2 plasma, preferably at atmospheric pressure. Studies in pure CO_2 plasmas have shown that much higher reduced electric fields are required to achieve the desired electron loss channels [116]. The ideal reduced electric fields may be achievable in microwave plasmas but most current plasmas of this type have been shown to thermally dissociate CO_2 [36]. Dielectric barrier discharges have also been shown to have too high reduced electric fields where most of the electron energy is going into electronic excitation or ionisation

channels [116]. This would mean that most dissociation in DBDs is due to direct electron impact which is inherently less efficient than by vibrational excitation as it requires electron energies higher than the dissociation energy of CO_2.

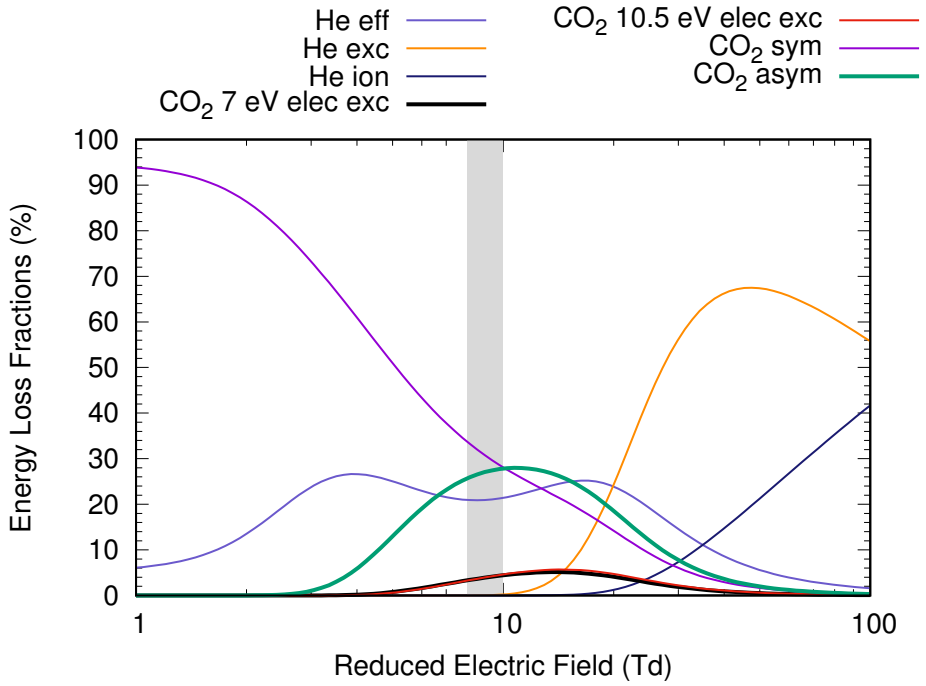

FIGURE 6.13: The energy loss fractions for the helium electron impact reactions, the electronic excitation of CO_2, as well as the symmetric vibrational excitation and asymmetric vibrational excitations above 4.5 eV, loss channels in a helium plasma with 1.5% CO_2 as a admixture as a function of the reduced electric field. The vibrational excitations above 4.5 eV are the ones found to cause dissociation and so only the loss fractions to dissociative asymmetric stretches are shown. The energy loss fractions were calculated using Bolsig+ with the same cross sections as in the global model. The desirable electron energy loss fractions are shown in bold in this figure.

Due to the large amount of electron energy that is lost to momentum transfer collisions with helium, for those plasmas the majority of the electron energy is not going into desirable channels, as seen in figure 6.13. The channels in which the electron energy is being deposited are similar for both helium and argon however there is a much smaller fraction of the electron energy which is going into the desirable channels in helium resulting in less CO being produced for the same specific energy input. This explains why although they have very similar dissociation pathways, shown in Figures 6.1 and 6.3, the two carrier gases produce very different yields. Other noble gases also exhibit a Ramsauer minimum like argon and should produce similar results to that of argon. However the electron energy

distribution functions and electron densities also have to be considered when considering how effective the carrier gas will be. Other noble gases are also more expensive than argon and in terms of CO produced per cost of a litre of carrier gas argon is likely to be the best choice of carrier gas.

6.5.1 Undesirable Electron Energy Loss Channels

Whilst a considerable amount of the electron energy is being deposited in the channels that will lead to dissociation a significant amount is still going into undesirable channels. The symmetric stretch of CO_2 is the main loss channel for plasmas with very low reduced electric fields and is still a large source of energy loss for the region of interest. Losing energy in symmetric CO_2 stretches is an unavoidable loss channel for electron energy.

By increasing the reduced electric field it would be possible to limit the amount of electron energy being lost to symmetric stretches and reach the peak of the curves for the desirable energy losses. Moving further to the right would also increase the amount of electron energy losses going into the 10.5 eV electronic state of CO_2 and excitation of metastable states in the noble gases. The 10.5 eV electronic state of CO_2 is not considered to lead to dissociation, as discussed earlier in the chapter, and is just another loss channel but the metastable states of helium and argon could potentially cause more CO_2 to dissociate through Penning dissociation [129], but again this requires more energy than the dissociation energy of CO_2.

However other Penning reactions also occur such as Penning ionisation [98], which would not cause CO_2 to dissociate except through dissociative reattachment which is not common according to the pathway analysis and supported by the energy loss fraction figures, which show very little energy being lost to metastable states of argon and helium. Penning dissociation would also not be a very efficient route to dissociation of CO_2 as the energy of the metastable states is 11.6 eV for argon and 19.85 eV for helium, both are high and above even the energy required for direct electron impact dissociation of CO_2. Due to the energy of the first metastable state of argon being close in energy to the 10.5 eV electronic state of CO_2 in the case of an argon plasma far more of the electron energy, for higher reduced electric fields, is lost to the argon excitation due to the higher density. In relation to helium since its metastable state is of much higher energy higher

reduced electric fields are required for a significant amount of the electron energy to be lost in this channel and so instead for slightly higher reduced electric fields the 10.5 eV electronic state of CO_2 starts to become a large loss channel for electron energy.

A slight increase in reduced electric fields may be possible experimentally by employing tailored waveforms to manipulate the electron energy distribution function and increase the mean electron energy. Using dual frequencies to drive a plasma has become an increasingly popular area of research [130–133]. Manipulating the EEDF to increase the mean electron energy will have the advantage of reducing the number of low energy electrons incapable of producing CO_2 states of high enough energy to produce CO and also create a plasma with a reduced electric field that corresponds to the maximum in the energy losses in asymmetric states in figure 6.12. If more energy is provided in these states for constant input power the yield should increase which would in turn increase the energy efficiency.

6.6 Energy Losses at the End of the Plasma

The energy loss fractions in the previous sections were somewhat idealised pictures of the plasma. In reality those figures would only be true in the first instance of the plasma and as soon as some of the CO_2 starts to dissociate other species would be produced that would create new loss channels for the electron energy and reduce the density of CO_2 and the energy loss coefficient and in turn the energy loss fraction in the desired channel. Figure 6.14 shows the energy loss fractions for an argon plasma with an admixture of 1.5% CO_2 at the end of the plasma. This means that of the 1.5% CO_2 admixture nearly 70% is now CO and this has a large effect on the energy loss fractions.

For the sake of simplicity most of the electron energy loss channels have been removed from Figure 6.14, especially for high reduced electric fields. It is clear that at the end of the plasma most of the electron energy is shifting into some form of CO excitation, have been summed into a single loss channel to clearly show the extent to which the electron energy is being lost. For the reduced electric field of the plasma, the region shaded, over 50% of the electron energy is being lost to some form of CO excitation and this loss would have been steadily increasing as the gas moved through the plasma. This is in part an explanation of why a trade

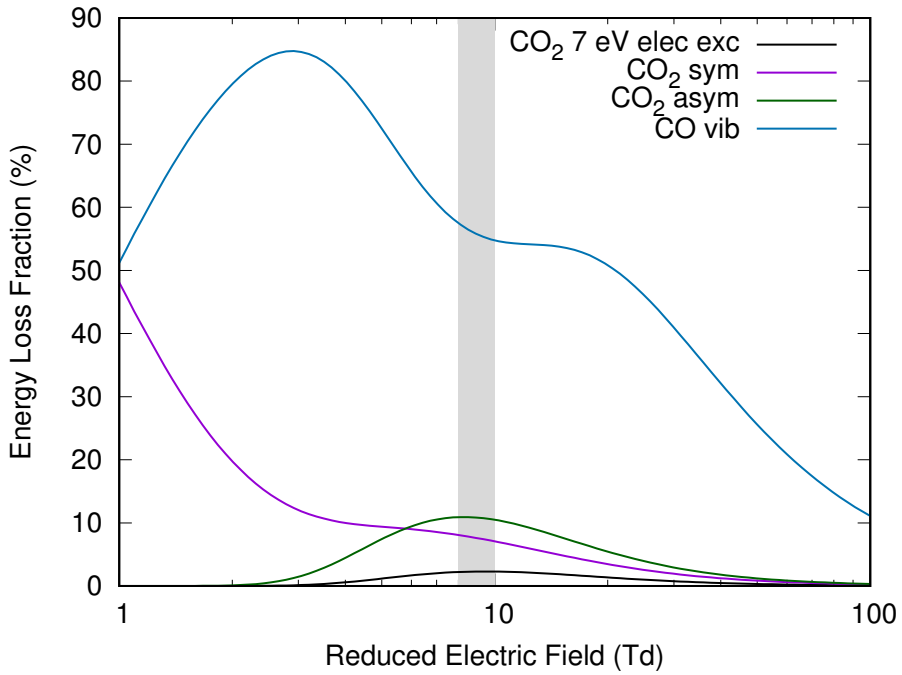

FIGURE 6.14: The energy loss fractions of an argon CO_2 plasma with a 1.5% admixture at the end of the plasma. This means that 70%, the yield of CO, of the 1.5% CO_2 admixture is now CO and this has a clear effect on the electron energy loss fractions. For simplicity most of the electron energy loss channels have been removed from the figure, particularly at the high end of the reduced electric fields. At the end of the plasma most of the electron energy is going into some form of CO excitation which is not desirable or useful for the production of CO and this will decrease the energy efficiency of the plasma.

off between yield and energy efficiency is always observed. The energy efficient plasmas do not convert a lot of CO_2 due to the electron energy not being deposited into channels that will cause dissociation and the high yield plasmas will start to not put the electron energy into dissociative channels due to the large reduction of CO_2 density. An increase in densities of other species will arise causing the electron energy to go into undesirable channels.

The electron energy deposited into CO is wasted energy but it is not actively reducing the CO yield. This is due to CO having a much higher dissociation energy than CO_2, of 9.77 eV. The high dissociation energy in comparison to the mean electron energy of the plasma means that very little of the carbon monoxide is dissociated and instead will just be quenched to the ground state in the effluent, as stated earlier in the pathway analysis most of the CO produced by the plasma remains CO. Although CO can be vibrationally excited, like CO_2, the high dissociation energy energy means that CO does not dissociate effectively through electron impact reactions, in this type of plasma, as observed with CO_2. This

result suggests that the energy efficiency can be improved by increasing the flow rate of the plasma to reduce the amount of energy lost in CO and reduce the specific energy input per molecule of CO_2. This will, of course, reduce the yield of CO.

6.7 Tailoring the Flow Rate

Figure 6.15 shows how the yield and energy efficiency change for an argon plasma with a 1.5% CO_2 admixture between 100 and 10 000 sccm. Varying the flow rate shows the expected result on the yield. As the residence time is increased, by reducing the flow rate, the yield increases up to the maximum yields seen in the model. As the residence time decreases the yield also decreases. The trend in energy efficiency also follows what is expected, with the energy efficiency increasing with flow rate due to the specific energy input per molecule of CO_2 been lower. However, eventually the yield drops so low with the increasing flow rate that it negates the lower specific energy input and the energy efficiency begins to decrease again.

The peak in the energy efficiency occurs for a flow rate of 4000 sccm and the energy efficiency has increased from 6% to 8%. The increase in energy efficiency is only slight as the yield in CO drops from nearly 65% to 25%, once again showing the trade off between energy efficiency and yield. Although the electron energy should be deposited into the desired channels with a higher flow rate, due to CO_2 making up a greater proportion of the admixture, the low residence time means that there is simply less chance of dissociation occurring and a low yield is to be expected. At the other end of the scale where the flow rate is very low the yield is shown to reach a maximum. This maximum is at just over 90%, which is the same maximum seen in the admixture variation results in the model but lower than that observed in the experiment. Since the experiment observed yields approaching 100% it is possible that this limit is purely numerical in the model and higher yields could be achieved experimentally with lower admixtures as shown in the previous chapter.

The reason for the saturation in the yield however can be explained by the energy loss fractions analysis shown in this chapter. For the low flow rate simulations the residence time is so large that nearly all the CO_2 has the chance to be

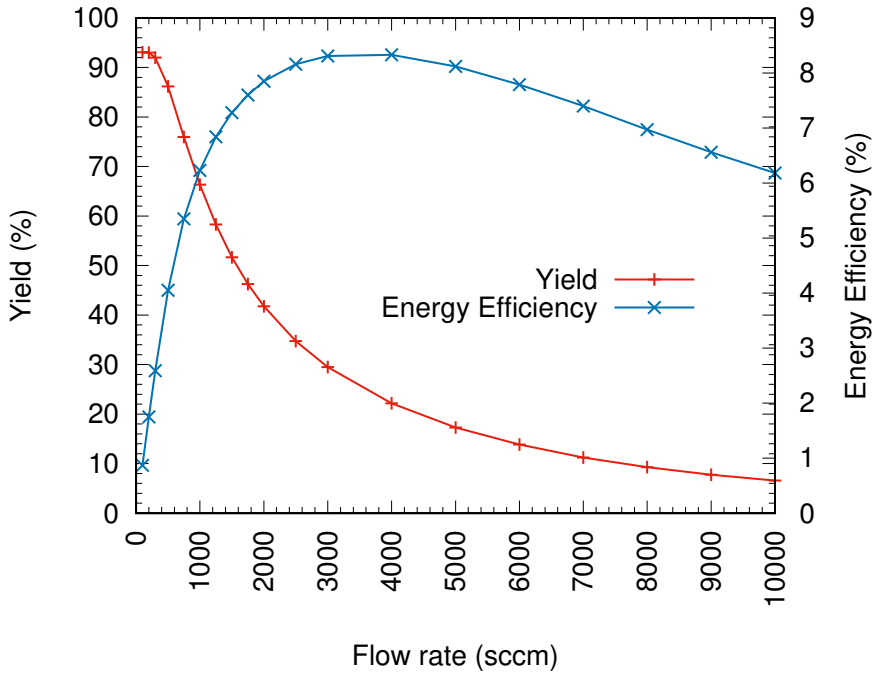

FIGURE 6.15: The flow rate of an argon plasma with a 1.5% CO_2 admixture is varied between 100 and 10 000 sccm. If the residence time is increased the yield of CO increases and correspondingly as it is decreased the yield decreases. Decreasing the residence time also decreases the specific energy input per molecule of CO_2 and therefore increases the energy efficiency. When the yield drops too low the effect of the lower specific energy input is negated and the energy efficiency starts to drop again.

dissociated through the dissociative pathways but as the CO_2 density decreases electron energy is more likely to be lost in reactions with CO and so eventually the chance of the electron energy being deposited into CO_2 channels that cause dissociation is so small that no more can be dissociated and a maximum yield is obtained.

Chapter 7

Two-Photon Absorption Laser Induced Fluorescence of Atomic Oxygen and Carbon Monoxide

7.1 The Advantages to Using TALIF

In the previous chapter the analysis of the production pathways of carbon monoxide showed that the recycling of atomic oxygen produced in the dissociation of CO_2 to further produce CO and O_2 is very important in the dissociation process in these plasmas and is an efficient way of dissociating CO_2. It is not possible to detect atomic oxygen using FTIR spectroscopy and it would also not be possible to measure atomic oxygen in the far effluent as it is a very short lived species. However it is possible to detect atomic oxygen using Two-photon absorption laser induced fluorescence (TALIF) [134–136].

TALIF is not only capable of detecting atomic oxygen, and other species of interest such as carbon monoxide, but also it is possible to position the laser so that it passes just into the effluent of the plasma, millimetres from the plasma itself where atomic oxygen will still be present in the gas and the carbon monoxide densities can be compared to those measured using the FTIR to show whether, as the model predicts, there is little chemistry occurring in the effluent. The measured ground state densities can be compared to the densities in the simulations to see

if they are in good agreement, and if so it provides further evidence to support the pathway analysis for the dissociation of CO_2.

TALIF is an active and direct diagnostic technique. This means that the laser will interact with the plasma effluent and requires calibration in order to determine the absolute densities of the measured species. Ideally, a diagnostic should be passive and direct, meaning that all of the information analysed comes from the plasma itself and requires no external stimulus and does not require calibration to obtain absolute densities. However practicality must be considered in experiments and often active techniques are required in order to obtain a signal strong enough to detect. For atomic species the energy of the photons required to stimulate an excited state from which to detect the fluorescence, can be so large that the wavelength of the photon is in the vacuum ultra-violet region of the electromagnetic spectrum. These wavelengths are readily absorbed by atmospheric species and so is not often used to detect species at atmospheric pressure [89, 137, 138]. By using two-photon excitation the laser wavelengths can be in the ultra-violet region. However, by using two-photon absorption the required energy is approximately halved so that it is not absorbed by atmospheric species and can be used in atmospheric conditions. Therefore TALIF can be used instead of LIF for these experiments. The cost of using TALIF instead of LIF comes in the required laser intensities as the likelihood of two photons being absorbed is much lower than a single photon and the fluorescence signal is much lower and greater laser intensities are required for detectable fluorescence signals.

7.2 Two-Photon Absorption Laser Induced fluorescence

The absolute ground state densities of species can be measured using TALIF by considering the excitation process from the ground state into an excited state and the subsequent decay producing a fluorescence photon. Figure 7.1 shows a simple three state system to demonstrate TALIF. In order to obtain ground state densities the fluorescence signal must be calibrated with a gas of known density. For gases such as atomic oxygen that cannot be provided in a bottle of known densities a calibration gas must be used with a two-photon resonance in the same spectral region as the species of interest [139].

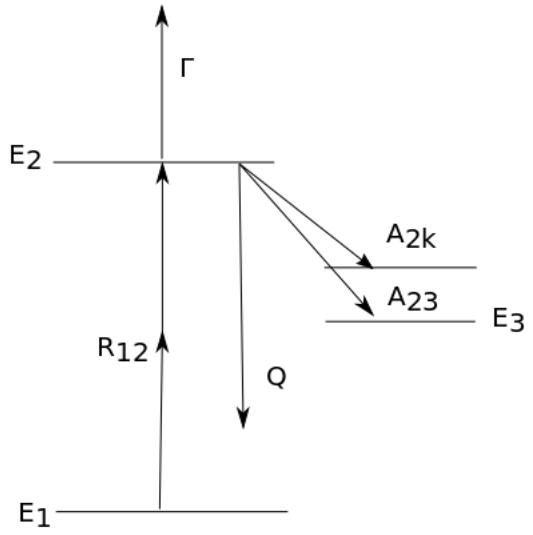

FIGURE 7.1: The TALIF process for a three state system. An electron is excited from the ground state, E_1, into an excited state, E_2, where there are then multiple available processes. The electron could be excited beyond the ionisation energy through Γ or de-excite through radiative decay, A_{2k}, or collisional quenching Q. The radiative decay into state E_3 releases a photon with the desired wavelength for detection.

The population density of the excited state, n_2, and the ground state, n_1, are given by equations 7.1 and 7.2 respectively, where R(t) is the excitation rate, A is the fluorescence rate of the excited state, Q is the quenching rate and Γ(t) is the ionisation rate. These continuity equations simply state that the only way the ground state is depopulated is through excitation and the excited state is populated through excitation from the ground state and is depopulated through fluorescence, quenching and ionisation.

$$\frac{d}{dt}n_2(t) = R(t)n_1(t) - (A + Q + \Gamma(t))n_2(t) \tag{7.1}$$

$$\frac{d}{dt}n_1(t) = -R(t)n_1(t) \tag{7.2}$$

The rate of excitation in TALIF is given in equation 7.3 where G is the photon statistic factor, which is 2 for a stochastic multi-mode field [140]. σ is the photon excitation cross section, $g(\nu)$ is the normalised line profile, I_o is the laser intensity and $h\nu$ is the photon energy. The rate of excitation depends on the square of all

the terms except the line profile due to two resonance photons being required for the excitation.

$$R(t) = G^2\sigma^2 g(\nu)\Big(\frac{I_o(t)}{h\nu}\Big)^2 \tag{7.3}$$

In order to be able to determine the ground state density of a species by measuring the fluorescence the different channels of depopulation of the excited state must be considered accurately. Since the depopulation of the excited state through fluorescence is how the ground state density is measured it is the most obvious form of de-excitation to consider. The total decay rate is given in equation 7.4 and is the sum all of possible rates into lower states, k. The decays rate of interest is the fluorescence decay rate into state E_3, A_{23}. It is possible to calculate the natural lifetime of the state from this decay rate, simply by taking the reciprocal of the decay rate.

$$A_2 = \sum_k A_{2k} \tag{7.4}$$

In an atmospheric pressure plasma the system is highly collisional and so collisional quenching, Q, must also be considered. In collisional quenching the excited state is depopulated through collisions and the energy of the excited state is not given off as a fluorescence photons and therefore if collisional quenching is not taken into account the ground state density will be underestimated due to there being less fluorescence signal than would be expected in a collisionless system.

Collisional quenching also reduces the effective lifetime of the excited state so that the lifetime calculated during a TALIF experiment will be much lower than the natural lifetime of the species. Different plasma species quench species at different rates. If the main quenching species densities and their quenching rates are known the lifetime of a species can be calculated using equation 7.5. In a highly collisional atmospheric pressure plasma the quenching rate is very important to the overall accuracy of the ground state density and is the largest lost process for the excited energy state.

$$Q = \sum_q n_q k_q \tag{7.5}$$

Quenching coefficients can be measured for species of interest by measuring the decay rate against the partial pressure of the quenching gas [136, 141–143] and the natural lifetime of the species can also be calculated by extrapolating the measured lifetimes to a partial pressure of zero. Equation 7.5 shows, however, that knowing the quenching rate coefficient is not the only value that needs to be known for measuring the quenching rate. The density of the species also needs to be known in order to calculate the quenching rate and this can be problematic for certain species. The density of the carrier gases are well known as they are inert and controlled by the mass flow controllers. Therefore in the case of argon, an effective quencher, most of the quenching is done by a species of known density. However for helium the densities of CO_2, CO and O_2 can have a large effect on the overall quenching rate and the exact densities of these species is not known at the point of the TALIF measurement. The model can be used to obtain approximate species densities at this point with some confidence due to the good agreement with the FTIR results, but this does add more uncertainty into the measurements. This uncertainty can be overcome by measuring the effective lifetime directly during the measurements because of the use of a pico-second laser. This will be explained in more detail subsequently in this chapter.

The last loss mechanism to consider is ionisation, where a third photon excites an electron in the excited state so that it has sufficient energy to ionise and therefore will not decay into the fluorescence state. For small laser intensities the ionisation rate is negligible and the excited state will not be depleted in this way. The ionisation rate is given in equation 7.6. Therefore if the laser intensity is kept low enough that photo-ionisation is negligible only collisional quenching and fluorescence need to be considered to calculate the ground state density.

$$\Gamma(t) = \frac{\sigma_i}{h\nu} I_o(t) \tag{7.6}$$

In order to determine if photo-ionisation is occurring the fluorescence signal of a species is measured with a varying laser energy and intensity. In a regime where photo-ionisation is negligible the fluorescence signal will be proportional to the square of the intensity and for the regime where photo-ionisation becomes

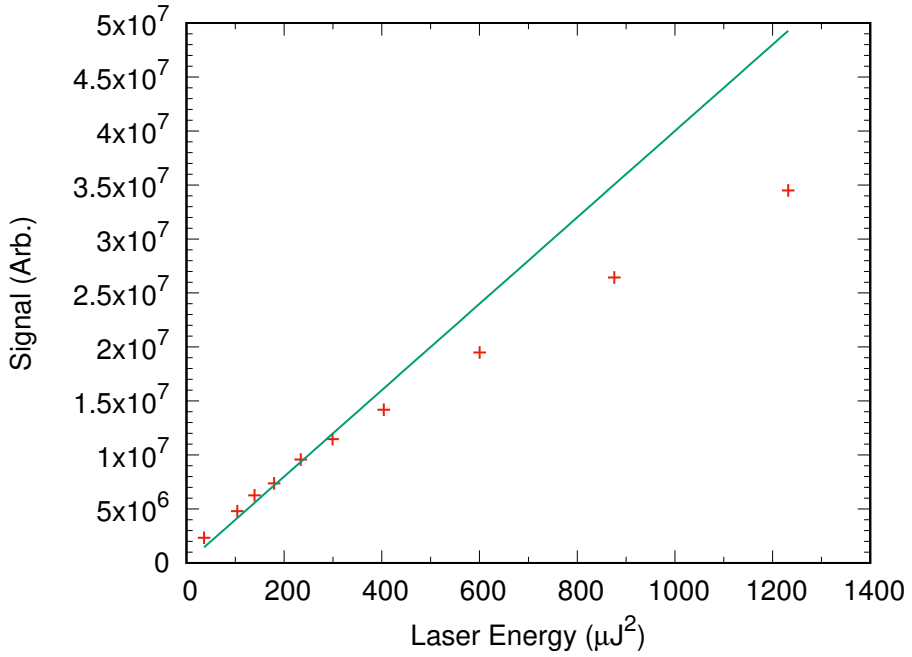

FIGURE 7.2: The fluorescence signal of CO as a function of the square of the laser energy, showing how for the low laser energies where photo-ionisation is negligible the fluorescence signal is linearly dependent on the square of the intensity. However after 300 μJ^2 the fluorescence signal begins to saturate and photo-ionisation is having a significant effect on the excited state density.

important this proportionality will no longer be the case and the iCCD signal will become saturated. Figure 7.2 shows a saturation to determine laser energies where photo-ionisation does not have to be considered in the analysis of the fluorescence signal.

Figure 7.2 shows the fluorescence signal of CO as a function of the square of the laser energy. There is a clear linear dependence on the square of the laser energy for low laser energies where photo-ionisation is negligible. For laser energies of more than 300 μJ^2 photo-ionisation becomes a prominent process and saturation of the fluorescence signal starts to occur. In order to simplify the analysis of the fluorescence signal the laser energy used in the measurements is kept in the regime that is linearly dependent on the square of the laser intensity so photo-ionisation does not need to be considered.

7.3 Calibration of the Fluorescence Signal

In order to obtain the ground state densities of species the fluorescence signal for the plasma must be normalised to the fluorescence signal of a known density. This is easy for the case of carbon monoxide where a bottle can be used to fill a chamber of a known volume and temperature to a known pressure and therefore the density can be calculated. For atomic oxygen, however, it is not possible to obtain a stable chamber as it is energetically favourable for oxygen to be diatomic and so in order to calibrate the fluorescence signal of atomic oxygen a noble gas is often used [139].

Using an inert gas means that it is straightforward to have a known density in the same way as carbon monoxide. When choosing a noble gas to use the transition from the ground state to the excited state must be in a similar spectral region to the species of interest. This is to ensure that the laser system has the same spatial spectral and temporal shape [144]. For atomic oxygen the noble gas used is xenon. The two photon excitation wavelength for atomic oxygen is 225.65 nm and for xenon it is 224.31 nm, therefore a quantitative comparison between the two fluorescence signals can be made as long as the regime used is linearly dependent on the intensity squared. Photo-ionisation will exhibit different dependencies on laser intensity with different gases and then calibration will not be possible.

In order to determine the ground state density of a species of interest from a reference gas ratios of the fluorescence signals, S_R for the reference gas and S_X for the species of interest, are taken and the ground state density of species of interest, n_X, can be determined using equation 7.7.

$$n_X = \frac{\eta_R}{\eta_X}\frac{T_R}{T_X}\left(\frac{\lambda_R}{\lambda_X}\right)^2\frac{\sigma_R^2}{\sigma_R^2}\frac{a_{23R}}{a_{23X}}\left(\frac{E_R}{E_X}\right)^2\frac{S_X}{S_R}n_R \tag{7.7}$$

η is the detection sensitivity and T the optical transmission which are both either known or easy to determine experimentally to a high level of precision, and the wavelengths, λ, of the excitation photons are also known. The ratio of the two-photon excitation cross sections, σ, are taken from the literature. The individual cross-sections for the species of interest and the inert gas, in this case atomic oxygen and xenon, are not known but their ratios have been measured

experimentally with good precision, estimated to be 20% [136]. As wavelengths for the species of interest and reference gas are in the same spectral region only the total energy, E, of the laser pulse, for both the calibration and the measurement of the species of interest, is required and the optical branching ratios are known from the natural radiative decay rates and the effective decay rates measured during the experiment.

In the case of carbon monoxide the ratio of signals is still required to determine the ground state densities but many of the terms in equation 7.7 will be one due to the calibration gas being the same as the gas of interest. This reduces much of the dependence on literature values. The wavelengths used for the experiment and reference gas are exactly the same and so the laser properties will also be the same.

7.3.1 Pico-second TALIF

For a low pressure plasma the decay rate of the excited state is small and the lifetime of the excited state is relatively long, on the order of tens of nanoseconds. For these plasmas a nanosecond pulsed laser, typically a 5 ns pulse width, is sufficient to ensure that the rate of excitation is small compared to the rate of decay, 1/A. Therefore the excitation can be considered to be instantaneous and the decay of the excited state through fluorescence can be monitored and the decay rate, A, measured.

Due to the highly collisional environment of an atmospheric pressure plasma the lifetime of the excited state reduces from on the order of tens of nanoseconds to nanoseconds. This clearly causes a problem with measuring the decay rate, A, as for a nanosecond pulsed laser the time-scale of the laser pulse width is on the same order of magnitude as the lifetime of the species of interest. In this case the decay of the excited state becomes convoluted with the laser pulse and the decay rate cannot be measured and quenching coefficients must be used. This then limits the accuracy of the measurements as not all quenching coefficients are known or if they are they may not be known to sufficient accuracy.

Using a laser with a pulse width on the order of hundreds of picoseconds for atmospheric pressure conditions means that the laser pulse width will be small when compared to the lifetime of the excited state and therefore the decay rate

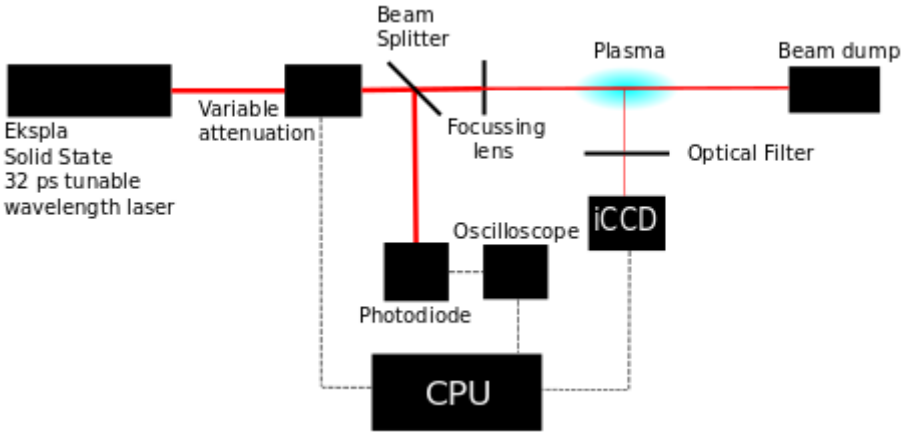

FIGURE 7.3: A Schematic of the TALIF set-up.

will be possible to measure by monitoring the fluorescence signal. Measuring of the decay rate is performed using an intensified charge coupled device (iCCD) that can resolve the fluorescence of the excited state on a time-scale of nanoseconds to monitor the decay of the signal with respect to time to obtain the decay rate (for a detailed explanation of the experimental procedure see [145]). A schematic of the experimental set-up is given in Figure 7.3. The laser used was a EKSPLA PL2251 series Nd:YAG pump laser and the iCCD used was an Andor iStar DH344T18U-73.

7.4 Measuring the Atomic Oxygen Density

In order to determine if atomic oxygen is being recycled to produce more CO the atomic oxygen density in the effluent needs to be measured and compared to the simulation values and the density of carbon monoxide. If all of the carbon monoxide produced is not from the recycling reaction then the atomic oxygen density should be of a similar order of magnitude to the carbon monoxide density. It is unlikely to be exactly the same due to atomic oxygen being more energetically table in a molecular form. If the atomic oxygen density compares well with the atomic oxygen density in the simulations then it gives credit to the pathway analysis and would appear likely that atomic oxygen is being recycled.

The two-photon excitation wavelengths used for measuring atomic oxygen are given in Figure 7.4 along with the two-photon excitation scheme for xenon, used for the calibration. The wavelength of the fluorescence signal is also given in this figure which is taken from [136] which includes the whole process for measuring

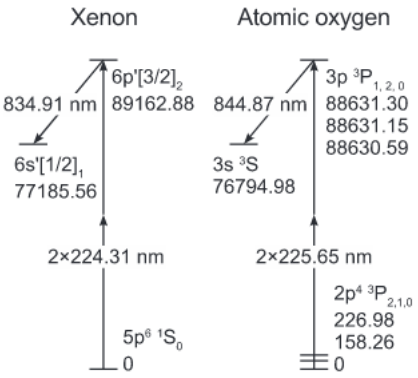

FIGURE 7.4: The two-photon excitation scheme used for the TALIF measurements for atomic oxygen and xenon for the calibration. The figure includes the wavelength of the excitation and the fluorescence and is taken from [136].

the ground state density of atomic oxygen. The laser energy was kept constant for the measurements at 20 μJ as this energy is before the TALIF signal starts to saturate, shown by figure 7.5.

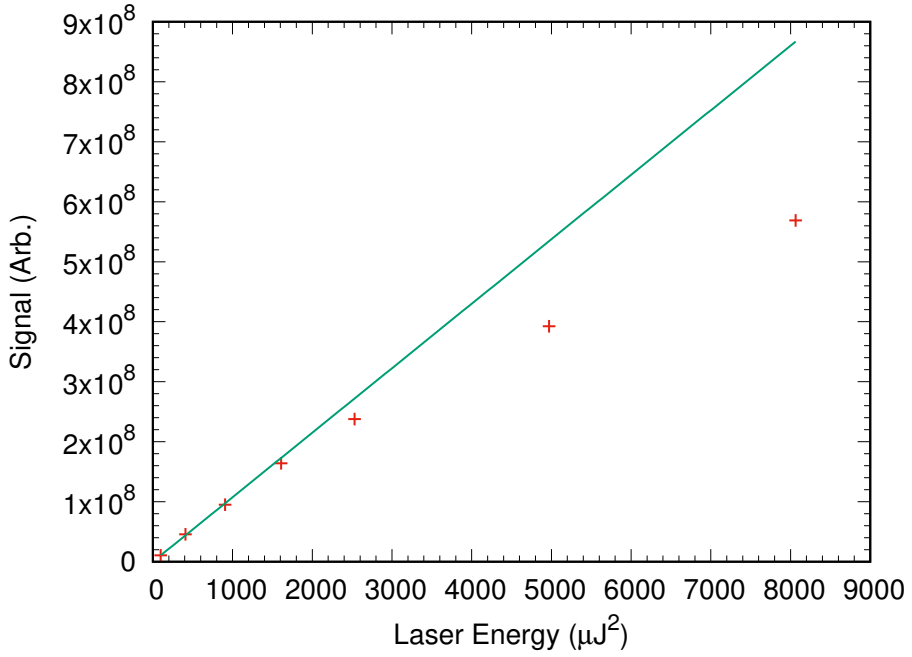

FIGURE 7.5: The fluorescence signal of O as a function of the square of the laser energy, showing how for the low laser energies where photo-ionisation is negligible the fluorescence signal is linearly dependent on the square of the intensity. A laser energy of 20 μJ was used for the measurements as this value is before the signal starts to become saturated.

7.4.1 Admixture Variation

In order to be able to compare the atomic oxygen densities with the simulations and the FTIR experiments they must be performed under the same conditions and, as before, these experiments were performed with a total flow rate of 1 slm and a plasma power of 30 W.

7.4.1.1 Argon

The measurements of atomic oxygen density with respect to CO_2 admixture are shown in Figure 7.6 and there is reasonable agreement between the TALIF measurements and the simulation results which are also plotted. The absolute densities between the TALIF results and the simulations do not align precisely over a factor of two difference between them. However, both the TALIF measurements and the rates governing the global models have uncertainties associated with them. The systematic error in the two photon excitation cross section is not shown in the error bar in these measurements due to it been constant across all measurements and is approximately 20 % [136].

The general trend observed in Figure 7.6 is similar between the experimental measurements and the simulation. There is some discrepancy in the smallest CO_2 admixture measured where in the TALIF measurement the atomic oxygen density lowers. This is likely to be due to the differences seen in yield for the low CO_2 admixtures where it has been observed to be close to 100% by the FTIR measurements but slightly below 90% for the simulations.

The trend in atomic oxygen densities observed is very different to the one observed for carbon monoxide in previous chapters. This suggests that there is not a simple splitting of CO_2 producing carbon monoxide and atomic oxygen, that would produce the same trend. Since the highest atomic oxygen densities are observed for the CO_2 admixtures that have the highest yields of CO and not the highest densities of CO it may be concluded that atomic oxygen reacts frequently with other admixture species. Since the highest atomic oxygen densities are observed where the CO density is lowest, the results of the pathway analysis seem accurate and atomic oxygen reacts to produce carbon monoxide. According to the pathway analysis the main production pathway of atomic oxygen is the dissociation of CO_2 through collisions with the carrier gas and the main loss mechanism is reacting

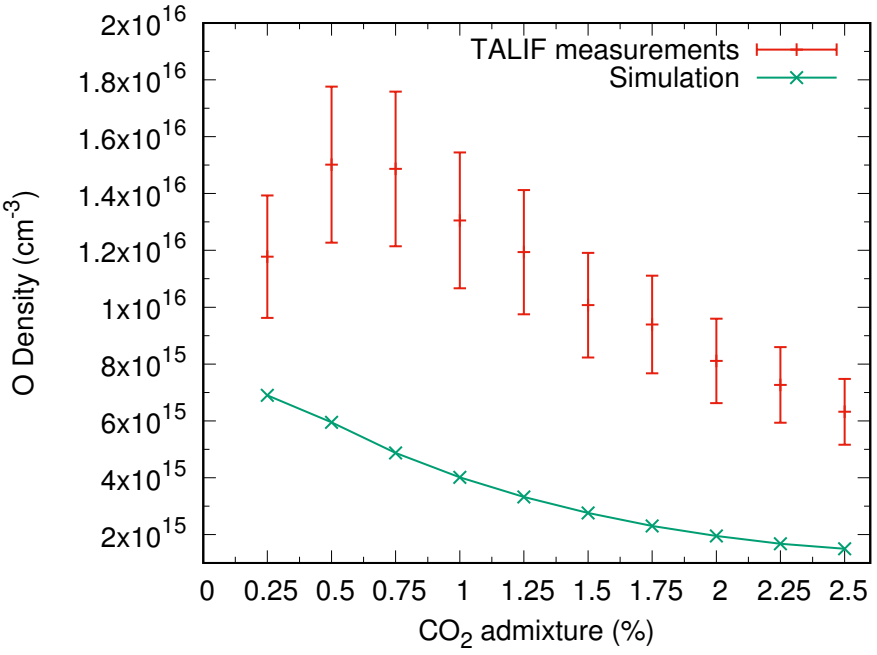

FIGURE 7.6: The density of atomic oxygen as a function of CO_2 admixture for an argon plasma with a plasma power of 30 W and flow rate of 1 slm measured using TALIF and compared to the simulation densities. There is reasonable agreement between the TALIF measurements and the simulation with both following the same general trend. The atomic oxygen density is almost two orders of magnitude lower than the carbon monoxide density measured in the FTIR which suggests that atomic oxygen is being recycled to create more carbon monoxide.

with vibrationally excited CO_2 to produce CO. Therefore the highest atomic oxygen densities would be expected for the highest yields, and not the highest CO density, as this is where production of atomic oxygen is highest be the destruction pathways are lowest, as observed in Figure 7.6.

7.4.1.2 Helium

Figure 7.7 shows the atomic oxygen density as a function of CO_2 admixture for the case of a helium carrier gas for both the TALIF measurements and the simulations. The absolute densities are in better agreement than for the argon case however the overall trend observed is not.

For the simulation results a very similar trend to the argon case is observed but the density for helium in slightly higher than for argon due to more atomic oxygen recycling occurring in the argon case due to a higher production of the

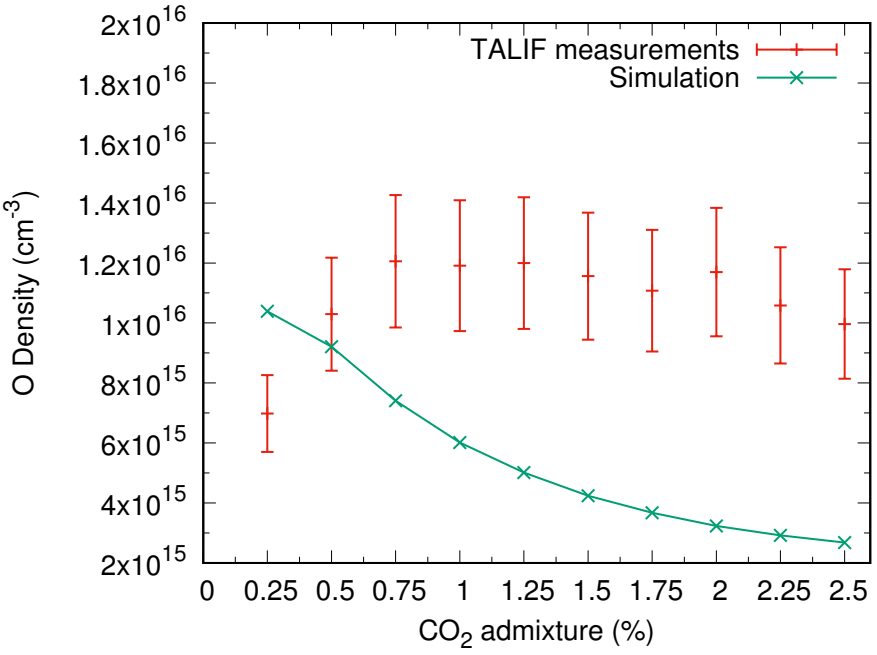

FIGURE 7.7: The density of atomic oxygen as a function of CO_2 admixture for a helium plasma with a plasma power of 30 W and a flow rate of 1 slm compared to the simulation densities. The agreement between the TALIF measurements and the simulations is less good for helium than for argon but the absolute densities are still in reasonable agreement.

dissociative asymmetric vibrational states of CO_2 in accordance with the pathway analysis in the previous chapter. For the TALIF measurements the trend observed is similar to the carbon monoxide density but the absolute values are an order of magnitude in difference. The atomic oxygen density appears to be fairly constant for high CO_2 admixtures as it is for carbon monoxide but the large difference in absolute density shows that it is not a simple splitting of CO_2 into CO and O.

7.4.1.3 Lifetime Comparison

In order to measure absolute densities the lifetime of the excited species is also measured and the comparison between the lifetimes in the two carrier gases can provide more information on the difference between the two. Figure 7.8 shows the lifetime of the excited state of atomic oxygen in helium and argon.

The lifetime of the excited species is always higher in helium than in argon and this shows that argon is a much more effective quencher than helium. The magnitude of the lifetime for both gases also shows why picosecond TALIF is

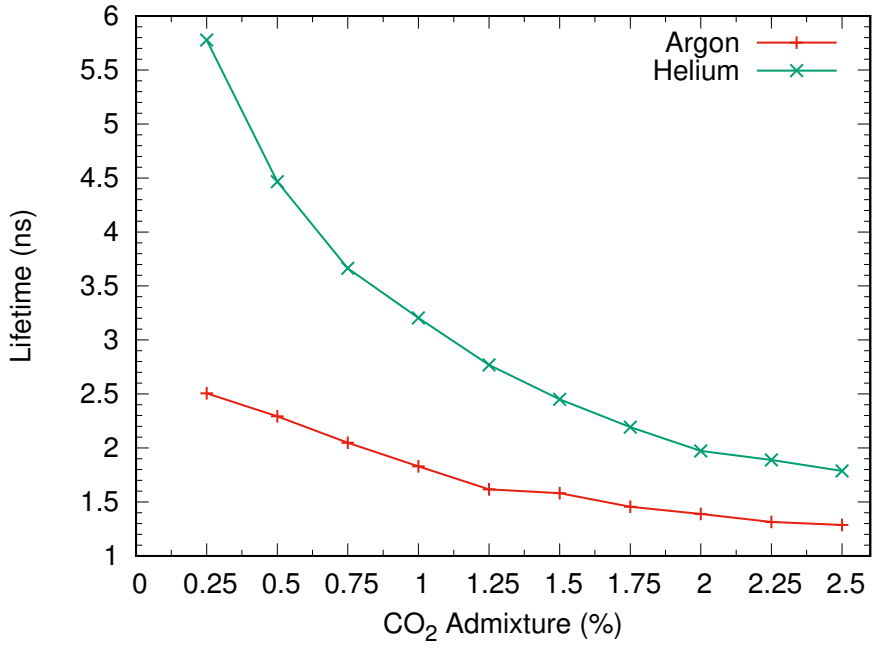

FIGURE 7.8: The lifetimes of the excited state of atomic oxygen in argon and helium. The lifetime in the helium plasma is much larger than in argon for very small CO_2 admixtures where the carrier gas is responsible for the majority of the collisional quenching. Therefore it is clear that argon is a much more efficient quencher than helium. The fairly close lifetimes for high CO_2 admixtures shows that the carrier gas admixture must also be considered when calculating the lifetime meaning that it can be difficult to obtain accurate lifetime measurements if they are not measured directly.

needed to measure species at atmospheric pressure as the lifetime for all cases is only a few nanoseconds. As the CO_2 admixture is increased the lifetime of the excited state of atomic oxygen decreases for both carrier gases. Therefore the admixture gas is having a noticeable, and is the case of helium very significant, effect on the effective lifetime of the species. The excited state of atomic oxygen these lifetimes could be calculated, using quenching coefficients [136, 146], to endeavour to provide accurate results but the exact concentrations of each species is not known. Quenching coefficients can also have a large uncertainty associated with them. For instance there is an order of magnitude difference in the helium quenching coefficient for Niemi et al. [136] and Bittner et al. [146], so although it is possible to calculate the lifetime using the coefficients from Bittner et al. the calculated lifetime is 1.8 ns and using the helium rate from Niemi et al. the calculated lifetime is 4.2 ns for a 0.5% CO_2 admixture in helium. Comparing this to Figure 7.8 there is good agreement for the Niemi et al. quenching coefficient but the Bittner et al. lifetime is much lower. In order to calculate the lifetimes

using the quenching coefficients the densities of the quenching species need to be known. These densities are usually not known and therefore the global model can be used to provide the relative species densities, but for this to be accurate the global model must also accurately predict all the quenching species densities. These uncertainties can be avoided by measuring the lifetime directly. In order to measure the absolute densities accurately the lifetimes need to be measured for each specific measurement. Since the excitation wavelengths for TALIF of atomic oxygen and carbon monoxide are similar, 225.65 nm and 230.10 nm respectively, carbon monoxide could effectively quench atomic oxygen as they have at least one similar energetic state.

7.4.2 Flow Variation

As well as varying the admixture to see if the atomic oxygen density supports the pathway analysis for the recombination of atomic oxygen it is also possible to vary the flow rate. Reducing the flow rate will increase the residence time of the gas in the plasma and this should increase the yield of CO. Increasing the dissociation of CO_2 should also increase the atomic oxygen density unless the atomic oxygen is being used to create more CO. However it is also possible that the increased residence time would simply provide more time in which the atomic oxygen could recombine with itself or O_2 and reduce the density in this way without having an effect on the CO density.

7.4.2.1 Argon

Figure 7.9 shows the atomic oxygen densities as a function of the flow rate for an argon plasma with a constant plasma power of 30 W and a constant CO_2 admixture of 1.5% for both TALIF measurements and the simulation. The trend observed in the TALIF measurements is what would be expected if atomic oxygen recycling was a common pathway for the production of carbon monoxide. As the flow rate decreases the residence time increases and the yield of CO is expected to increase. Since the dissociation of CO_2 is increasing the production of atomic oxygen is also increasing and so if atomic oxygen where not being recycled it would be expected that the atomic oxygen density would increase with increased residence time. Since the opposite trend is observed in the TALIF measurements

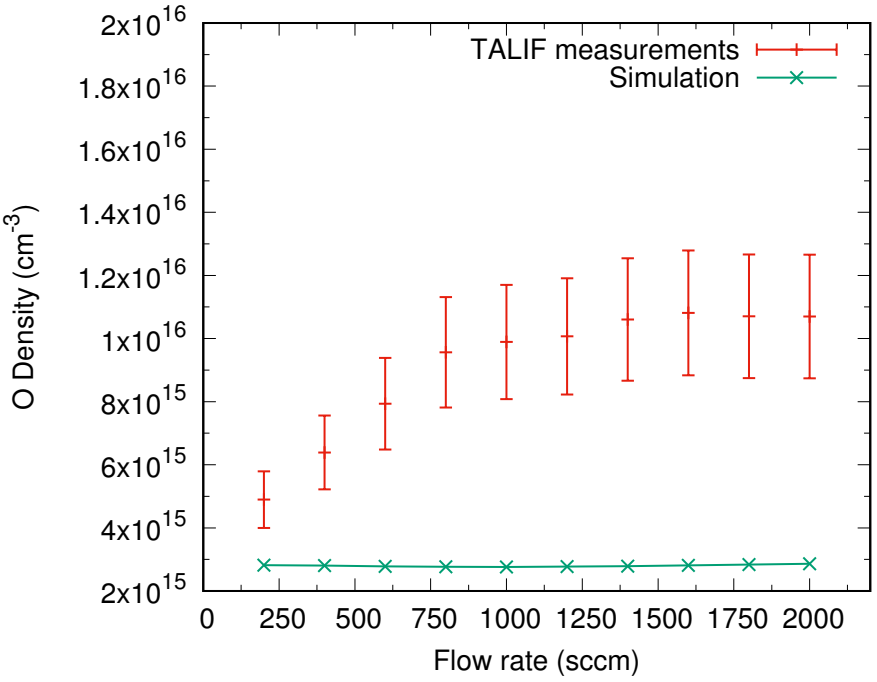

FIGURE 7.9: Atomic oxygen density in an argon plasma with a plasma power of 30 W and a constant CO_2 admixture of 1.5% as a function of flow rate. The trend in the experimental densities is what would be expected for atomic oxygen recycling with a longer residence time producing more carbon monoxide through atomic oxygen recycling. There is a reasonable agreement between the experimental and simulation results, however the trends are quite different.

it would seem that atomic oxygen is being used to produce more carbon monoxide as predicted by the pathway analysis of the model.

The comparison between the experimental measurements and the simulation in Figure 7.9 is not conclusive. The absolute densities are of a similar order of magnitude for the lower flow rates but the trends observed are slightly different. The trend in the simulations is constant across the different flow rates and this leads to a considerable difference in absolute density for the large flow rate values. This is most likely due to the lower yields producing smaller atomic oxygen densities for high flow rates and the extra atomic oxygen produced for lower flow rates is always used in further reactions and so the production is always matching destruction in the model whilst this is not true in the experiment and there is clearly some uncertainty in the rates of the atomic oxygen reactions.

7.4.2.2 Helium

Figure 7.10 shows the atomic oxygen density as a function of the flow rate for a fixed plasma power of 30 W and a fixed CO_2 admixture of 1.5% for both the TALIF measurements and the simulation. The experiment and the simulation results have reasonable agreement, within an order of magnitude, and the general trend between the two is also in reasonable agreement. Overall the smallest flow rates have the lowest atomic oxygen densities as is the case with argon. Slower flows have been shown in Chapter 5 to give higher conversions of CO_2 and therefore the production of atomic oxygen will also be higher. The trend observed however is that slower flows have lower atomic oxygen densities and this would indicate that atomic oxygen is been reused after the initial dissociation of CO_2 to produce more CO and O_2. Since the lower flow rates increase the residence time it is also possible that atomic oxygen is been depleted by other means such as recombination with itself, but this is not possible to determine experimentally and if the carbon monoxide density shows the opposite trend with flow rate, as expected, it seems

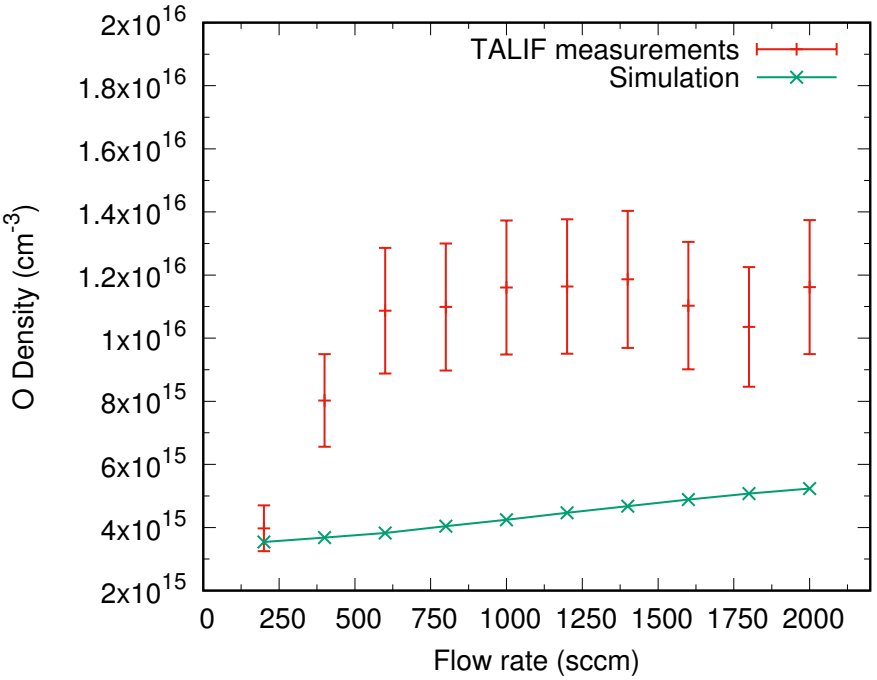

FIGURE 7.10: Atomic oxygen density as a function of flow rate for a helium plasma with a plasma power of 30 W and a CO_2 admixture of 1.5%. There is again reasonable agreement between the experiment and simulations with the absolute densities being of the same order of magnitude. The general trends also agree fairly well with the lowest flow rates having the lowest atomic oxygen density, which would suggest atomic oxygen is being used to produce more carbon monoxide.

reasonable to conclude that the recycling of atomic oxygen is an efficient and important dissociation process.

7.4.2.3 Lifetime Comparison

Figure 7.11 shows the variation in lifetimes for the flow variation for both argon and helium. Since the CO_2 admixture is constant for all the measurements as the density of the carrier gas the only things that will affect the value of the lifetime is the species present in the admixture at the end of the plasma which will be different for each measurement with more carbon monoxide and less carbon dioxide in low flow rate measurements and vice versa for high admixtures and the gas temperature. A higher gas temperature will decrease the lifetime of the state due to increased quenching rates and this could also potentially explain the observed trend, but it has not been measured.

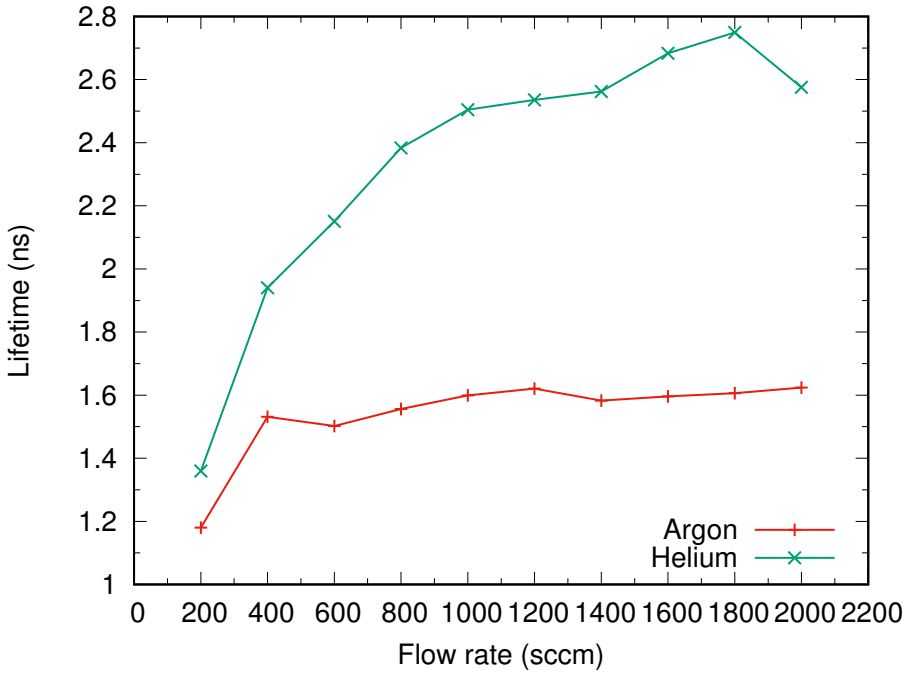

FIGURE 7.11: The lifetimes of the excited state of atomic oxygen as a function of the total flow rate of the input gases with a constant 1.5% CO_2 admixture. The lifetime changes substantially for helium due to the effect of small yields of carbon monoxide being produced for high flows, as the admixture remains constant it is only the contents of the admixture that will affect the lifetime. For argon the lifetime is fairly constant as argon is the most effective quencher.

The lifetime for argon is fairly constant for the different flow rates and this is expected as argon is a very effective quencher and its density remains unchanged

throughout the measurements. The lifetime for the 200 sccm flow rate reduces drastically for both argon and helium and this is likely due to the high degree of dissociation expected for the smallest flow rate. For helium, however, the lifetime is changing for the different flow rates due to helium being a poor quencher of atomic oxygen and a large proportion of the collisional quenching coming from the admixture despite the smaller densities. As the conversion starts to increase with smaller admixtures the lifetime reduces suggesting that CO is more effective at quenching atomic oxygen than CO_2 but both are not as effective as argon, largely due to their respective densities. The quenching coefficients of atomic oxygen for CO and CO_2 given in [146] are 4.9x10^{-16} m^3s^{-1} and 6.6x10^{-16} m^3s^{-1} respectively, and since these are very similar the large decrease in lifetimes of the excited state for the 200 sccm flow seems to be due to the increased gas temperature.

7.5 Measuring the Carbon Monoxide Density

Measuring the carbon monoxide density using TALIF is done in much the same way as atomic oxygen. The wavelength used for the two photon excitation and the fluorescence wavelengths are obviously different for carbon monoxide and the two-photon excitation used is 230.15 nm and the fluorescence signal is 486 nm in accordance with [147].

The main difference between using TALIF to measure carbon monoxide as opposed to atomic oxygen is that it is possible to store carbon monoxide in a known quantity and therefore carbon monoxide measurements can be calibrated with itself. Being able to calibrate the signal with a signal of exactly the same gas means that many of the approximations used for the unstable species are no longer present. The main source of uncertainty in the atomic oxygen measurements comes from the ratio of the excitation cross sections, which for atomic oxygen and xenon has an uncertainty of $\sim$20% [136]. Whilst the excitation cross sections are also not known for carbon monoxide, as with atomic oxygen and xenon, the ratio of the carbon monoxide cross section with the calibration gas is known to be one and this eliminates the main source of uncertainty in TALIF.

7.5.1 Admixture Variation

The admixture variation measurements were performed under the same conditions as the FTIR experiments, plasma power of 30 W and flow rate of 1 slm, to directly compare the carbon monoxide densities at the start of the effluent and far into the effluent. According to the simulation results there should not be any large difference between these two densities as carbon monoxide is a stable molecule and there is very little recombination in the effluent for the relatively low gas temperature in these plasmas.

7.5.1.1 Argon

The carbon monoxide densities as a function of admixture in an argon carrier gas are shown in Figure 7.12 for the TALIF measurements and the simulation. For small CO_2 admixtures there is reasonable agreement between the TALIF measurements and the simulation densities, however there is some discrepancy for the high CO_2 admixtures.

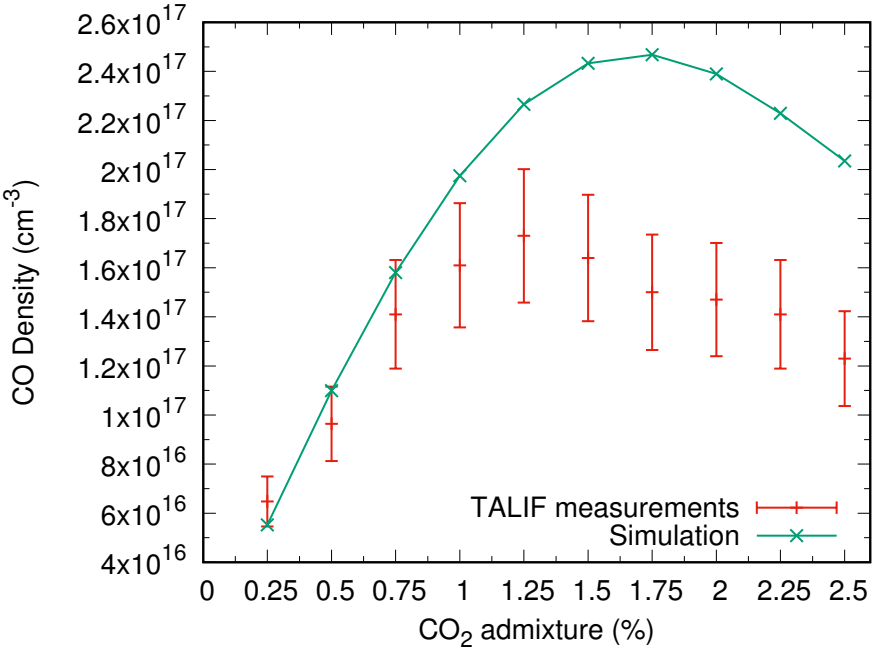

FIGURE 7.12: Carbon monoxide densities measured using TALIF for a constant plasma power of 30 W and flow rate of 1 slm. There is a reasonable agreement between the TALIF measurements and the simulations for low CO_2 admixtures, however for the higher values there is some discrepancy between the two values.

The TALIF measurements are performed just at the exit of the plasma less than 2 mm into the effluent. This is because atomic oxygen is a very short lived species and cannot be measured far into the effluent like carbon monoxide. Whilst carbon monoxide is a stable species that will not decay further into the effluent it is also a diatomic molecule. Diatomic molecules have more degrees of freedom than atoms as whilst they may be in the electronic ground state they are not necessarily in the vibrational ground state. Like CO_2, CO also has many vibrationally excited states up to the dissociation energy of 11.3 eV [148].

Just millimetres into the effluent it is still possible that carbon monoxide exists in a vibrationally excited state that would have relaxed down to the ground state by the time it would have reached the FTIR. If the carbon monoxide molecule is vibrationally excited the two photon excitation wavelength used would not have the correct energy to excite the molecule into a state that will fluoresce with a photon wavelength the camera is detecting. Therefore it is possible that by measuring the carbon monoxide density just in the effluent of the plasma the density measured is much lower than expected.

Figure 7.13 shows the carbon monoxide density from the simulations that include vibrational states of carbon monoxide in a similar manner as for CO_2 by using cross-sections to obtain electron impact excitation rate coefficients [149]. The ground state density at the end of the plasma is then plotted as well as the ground state density 2.5 mm into the effluent to cover the region where the TALIF measurements are performed. The area between the two simulation points is shaded as the TALIF measurements were performed between those two points. The agreement between the experiment and simulation is now much improved but there is still some disagreement for the CO_2 admixtures where gamma mode was observed in the FTIR experiments and it follows that if these admixtures are still in gamma mode the amount of ground state carbon monoxide depletion from vibrational excitation would be increased and the measured densities from TALIF would be lower than what is predicted by the model.

7.5.1.2 Helium

In a helium carrier gas the results are much the same as for argon. Figure 7.14 shows that the carbon monoxide density measured by TALIF is still consistently

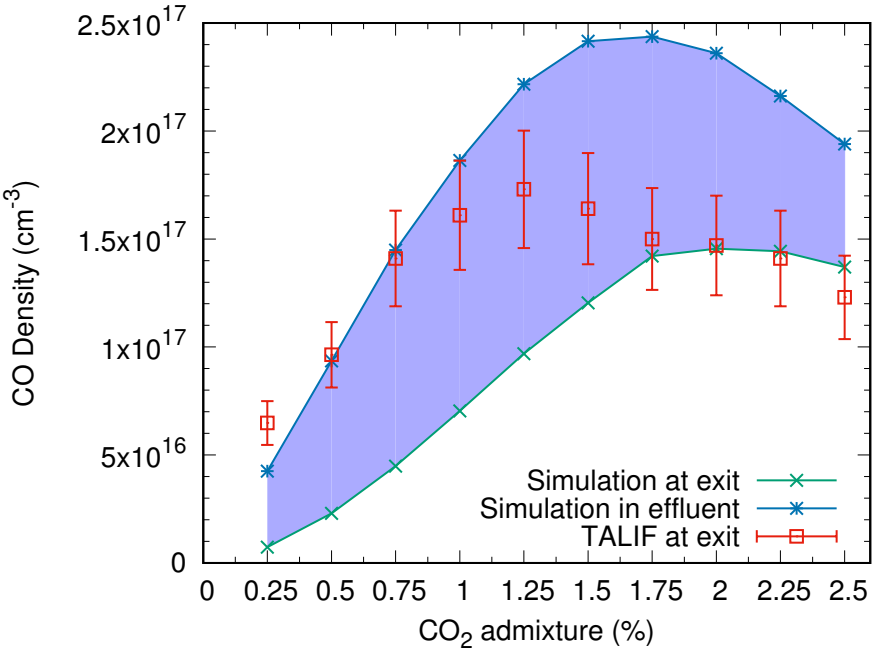

FIGURE 7.13: Comparing the TALIF measurements to just the ground state carbon monoxide densities in simulations that includes vibrational states of carbon monoxide at the exit of the plasma and 2.5 mm into the effluent there is much better agreement between the results. Therefore it seems likely that a significant portion of the carbon monoxide density is still vibrationally excited at the point where the TALIF measurements are performed leading to significantly lower carbon monoxide densities detected.

lower for all CO_2 admixtures than the simulation density. The overall trend however does agree well with the FTIR measurements which is to be expected as no discontinuity was seen in the helium measurements as there was with argon.

Figure 7.15 shows the TALIF measurements again compared with the ground state densities of carbon monoxide for simulations including the vibrational states of carbon monoxide as applied in the case of argon stated previously. As previously the agreement between the model and the simulation is improved with the TALIF measurements better matching the ground state densities of carbon monoxide just at the exit of the plasma. The simulation is over-predicting the ground state density of carbon monoxide. However, the simulations have always over-predicted the yield of carbon monoxide in helium and so this result is not unexpected. This Figure shows that is a considerably amount of vibrational excitation of carbon monoxide in the plasma, as with CO_2, but it is not dissociated due to the high bond energy of the molecule. This also supports the analysis of electron energy loss fractions that showed a significant amount of electron energy lost to carbon

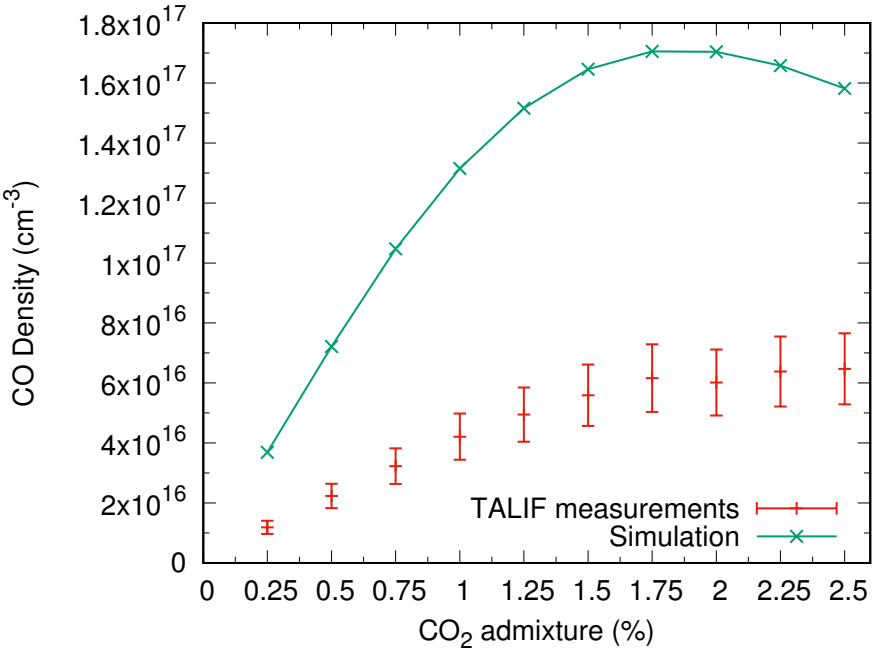

FIGURE 7.14: Carbon monoxide densities measured using TALIF for a constant plasma power of 30 W and flow rate of 1 slm. As with argon the TALIF measurements are consistently lower than the simulation density but the overall trend is similar to that of the FTIR measurements.

monoxide vibrational excitation at the exit of the plasma.

Therefore it is reasonable to conclude that the difference in ground state densities observed between the FTIR and TALIF experiments is due to electron induced vibrational states of CO still existing just into the effluent although they all decay back to the ground state by the time the gas reaches the FTIR gas cell. In order to determine if vibrational excitation is the cause of the discrepancy the TALIF measurements can be repeated further into the effluent where the excited carbon monoxide molecules have decayed back to the ground state using vibrational cross sections as described in Laporta et al. [149]. The simulation can be used to determine the appropriate distance.

7.5.1.3 Relaxation of Vibrationally Excited Carbon Monoxide

Whilst measuring just into the effluent is necessary for short lived atomic species such as atomic oxygen it does not give ideal results for diatomic molecules such as carbon monoxide the total density of the species are to be measured. Figure 7.16 shows that both the atomic oxygen and carbon monoxide density change

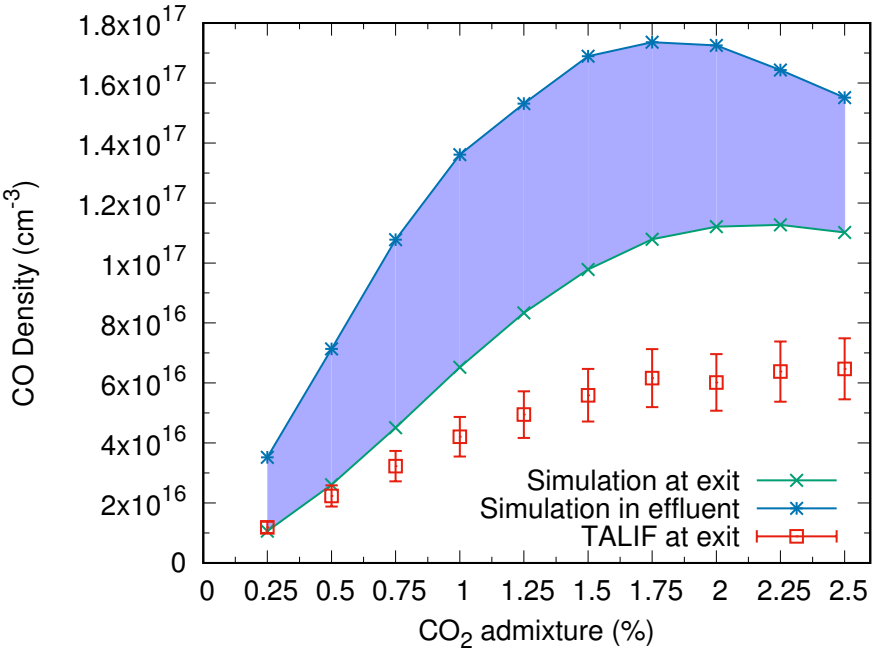

FIGURE 7.15: For a simulation that includes vibrational states of carbon monoxide the ground state densities of carbon monoxide agree very well with the TALIF measurements. The simulation densities for the ground state of carbon monoxide are taken at the exit of the plasma and 2.5 mm into the effluent in order to include the area where the TALIF measurements are performed.

drastically just outside the plasma. For the effluent simulations the input power is set to zero after 5 cm as that is the length of the electrodes and this causes the electron temperature to drop to zero and as such no electron dependent reactions occur afterwards. As such the production pathways for species such as atomic oxygen and vibrationally excited molecules drop to zero and the species density drops.

Within the first 5 mm of the effluent simulation, which was performed in an argon carrier gas with an admixture of 1.5% with a plasma power of 30 W and a flow rate of 1 slm, the ground state density of carbon monoxide reaches the same density as the previous simulations without the vibrational states of carbon monoxide. Therefore by measuring one or two centimetres into the effluent all of the carbon monoxide should have decayed back down to the ground state and the TALIF measurements should more closely match the FTIR experiments. The corresponding atomic oxygen densities at these distances have decayed to too low a level to be detected by TALIF however, showing the necessity to measure as close to the plasma as is possible in that case. Since the laser profile used for the TALIF measurements has a finite width it is possible to spatially resolve the

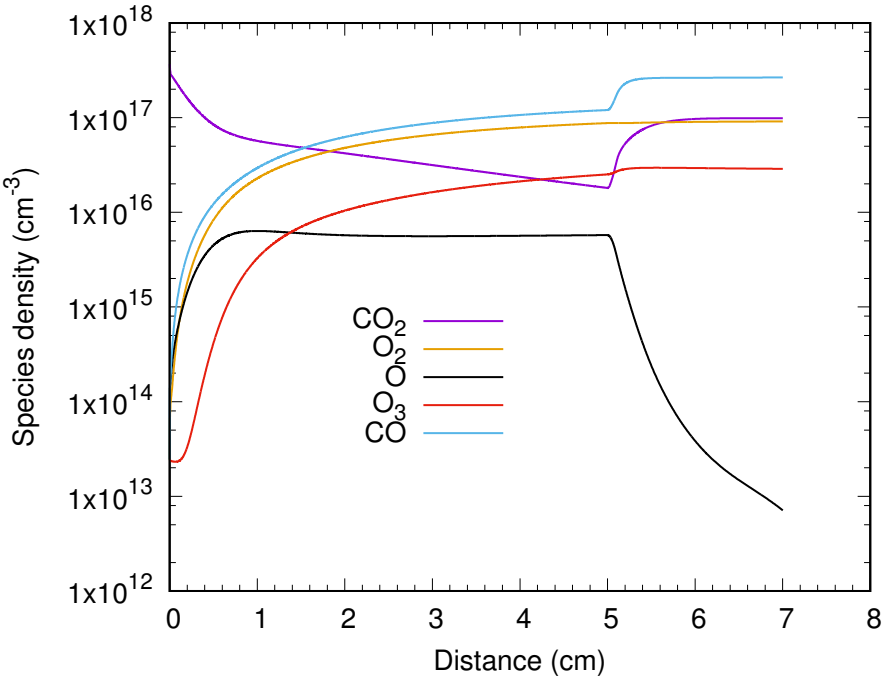

FIGURE 7.16: The species densities of ground state CO_2, CO, O_2, O_3 and O in an argon plasma with a 1.5% CO_2 admixture with a plasma power of 30 W and a flow rate of 1 slm. The ground state density of carbon monoxide rises sharply after the plasma for the first 5 mm until it reaches steady state due to the relaxation of vibrational states. This region is the region in which the TALIF measurements are performed and so this is likely to have an effect on the measured ground state density.

species density in the effluent and through this method it is possible to measure the decay rate of vibrationally excited carbon monoxide under the effluent conditions.

7.5.1.4 Lifetime

The minimum distance needed for all of the vibrational states of CO to decay will be different depending on the carrier gas. Figure 7.17 shows that argon is a very effective quencher of the excited state of carbon monoxide. Argon is so effective at quenching CO that it was not possible to accurately measure the decay rate using the iCCD. Although it was possible to detect the decay of the fluorescence signal in argon, it was too quick to obtain enough data points to reliably fit a exponential decay to the data and as such the absolute density measurements were not accurate. As a consequence it proved necessary to use quenching coefficients to calculate the effective lifetime for the conditions expected and then calculate the absolute density. The quenching coefficients are calculated from cross-sections

[143] for the different plasma species by multiplying them by the thermal velocity. There is a temperature dependence in the quenching rates which could be important for measurements performed at the exit of the plasma.

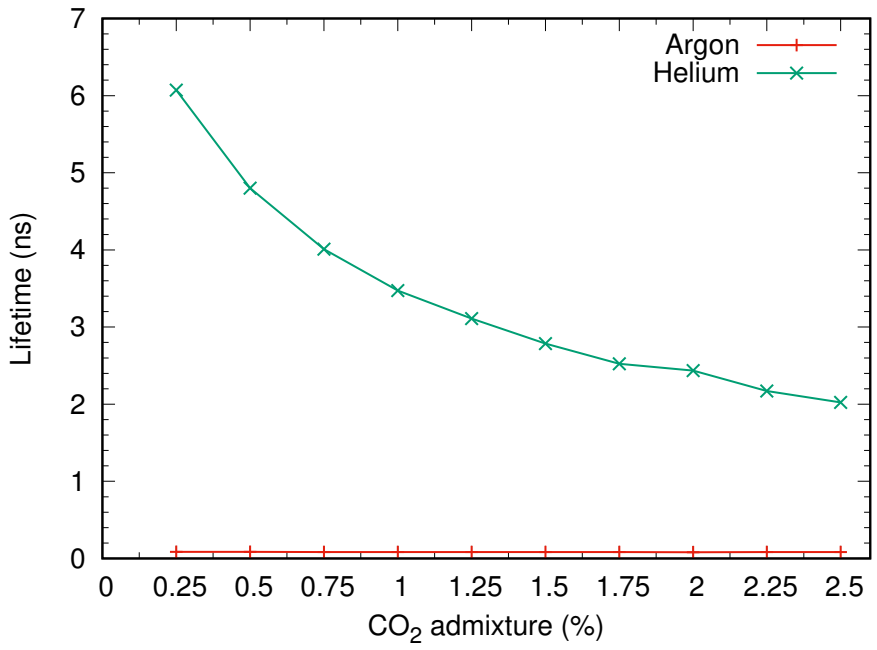

FIGURE 7.17: The lifetimes of the excited state of carbon monoxide in both a helium and argon carrier gas. As with the atomic oxygen lifetimes argon is a much more effective quencher than helium, so much so that the lifetime of the exited state in argon was calculated using quenching coefficients due to it being too low to accurately measure using the iCCD. There is also a large variation in the lifetime for a helium carrier gas showing that the CO_2 density has a larger effect on the lifetime than the helium density.

The lifetime of the excited state of CO for argon remains fairly constant with CO_2 admixture because argon is a far more effective quencher, due to the much higher density, than the other species. Since argon is shown to be a much more effective quencher of electronically excited carbon monoxide than helium it is also reasonable to assume that it is a much more effective quencher of vibrationally excited CO_2. This would mean that it is unlikely that an argon carrier gas would produce higher yields of carbon monoxide if the main dissociation pathway was through vibrational up-pumping and therefore the pathway analysis showing a two-step dissociation process seems like a more likely pathway.

The lifetime of the excited state of carbon monoxide in a helium carrier gas becomes smaller as the CO_2 admixture is increased. This is due to both carbon monoxide and carbon dioxide been more effective quenchers than helium and so

as the helium density decreases and the density of other plasma species increases the lifetime of the excited state of CO decreases.

7.5.2 Measuring the Carbon Monoxide Density in the Far Effluent

By repeating the CO density measurements in the far effluent via TALIF the measured density should much more closely reflect the total density of carbon monoxide due to the relaxation of the vibrational states. The first vibrational state of carbon monoxide has a vibrational energy of 0.27 eV which is equivalent to 3133 K. This is an order of magnitude higher than the gas temperature and therefore the gas temperature is not hot enough to populate the vibrational levels and due to electron impact excitation not being present in the far effluent there is no production of vibrationally excited CO. In order to keep the effluent free from contamination from the set-up used in the FTIR experiments was used and the laser was positioned just above the end of the swagelok piping.

The effluent TALIF measurements for an argon plasma are shown in Figure 7.18 along with TALIF measurements at the exit of the plasma and the simulation results. There is very good agreement between the TALIF measurements and the simulation for the effluent conditions. The effluent TALIF measurements are also consistently greater in magnitude than the measured densities just at the exit of the plasma. Therefore it is reasonable to deduce that there is a large amount of vibrationally excited carbon monoxide just in the effluent of the plasma that will affect the measured densities by reducing the fluorescence signal. The density of vibrationally excited carbon monoxide can also be deduced by taking the difference between the two densities. There is no indication of gamma mode being observed in the TALIF measurements however, even though the same plasma source is being used. This is most likely due to the surface of the electrodes been changed from continued usage as they are no longer copper in colour but blackened due to overheating.

The small CO_2 admixture values in Figure 7.18 are high in comparison to the simulation values. Since the yield of carbon monoxide in this region is nearly 100% the TALIF values are clearly too high as they equate to far more than a yield of 100% of carbon monoxide. However the data points are well within error

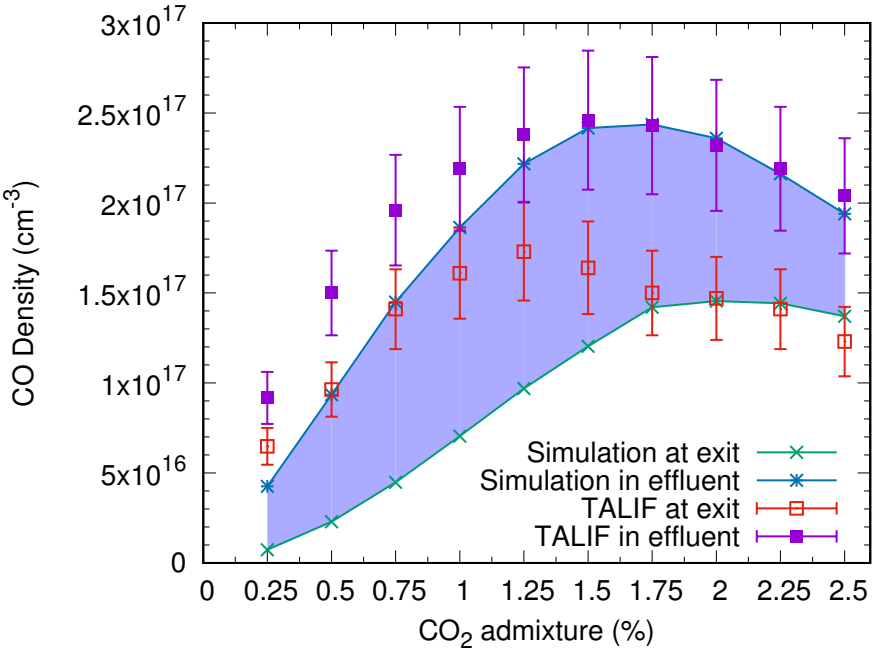

FIGURE 7.18: A comparison between the simulation densities in the effluent and at the exit of the plasma with the TALIF measurement at the exit of the plasma and in the effluent in an argon plasma with a plasma power of 30 W and 1 slm flow rate. There is very good agreement between the effluent measurements and the corresponding simulation densities. For low CO_2 admixtures the TALIF densities are too high and correspond to CO yields of far over 100%. This is due to the calculating the lifetime using quenching coefficients predicting a very short lifetime.

of measured values. The region for the overly high densities is most likely caused by the quenching coefficients used to calculate the lifetime of the excited state of carbon monoxide.

If the lifetimes in argon followed the same trend as for helium in Figure 7.17 then the lifetime for the small CO_2 admixtures would be higher and the measured densities lower. The lifetimes would also then follow the same trend as the atomic oxygen lifetimes. The lifetimes calculated for the argon cause are clearly dominated by the argon quenching rate as the lifetime is constant with CO_2 admixture. Therefore the quenching rate with argon is likely to be too high and causing larger measured densities. The iCCD should not have difficulty in measuring lifetimes of 0.5 ns and higher. The calculated lifetime is a realistic value as it is much smaller than what the iCCD can comfortably measure but it will increase the error in the measurement as there is an error associated with the quenching rates.

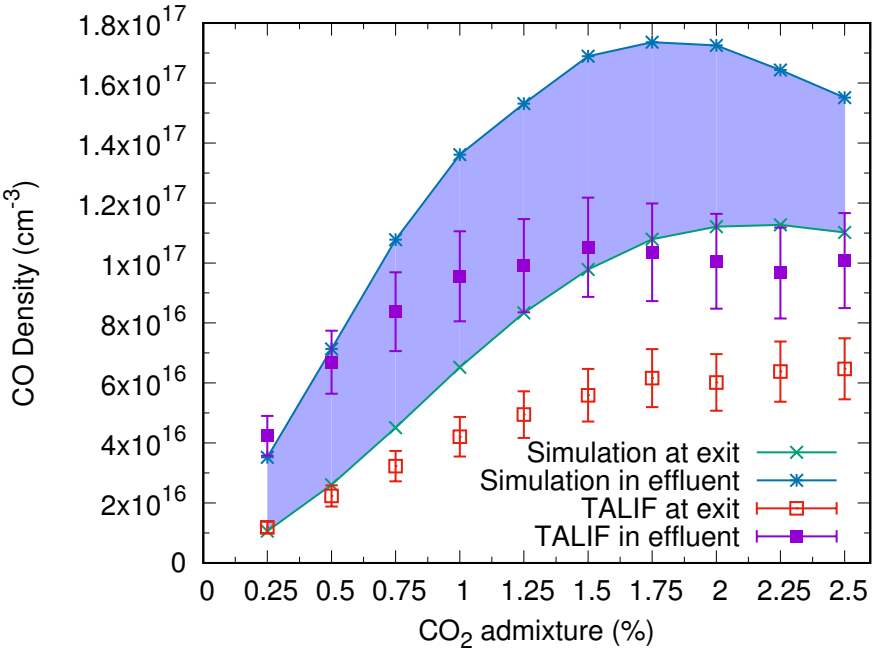

FIGURE 7.19: A comparison between the simulation densities in the effluent and at the exit of the plasma with the TALIF measurement at the exit of the plasma and in the effluent in a helium plasma with a plasma power of 30 W and 1 slm flow rate. The density is measured in the effluent is once again consistently higher than what was measured at the exit of the plasma. The agreement between the TALIF measurements and the simulation is about as good as for the FTIR and the simulation results.

Figure 7.19 shows the effluent measurements for the helium case. Once again the density measured in the far effluent is consistently higher than the those for the exit of the plasma. The agreement between the simulation and the model is once again not as substantive for helium as argon. However, the agreement for helium between the far effluent TALIF measurements and the FTIR measurements is similar. The observed trend does differ slightly to the trend in the FTIR measurements for the higher admixtures of CO_2. There is a much more clearly defined maximum in the TALIF measurements and since this occurs for the same CO_2 admixtures as where the gamma mode was observed in the argon FTIR measurements but not TALIF, it can be concluded that there is likely to be a lower electron density in the high CO_2 admixture conditions in the reactors current state as opposed to previously. This has implications in the utilisation of the plasma source as for certain admixtures the condition of the electrodes seems to be crucial for optimum performance.

7.5.2.1 Comparison Between TALIF and FTIR Densities

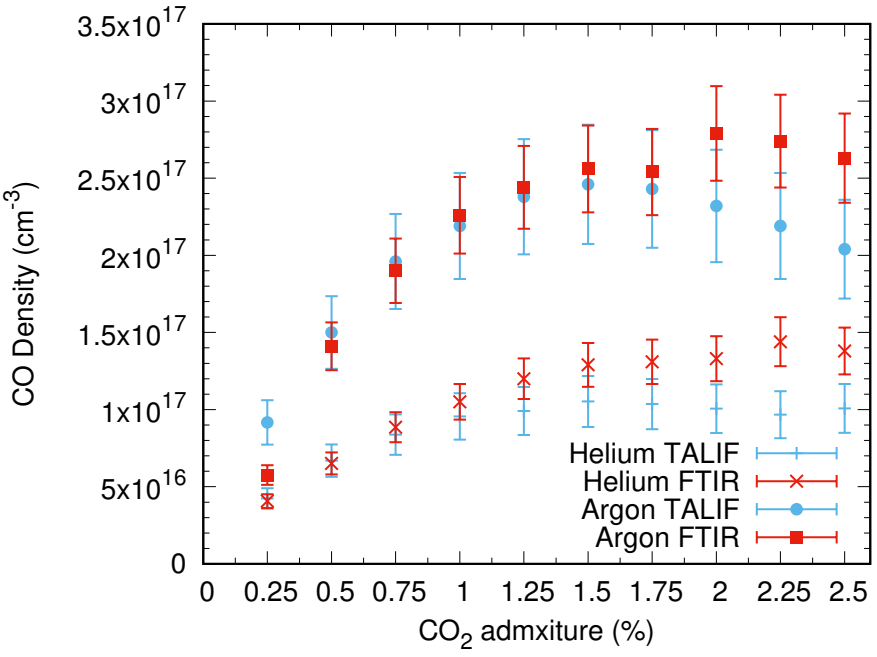

FIGURE 7.20: A comparison between the absolute ground state carbon monoxide densities measured using the FTIR and TALIF with respect to CO_2 admixture. The absolute densities measured using the FTIR are shown in red and TALIF in blue and the helium results are denoted using crosses and argon solid shapes. The absolute densities measured using the two different diagnostic techniques are in good agreement and almost all agree within the errorbars. The largest difference comes from the high CO_2 admixtures where gamma mode was observed in the FTIR measurements and not in TALIF.

The absolute ground state carbon monoxide density measurements using the two different diagnostics of FTIR and TALIF are shown in Figure 7.20 with respect to CO_2 admixture with both methods having a constant flow rate of 1 slm and plasma power of 30 W. There is very good agreement between the two diagnostic methods with the majority of the data points agreeing within error. The FTIR measures a higher carbon monoxide density than TALIF except in argon for the lowest CO_2 admixtures where the TALIF measurements predict a yield of over 100% and the causes were discussed in the previous section where the lifetimes of the excited carbon monoxide states were measured. The disagreement in the high CO_2 admixtures where gamma mode was observed for the FTIR measurements was also discussed in the previous section, where carbon monoxide densities were measured in the effluent using TALIF. TALIF also has an advantage over FTIR as a diagnostic as it can be employed locally and with spatial resolution.

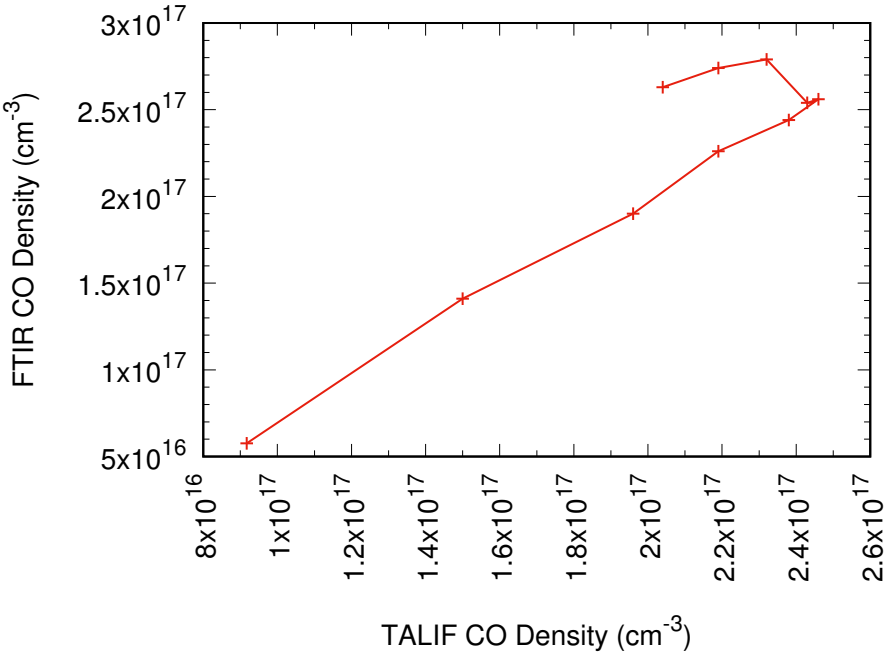

FIGURE 7.21: The carbon monoxide density measured using TALIF, in the far effluent, plotted against the same measurements using the FTIR. There is a linear trend observed between the two diagnostics measured, as expected as the different diagnostics methods should not depend on plasma parameters. The maximum in CO density also occurs for the same CO_2 admixture. However since gamma mode was not observed in the TALIF measurements in the effluent there is a discrepancy in the linear trend observed when the FTIR measurements showed signs of a gamma mode.

The good agreement between the absolute carbon monoxide densities means that there will also be good agreement between the yield and energy efficiency of the dissociation process since the specific energy input is the same for each diagnostic method. The good agreement between the two different diagnostic method also provide more validity to the two different methods and provides more confidence in the results presented as it is unlikely that both methods would be over or under-predicting the carbon monoxide density by the same amount. These results also show that, for alpha mode at least, the performance of the reactor is very consistent in yield at each time in use and can continue to produce high yields even after long periods of use. This is important information for the potential of an industrial use for this plasma.

Since both the FTIR and TALIF measurements in the far effluent are showing the same trend with respect to CO_2 admixture, they should show a linear trend with respect to each other as each diagnostic method should not depend on the plasma parameters. Figure 7.21 shows that there is a linear dependence between

the FTIR and TALIF measurements in the far effluent. At least for the majority of the measurements, there is a deviation from this trend for the FTIR measurements in gamma mode, which was not observed in the TALIF measurements in the far effluent. The maximum in CO density is also observed for the same CO_2 admixture in the alpha mode and so the remaining data points would be expected to follow the linear trend in the opposite direction, as observed for the 1.75% CO_2 admixture.

7.5.2.2 Vibrational Carbon Monoxide Density

Figure 7.22 shows the vibrational state densities of carbon monoxide deduced from the TALIF measurements. The vibrational states measured will consist of all those present in the effluent of the plasma but it is the lowest energy states that will be the most densely populated, although it is not possible to resolve these densities into individual vibrational states. This would, however, be possible in an FTIR with a small enough path length but would be very difficult to achieve at atmospheric pressure. Raman spectroscopy would be the best method to measure vibrational states of CO and CO_2.

There is not a clearly defined trend in the argon TALIF results due to the lifetime of the excited state being calculated instead of measured and this will add extra uncertainty to those measurements that becomes apparent when taking the difference between the two densities. However there is a clear trend in the helium measurements and a good agreement in trends and reasonable agreement in density between TALIF and the simulations. The vibrational state density is usually higher in argon compared to helium, which is expected as not only is the carbon monoxide density higher the electron density and temperature are also predicted to be higher by the model and these factors would lead to an increase in vibrational excitation. The density of the vibrational states are shown to be between 40-50% of the total carbon monoxide density.

There is more of a trend in the helium vibrational state densities which differs slightly from the trend observed in the ground state density. The maximum in the vibrational state density in helium is observed for a CO_2 admixture of 1% whilst the maximum ground state density is for a 1.5% admixture according to the TALIF measurements. This difference in maximum densities can be explained by considering the quenching of the vibrational states. As observed in the lifetime measurements increasing the CO_2 admixture in helium increases the quenching

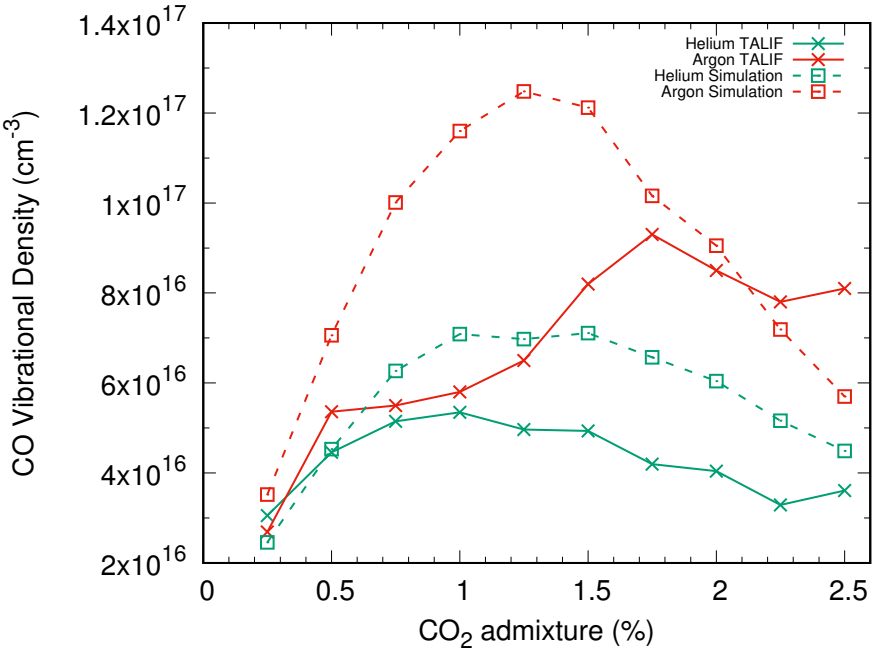

FIGURE 7.22: By finding the difference between the ground state densities in the far effluent and just at the exit of the plasma it is possible to determine the vibrationally excited densities of carbon monoxide for both the TALIF measurements and the simulation. The majority of this density will be populated with very low energy states and will demonstrate the amount of electron energy that is 'wasted' at the end of the plasma when the carbon monoxide density is at its highest. The vibrational carbon monoxide density is higher in the simulations compared to the experiment due to either uncertainties in the vibrational excitation reaction cross sections or the quenching rates.

of the electronically excited carbon monoxide state and appears to also increase the quenching of the vibrational energy states and supports the pathway analysis results of a two step dissociation process as whilst the vibrational densities are quite high there is also clearly a high level of quenching.

7.5.3 Flow Variation

Now that the absolute ground state density can be accurately measured through TALIF, measuring the absolute density of CO with respect to the total flow rate of the plasma and comparing the trend to that of atomic oxygen will provide the best insight into whether it seems that atomic oxygen is being recycled to produce more carbon monoxide and oxygen.

7.5.3.1 Argon

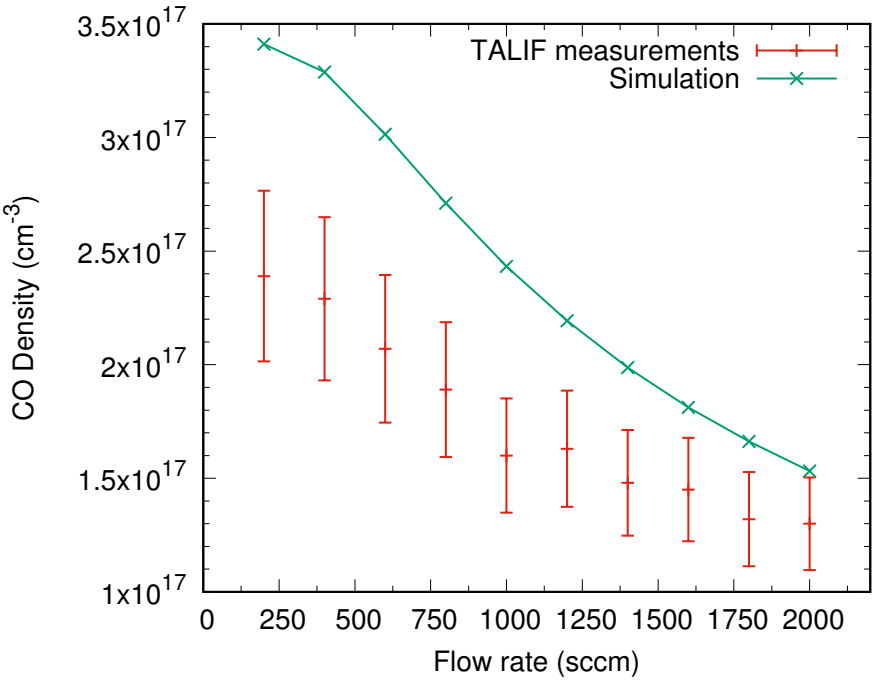

FIGURE 7.23: The absolute carbon monoxide density as a function of the total flow rate of the gas with a constant CO_2 admixture of 1.5% and plasma power of 30 W in argon. The overall trend in the carbon monoxide density is similar between the TALIF measurements and the simulations under the same conditions with an increased residence time from the decreased flow rate increasing the carbon monoxide density. This is opposite to the trend observed in atomic oxygen which suggests that atomic oxygen is being used to produce more carbon monoxide.

The absolute carbon monoxide densities measured in the far effluent of the plasma using TALIF in an argon carrier gas with respect to the total flow rate of the gas are shown in Figure 7.23. The measurements were performed using a constant CO_2 admixture of 1.5% and plasma power of 30 W, the same as those used for the atomic oxygen flow variation. The overall trend of the carbon monoxide density is similar to that of the simulation with the absolute densities agreeing within error. However the predicted yield is much higher in the simulation for the lowest flows but the agreement improves as the flow rate is increased.

The trend in carbon monoxide density is the exact opposite of the one observed for the atomic oxygen density where the density would decrease with decreasing flow. This strongly suggests that atomic oxygen is reacting with excited CO_2 to produce more CO. As the residence time increases the amount of sufficiently excited CO_2 and also the rate of the recycling reaction increases and the

carbon monoxide density increases. The main loss channels of carbon monoxide is the reverse reaction to CO_2 but the atomic oxygen density has been shown to decrease and so the CO losses do not significantly increase. If there was a simple splitting of CO_2 the same trend would be expected between carbon monoxide and atomic oxygen densities but the observed trends are those expected from the pathway analysis work.

7.5.3.2 Helium

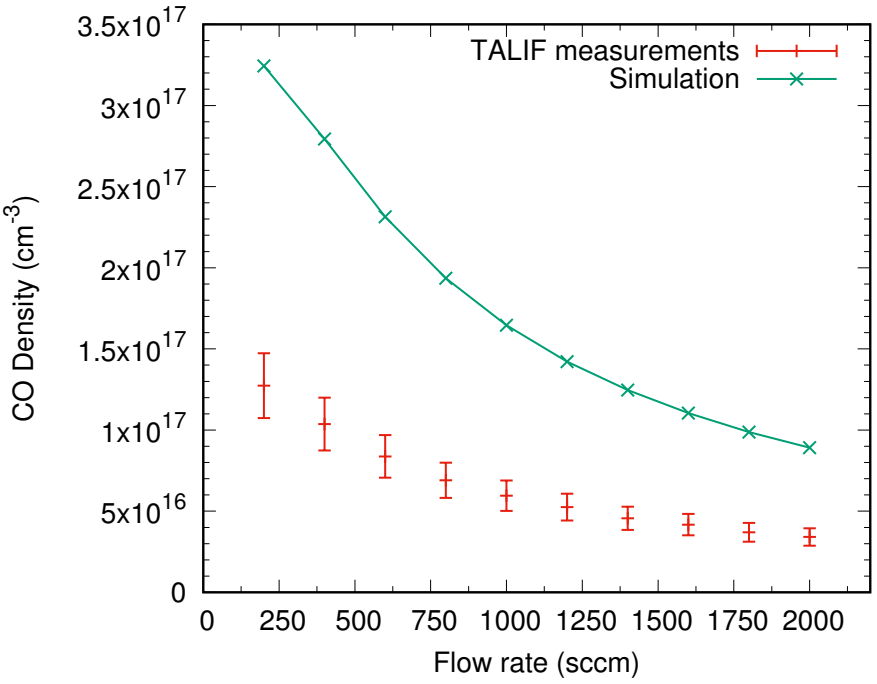

FIGURE 7.24: The absolute carbon monoxide density as a function of the total flow rate of the gas with a constant CO_2 admixture of 1.5% and a plasma power of 30 W in helium. The model predicts a far more sharply increasing density with reducing total flow and always predicts a higher carbon monoxide density, as have all of the helium simulations. There is also a maximum density obtained in the helium carrier gas with the density remaining 1.5 X 10^{17} cm^{-3} for both 200 and 400 sccm.

Figure 7.24 shows the carbon monoxide density as a function of flow rate for the helium carrier gas. The agreement between the model and the experiment is not as good for the helium case and although the general trend is similar there are a few points of difference. As with the argon case as the residence time increases the carbon monoxide density increases which is once again the opposite trend to the atomic oxygen density and so helium, like argon, appears to show that atomic oxygen is used to produce carbon monoxide in the plasma.

There is a maximum carbon monoxide density, and therefore conversion, observed in the helium case. For both the 200 and 400 sccm total flow rate points the carbon monoxide density peaks at 1.5 X 10^{17} cm^{-3} which is only a yield of 40.89 %. Higher yields have been presented in this work with smaller CO_2 admixtures in helium and so this only appears to be a limit for this particular admixture. Since the model doesn't show the same limit, and has always been more inaccurate than the argon model, there is clearly still more to be understood in how helium interacts with the admixture in these plasmas.

A possible explanation for this limit can be found in the electron energy loss fractions shown in the previous chapter. Since a significant amount of electron energy is lost through collisions with the carrier gas and as more CO_2 is converted more electron energy is lost into excited states of carbon monoxide and therefore it is possible that very little electron energy is being deposited into CO_2 dissociation channels, and Figure 7.25 supports this.

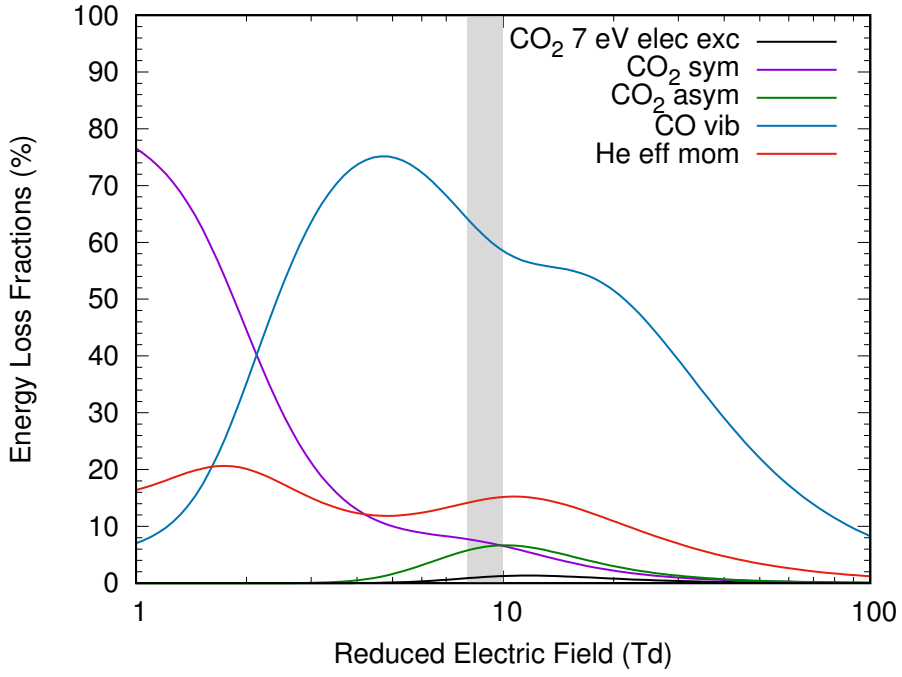

FIGURE 7.25: The electron energy loss fractions in a helium CO_2 plasma with a 40% conversion into CO as seen in the 200 and 400 sccm flow rates. For the reduced electric field range seen in these plasmas approximately 90% of the electron energy is being deposited into non-dissociative electron energy loss channels.

Approximately 90% of the electron energy is being deposited into channels that do not lead to dissociation, most of the energy is being lost to CO excitations but there is still a significant amount lost to effective momentum transfer with

the carrier gas and symmetric stretches of CO_2. The gas fractions put into the Bolsig+ calculations are those of the conditions measured in the far effluent of the 400 sccm total flow rate condition presented in this section and therefore it shows that even though the residence time is doubled for the 200 sccm case most of the electron energy will not possibly lead to dissociation. However since some energy is still going into dissociative channels it does not explain why no increase is conversion is seen. The simulation is not showing this effect because of the lack of excited carbon monoxide states included for simplicity and ease of determining conversion rates. Including a full set of vibrational states should improve the agreement between the experiments and simulation.

7.5.3.3 Lifetime

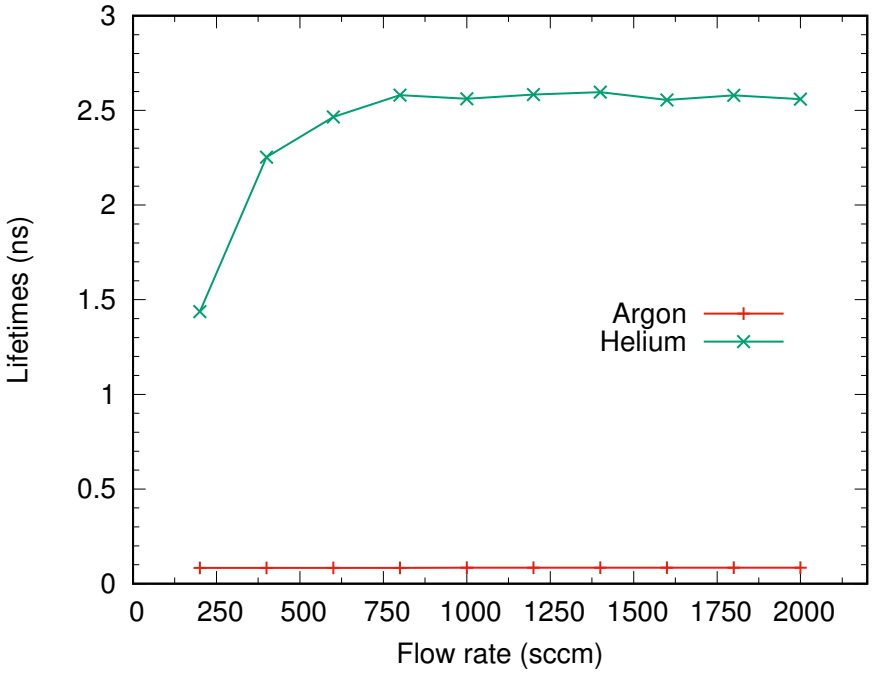

FIGURE 7.26: The lifetimes of the excited state of carbon monoxide in both argon and helium carrier gases. Again the argon lifetimes are calculated from quenching rates and there is little difference with flow rate. For helium the lifetime reduces as the flow rate reduces as self quenching has a substantial effect on the lifetime.

Figure 7.26 shows the lifetime of the excited state of carbon monoxide for the flow rate variations. As the argon case lifetimes are again calculated from the quenching coefficients the lifetime is remaining constant for all conditions which will lead to some uncertainty in the measured densities. For the helium case

the lifetime reduces with decreasing flow rate. This is due to the increased self quenching as the conversion increases with the increased residence time. Since the admixture remains constant the carrier gas density is also constant and it is only the contents of the admixture that changes. Therefore the reduction in lifetime must be due to self-quenching, or O_2, as the CO_2 density reduces with admixture. Looking at the quenching coefficients for CO, [143], both O_2 and CO should be effective at quenching the state as the quenching rate for O_2 is approximately twice that of self quenching but the density is approximately half due to molecular oxygen forming for roughly every two CO_2 dissociation reactions. Since a large difference in lifetime is observed for the 200 and 400 sccm measurements it seems unlikely that the conversion is the same for each case as if the conversion is the same the gas mixture should be the same and the measured lifetime should be the same since the measurement was performed in the far effluent where the temperature should be the same for all measurements.

7.5.3.4 Comparison to the FTIR Measurements

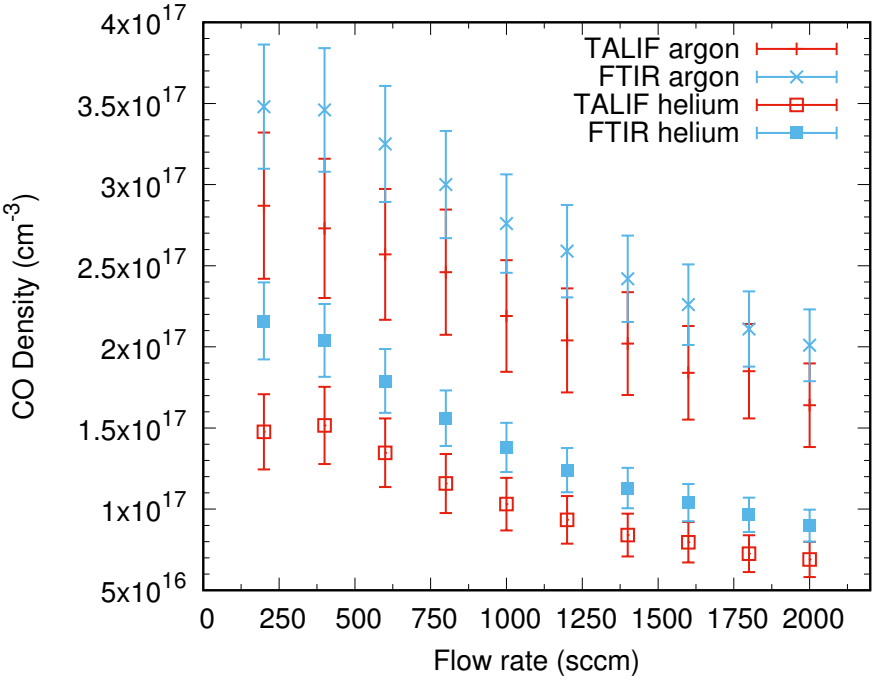

FIGURE 7.27: A Comparison of the Absolute Densities of Carbon Monoxide Measured Using TALIF and FTIR as a Function of Flow. The FTIR measurements are shown in blue and the TALIF measurements in red with the argon carrier gas results shown using crosses and the helium, squares. The agreement is once again very good with most data points agreeing within error with the FTIR always yielding a higher absolute density.

The absolute ground state densities measured using TALIF and FTIR spectroscopy are shown in Figure 7.27. Once again there is very good agreement between the measured densities using the two different diagnostics with most the data points agreeing within their respective errors. The densities measured using FTIR spectroscopy are also consistently higher than the TALIF measurements as well as having a smaller error associated with them. Therefore FTIR spectroscopy appears to be a better diagnostic method for measuring ground state CO densities but TALIF has many other advantages such as the ability to measure short lived atomic species and the potential to spatially resolve the absolute densities by moving the laser beam with respect to the exit of the plasma [77].

The maximum yield observed in the helium TALIF measurements was not observed in the FTIR measurement and this could be due to the measured lifetime as stated earlier but the flow controller used for the FTIR measurements also had a minimum flow rate of 200 sccm and so can be considered the least accurate data point for the FTIR measurements whilst the minimum flow on the flow controller used for the TALIF measurements was 100 sccm and as such the CO_2 admixture in the FTIR experiments was likely slightly below 1.5%.

Through the complementary nature of experimental and computational work the radio frequency atmospheric pressure plasma for the conversion of CO_2 has been well characterised and understood with operating regimes discovered to provide a high range of yields with very good energy efficiencies for the yields obtained. However, in order for these plasmas to be successfully implemented on an industrial scale the ease of utilisation must also be investigated.

Chapter 8

Utilising the Carbon Monoxide

Whilst the focus of this work has currently been on converting CO_2 to produce CO and optimise the system, this is only the first step on the way to producing an industrial technology. Whilst optimising the yield and energy efficiency are vital for showing the potential of plasma reactors for the conversion of CO_2 it is equally vital to show that the carbon monoxide produced is able to be utilised effectively to give the desired results. This can be achieved either through the direct utilisation of CO or by attempting to separate the gases [150].

In order to test how effectively the carbon monoxide produced can be utilised it is necessary to test the technology on a chemical application. For the most energetically efficient plasma reactors, such as microwave plasmas, the aim is to produce carbon neutral fuels through combining the carbon monoxide with hydrogen to produce syngas. For the plasma reactor shown in this work the high yields obtained with low energy efficiencies compared to the microwave plasmas shows these plasmas to be more useful as a greener source of carbon monoxide than dry reforming of methane.

Since the plasma runs in atmospheric pressure and standard temperatures a chemical application that requires carbon monoxide and also runs in these conditions is a perfect test for utilising the carbon monoxide as the effluent can simply be run through the reaction vessel. Although the effluent is mostly comprised of the carrier gas, which will be argon for the chemical applications due to the high yields of CO obtained and the sustainability of the argon compared to helium, the carrier gas is inert and should not interfere with the reactions.

8.1 Using the Carbon Monoxide for Chemical Synthesis

The reaction of choice used to test the usability of the carbon monoxide is the hydroxycarbonylation of aryl halides into aromatic acids, which is simple to operate and reacts in ambient conditions [151]. The reaction the carbon monoxide has been used for is shown in Figure 8.1. This reaction has been shown to produce high yields of product, up to 90%, with high selectivities using a palladium catalyst. Therefore if the carbon monoxide from the plasma effluent can replicate the high yields of product the plasma reactor could be used as a method of turning waste CO_2 into a valuable product. Aromatic acids such as the one produced in this reaction are useful in pharmaceuticals and agrochemicals.

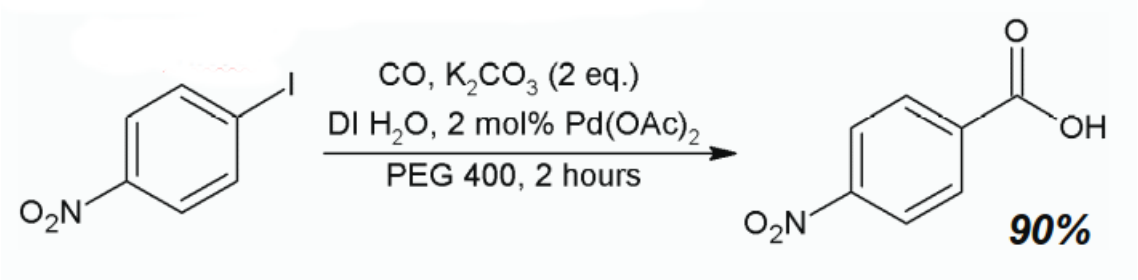

FIGURE 8.1: The reaction being used to test the usability of the carbon monoxide as described in [151]. The reaction being used is the hydroxycarbonylation of aryl halides into aromatic acids and has been shown to produce high yields with high selectivities under ambient conditions.

The conditions used to produce the carbon monoxide used were selected to produce high yields of carbon monoxide whilst also trying to have the highest concentration of carbon monoxide in the effluent and therefore a 1% CO_2 admixture was used in a total flow of 0.5 slm with an argon carrier gas and a plasma power of 30 W. The yield of carbon monoxide is over 90% with the effluent containing 2.26 X 10^{17} cm^{-3}. The effluent was bubbled into the reaction mixture for 4 hours in accordance with the experimental procedure in the literature and the reaction mixture was analysed using nuclear magnetic resonance (NMR) to measure the yield of product.

The first results of trying to utilise the carbon monoxide where far from ideal with 0% conversion achieved and the literature results where repeated with pure carbon monoxide from a bottle. This was due to the ozone produced by the plasma reacting with the palladium catalyst and preventing it from catalysing the

Reaction time (hours)	Concentration of Catalyst (mole %)	Product (%)
2	2	4
2	10	12
2	20	10
4	10	11

TABLE 8.1: The percentage of product produced from the carbon monoxide produced by the plasma with respect to the concentration of the palladium catalyst and the time allowed for the reaction. Increasing the concentration of the catalyst provides some improvement in yield but not indefinitely. Increasing the reaction time also does not provide any improvement in the yield and therefore it appears that the catalyst is still being compromised.

reaction and therefore the reaction would not occur under ambient conditions. Whilst stopping the plasma from producing ozone is very difficult removing ozone from the effluent is not. There are catalytic ozone scrubbers in production that are possible to add the gas lines after the plasma and before the reaction mixture to remove the ozone from the effluent. The effectiveness of the scrubber was tested using the FTIR and it was observed to remove the ozone peaks from the infra-red signal without having an impact in the carbon monoxide density.

Having removed the ozone from the plasma effluent and by using a less viscous version of the reaction solvent to allow the effluent to better defuse into the reaction mixture the plasma created carbon monoxide was able to produce 4% of the desired product, far from the desired 90% but an improvement. By increasing the concentration of the palladium catalyst in the reaction mixture the conversion was increased to 12% as shown in Table 8.1 with only two hours of bubbling time but by doubling both the reaction time and the concentration of the catalyst no improvement in the yield was seen. This suggests that the catalyst is being compromised by something else in the effluent.

Since the ozone has been removed from the scrubber and argon is inert the only main products left that could be affecting the reaction are the unreacted CO_2 and the O_2 produced. The reaction in question is strongly alkaline and CO_2 reacting with water to form carbonic acid is well known. Water is present in the reaction mixture for the formation of aromatic acids and the formation of carbonic acid would change the pH of the reaction significantly enough to prevent high yields of aromatic acids. Figure 8.2 shows the pH of the reaction mixture for pure CO from a bottle and plasma produced CO with respect to the reaction time. It is clear that a significant amount of acid is being produced by the unreacted

CO_2 in the plasma produced carbon monoxide and this is preventing the same yields of aromatic acids being formed.

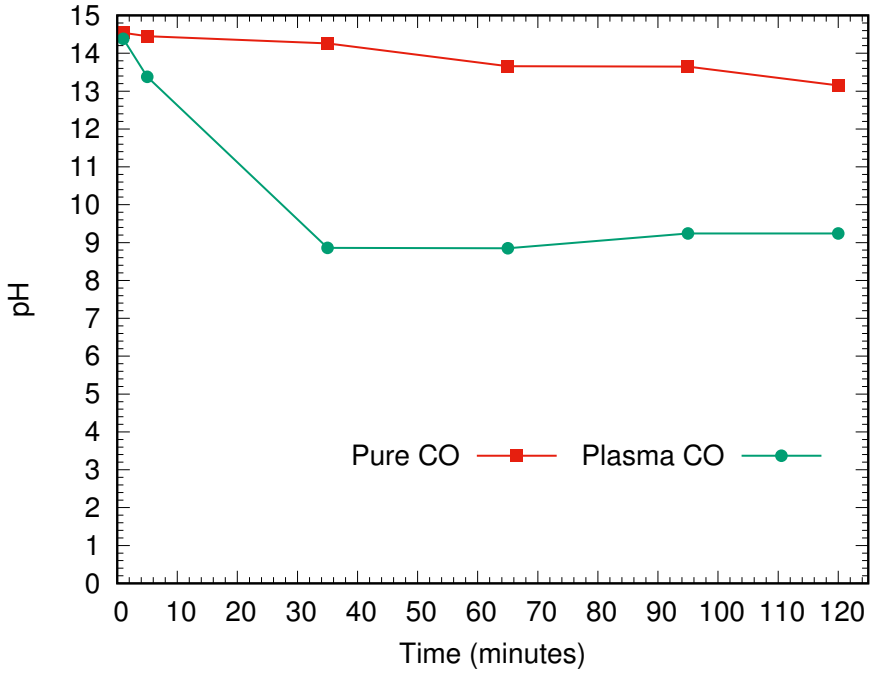

FIGURE 8.2: By monitoring the pH of the hydroxycarbonylation of aryl halides into aromatic acids for both pure CO from a bottle and plasma produced CO it is clear that an acid is being produced during the plasma produced CO experiments and this is having a significant effect on the yield of aromatic acids. The acid being produced is carbonic acid from the unreacted CO_2 and water in the reaction mixture and further experiments showed that even for conditions were the CO_2 conversion was close to 100% enough would reach the aryl halides to affect the yield of aromatic acids.

A lime water trap was added to the gas lines to trap the unreacted CO_2 and smaller CO_2 admixtures of 0.5% were used to try and limit the amount of CO_2 reaching the reaction mixture but no significant increase was seen in the yield of aromatic acids. Whilst the yields achieved using the plasma produced carbon monoxide were low and far from those of pure carbon monoxide some yield was observed. Therefore the problems with utilising the carbon monoxide are largely down to issues with separating the product, CO, from the reactant CO_2 which only highlights the need to consider how the carbon monoxide can be used once produced. Another method to utilise the carbon monoxide that was considered was to selectively remove the carbon monoxide from the effluent and store it for future use.

8.2 Storing the Carbon Monoxide for Future Utilisation

Carbon monoxide is known to be soluble in polar aprotic solvents such as dimethyl sulfoxide (DMSO) and dimethyl formamide (DMF). A polar aprotic solvent is one that will dissolve many salts but does not possess an acidic hydrogen atom. However DMF is thought to be carcinogenic and so is not a suitable and DMSO can irritate the skin and therefore propylene carbonate has also been considered as a solvent into which the carbon monoxide can be dissolved for later use and thus remove the problem of unreacted CO_2.

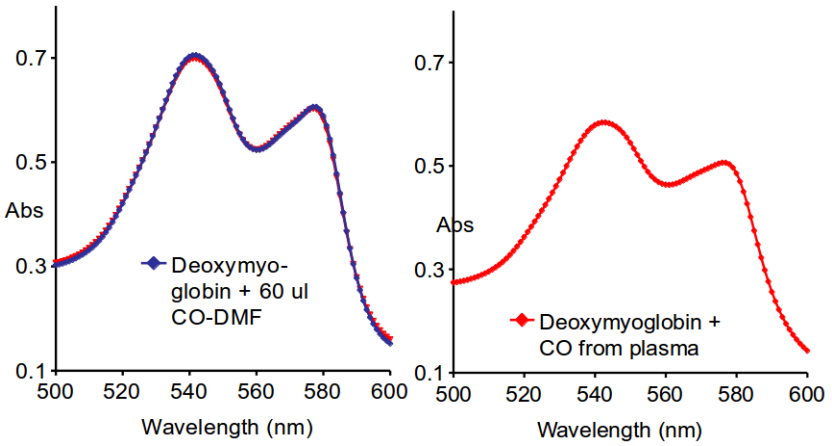

FIGURE 8.3: The saturation of dimethyl formamide with carbon monoxide from the plasma and pure carbon monoxide. The plasma produced carbon monoxide is not saturated due to the presence of ozone in the effluent which can easily be removed using a scrubber.

Figure 8.3 shows the attempts to saturate the solvent DMF with carbon monoxide. The plasma produced carbon monoxide is shown to not have saturated the solvent due to the presence of ozone in the effluent which can easily be removed with an ozone scrubber. The plasma used to try and saturate the DMF was a 1% CO_2 admixture in a helium plasma with a plasma power of 30 W. There is evidence though that CO is stored in the DMF allowing for temporary reversible storage. This allows for the plasma produced CO to be transported and used in different reactions, allowing the utilisation of plasma produced CO. Trapping of CO into polar aprotic solvents is one potential method of separating CO from the other exhaust gases but more work is needed to demonstrate the capability of this method on a large scale.

Chapter 9

Conclusion

The aim of this work was to investigate the effectiveness of an atmospheric pressure radio frequency plasma reactor for the conversion of waste carbon dioxide into carbon monoxide, a valuable chemical feedstock. Many different plasma sources have been studied for the conversion of CO_2 with varying degrees of success, some efficient and some able to achieve high yields, but there has always been a trade-off between the yield and energy efficiency. Radio-frequency atmospheric pressure plasmas are of interest due to their low cost of running and ability to be easily scaled to commercially viable industrial levels.

The plasma reactor design used differs slightly to the standard radio-frequency atmospheric pressure design [77, 78] with an electrode gap of only 0.5 mm. This was to allow easy use of argon as a carrier gas and also compare argon and helium as carrier gases for producing desired species in a plasma. The driving frequency used was also different from the standard for this type of plasma. 40.68 MHz was used due to the higher electron densities and plasma powers that could be obtained with high driving frequencies.

The plasma reactor was immediately shown to be highly capable of converting CO_2 into CO with high selectivity, achieving conversions of nearly 100% for CO_2 admixtures below 1% with plasma powers of 30 W. However as with all the other plasma sources this high conversion came with low energy efficiencies with the highest yield having a conversion efficiency of only 4.52%. The best results were always shown to be in argon due to the higher conversion in an argon carrier gas with the same specific energy inputs per molecule of CO_2 used when only changing the carrier gas. The conversion in helium was often found to be only about half

what could be achieved in argon and the reasons behind this formed a large part of this study.

In comparison to other plasma reactors for converting CO_2 the source used in this study has much higher specific energy inputs per molecule of CO_2. This is because many other plasma reactors have focused on plasmas that can operate in pure CO_2 and the plasma in this study has small admixtures of CO_2 in a carrier gas, greatly reducing the density of CO_2 molecules in the plasma even when compared to plasma reactors operating below atmospheric pressure. This causes low energy efficiencies but the operating power is much lower than other plasma sources requiring only tens of Watts instead of hundreds or even thousands. Whilst these plasmas are not suited for producing carbon neutral fuel from a CO_2 emitting energy source. Due to their high yields and ease of use they are ideally suited for running when surpluses of renewable energy sources are in the grid, as a result of high levels of wind or sun on a particular day. Running these plasmas off solely renewable energy sources would result in a net reduction in CO_2 levels, or at least net zero.

This study has shown that the yield of carbon monoxide drops with increasing CO_2 admixture up to the maximum admixture studied of 2.5% and this trend is expected to continue until it is no longer possible to ignite a plasma. The corresponding energy efficiency however, does not show the same trend and reaches a maximum at 1.5% in alpha mode for argon, 2% in gamma mode, and 2.25% in helium. The energy efficiency trend was shown to match that of the absolute carbon monoxide density with the maximum energy efficiency corresponding to the maximum carbon monoxide density. The most energetically efficient CO_2 admixture also contains the highest density of carbon monoxide but does not correspond to the most CO_2 converted.

A global model, Global_Kin was used to simulate the gas kinetics of the plasma and was shown to correlate with the experimental results. It can therefore be used to provide insight of the plasma that either cannot or was not measured experimentally. The model showed that both the electron temperature and density for both argon and helium decrease with increasing CO_2 admixture. The electrons eventually becoming to few and/or too cold to produce more carbon monoxide; thus the density of carbon monoxide decreases. This result is important as it can be used to tailor the plasma to produce the most effective plasma for the application.

For instance the electron temperature and density can be influenced by using non-sinusoidal tailored waveforms which then increase the yield and energy efficiency further and the increased electron density in gamma mode results in the increased carbon monoxide densities observed.

The electron temperature and density were also shown to be higher in argon than helium and this goes part of the way to explaining the higher conversion seen in the majority argon plasmas. The electron energy distribution functions were also shown to be more favourable for CO_2 conversion in argon than helium. Since the bond energy of CO_2 is 5.5 eV and the energy required for direct electron impact dissociation is over 7 eV, having a higher density of electrons in this energy range leads to a greater chance of electrons dissociating CO_2 and therefore the distribution of electron energies were shown to be better in argon than helium.

Looking at the electron energy loss fractions for the same reduced electric field values as observed in the global model show that a large reason for the difference in yield and therefore energy efficiency between argon and helium is due to only a small percentage of the electron energy being lost to momentum exchanges with argon, whilst nearly a quarter of the electron energy is lost in momentum exchanges with helium. This difference in energy losses is due to the Ramsauer minimum which means that electrons can essentially pass through argon atoms whilst they will collide with helium and therefore less of the electron energy will go into desirable channels that dissociate CO_2.

Observing the electron energy losses in the plasma with an admixture comprised of what is expected at the end of the plasma rather than the start also showed that a significant amount of the electron energy is lost in collisions with carbon monoxide. Therefore as the plasma evolves less, and less of the electron energy is deposited in desirable channels and more is wasted in other excitation processes. Increasing the flow rate decreases the electron energy losses to the products and leads to an increase in energy efficiency until the yield becomes so low that it negates the lower specific energy input.

The global model was also used to observe how the densities of the plasma species change throughout the plasma and the species densities where shown to not be in equilibrium at the exit of the plasma. Therefore a variation of the flow rate was performed to ascertain whether the conversion would be increased with increased residence time and to see if the energy efficiency would increase. A

1.5% CO_2 admixture was used for this variation as it provided the highest energy efficiency in alpha mode. The model was shown to correlate once again with the experimental results; the yields of carbon monoxide increasing with decreasing flow rate and the energy efficiency increasing with increasing flow rate (due to the loss in yield being outweighed by the reduction in specific energy input per molecule of CO_2). A new maximum energy efficiency of 9% was achieved for a yield of over 50%. Whilst this energy efficiency is still too low to produce fuels with a net reduction in CO_2 it does show that radio-frequency plasmas can achieve efficiencies equivalent to those of DBD plasmas with higher conversions.

Pathway analysis of the chemical reactions was also performed on the global model results to provide insight into how the carbon monoxide is produced and ascertain whether improvements can be made. The pathway analysis shows that the carbon monoxide produced was produced in the desirable and energetically efficient manner and the low energy efficiencies are only a result of the low partial pressures of CO_2 in these plasmas. It also illustrates that a two step process was observed for the dissociation of CO_2 with electrons exciting the carbon dioxide molecule close to the dissociation limit and then collisions with either the carrier gas or the atomic oxygen produced from dissociation to complete the dissociation. Direct electron impact dissociation was also shown to be important but not to the same extent as the two step dissociation.

Vibrational up-pumping was not observed in these plasmas which is not unexpected due to the highly collisional nature of atmospheric pressure plasmas and the low gas temperatures meaning that only single quantum transitions will occur during vibrational energy exchange. Due to the singe quantum transitions the highest energy levels that lead to dissociation were not populated through up-pumping as the vibrational state was more likely to collide with the carrier gas or atomic oxygen than vibrationally excited CO_2 due to the large difference in densities and therefore reaction rates.

The backward reaction of carbon monoxide and atomic oxygen was also seen to be very low in rate and therefore the carbon monoxide produced remains very stable in the plasma and the plasma effluent. This result was expected as the FTIR measurements were performed in the far effluent and where showing very high yields of CO for small CO_2 admixtures. However as the species in the admixture evolve throughout the plasma more ozone starts to be produced through the three body recombination of atomic oxygen and molecular oxygen which is an

undesirable reaction that reduces the amount of atomic oxygen that can be used to produce more carbon monoxide.

However the accuracy of the pathway analysis depends entirely on the accuracy of the reaction rate coefficients, which are notorious for inaccuracy and changing by orders of magnitude depending on the study. Therefore the results of the pathway analysis could change considerably with different reaction rates or even within the error of the reaction rates used. Since the dissociation of CO_2 was found to be a two step process, the first step been electron impact vibrational excitation, the error in the reaction rate for the first step also has a big impact on the results of the model. The reaction rates for the electron impact vibrational excitation of CO_2 are calculated from cross-section data depending on the electron energy distribution function. Therefore the cross-sections used would also have a large impact on the results of the model. The cross-sections for almost all of these processes are approximated using the Fridman approximation, and therefore there is already a large uncertainty included in these rates and the accuracy of the approximated rates depends not only on the accuracy and validity of the approximation used but also of the cross-section used from which to calculate the approximations.

There are also many approximations used in the changing of the activation energy of the reaction rates in accordance with the vibrational energy of the CO_2 vibrational state in the reaction. The activation energy of the reaction and the amount the activation energy is lowered by the vibrationally excited CO_2 molecule have the affect of determining which asymmetric states of CO_2 will dissociate. In this work it was found that only asymmetric states with an energy over 4.5 eV would dissociate through the two main dissociation reactions, however this depends entirely upon the approximations used in lower the activation energy and the activation energies in the rate coefficient. Changing either of these would change which CO_2 states dissociate and therefore would affect the yield of CO and the pathway analysis. Therefore the pathway analysis results hinge on trying to accurately reflect the plasma chemistry through the assumptions used and must be validated to experimental data in order to have any relevance.

TALIF measurements were performed to measure both the atomic oxygen and carbon monoxide densities for the first time on a plasma of this type. The atomic oxygen density was found to be orders of magnitude lower than the carbon monoxide density which would not be the case if there was a simple dissociation

of CO_2 into CO and O. The trends observed in the densities of atomic oxygen and carbon monoxide for a flow variation where shown to be opposite to one another. Therefore this appears to support the pathway analysis results of atomic oxygen being used to react with CO_2 to produce more CO, which is a highly desirable result for efficient conversion of CO_2. The experiment however, only provides a qualitative view of the atomic oxygen dynamics and does not conclusively show the recycling of atomic oxygen as predicted by the pathway analysis. More in-depth experiments would be required to show that this is occurring more conclusively and these are discussed in the next section.

TALIF measurements performed on carbon monoxide were also shown to be able to give a value for the vibrational state density of carbon monoxide by measuring at the exit of the plasma and the far effluent. It would also be of interest and possible to measure the increase in carbon monoxide density as a function of distance into the effluent and measure the rate of decay of the vibrational states of carbon monoxide and potentially other molecular species that can be detected using TALIF. The TALIF measurements were also shown to agree well with the FTIR measurements adding validity to both diagnostic techniques and the yields reported in this study.

Finally the carbon monoxide was utilised to demonstrate both the ability of the plasma to produce usable CO and the difficulty of separating the carbon monoxide from the other plasma species. Both unreacted CO_2 and ozone were found to cause problems for the ability to utilise the carbon monoxide produced. The ozone produced could be easily removed with a catalytic scrubber but the CO_2 proved to be more difficult to handle. The carbon monoxide produced by a plasma was shown to be usable but with far less effect than pure carbon monoxide. However it was also shown that it is possible to dissolve the carbon monoxide in a solvent to remove it selectively from the effluent. However, more investigation is needed into how to utilise effectively the carbon monoxide produce by a plasma.

This work has shown that radio-frequency atmospheric pressure plasmas can convert CO_2 with very high yields and high energy efficiencies for the corresponding yields. However the energy efficiencies are still low in comparison to other types of plasma reactors such as microwave plasmas. The argon CO_2 plasmas were shown to put electron energy into the desirable channels for efficient dissociation thereby allowing these plasmas to perform better than others of that achieve the same yields. In order to convert CO_2 the most efficiently through plasmas is by

means of a plasma reactor designed to operate in high CO_2 densities, to keep the specific energy inputs low, and have a reduced electric field value that will lead to a high proportion of the electron energy being deposited in the desirable channels. More work however needs to be done on how to use the carbon monoxide once it is produced in order for plasma produced carbon monoxide to become viable in a commercially viable industrial setting.

9.1 Outlook and Future Studies

The Phelps cross section set [115] was used for this study and the reasons behind this were discussed in chapter 6. However since this cross section set made the basis for all of the approximations used to determine the electron impact vibrational excitation reactions, which are vital to the dissociation of CO_2, a large amount of the uncertainty in the model comes from this reaction set. Although the 7 eV electronic excitation of CO_2 was shown to be a good approximation for direct electron impact dissociation, the pathway analysis shows that asymmetric vibrational excitation is much more important to the overall conversion process. Therefore determining the best cross section database for asymmetric vibrational excitation of CO_2 should provide the most accurate dissociation reactions overall. Therefore it is important to use other cross section databases for CO_2 in the model and apply the Fridman approximation again to determine which database would provide the most accurate results for these plasmas and how much variance there is between the different databases.

In order to validate the recycling of atomic oxygen, which was shown to be important in the pathway analysis of the model, more in-depth TALIF experiments are required. It is possible with TALIF to get highly spatially resolved measurements due to the small beam width of the laser. It would therefore be possible to provide a small increase in atomic oxygen density at a point in the plasma, either through a small increase in plasma power for a finite amount of time or the a brief addition of more oxygen into the plasma admixture. Since the addition of more atomic oxygen would only be for a finite amount of time the atomic oxygen density would soon decay and return to the same density as before the addition. It would be possible to measure the decay of the atomic oxygen density over time. By considering the particle balance of atomic oxygen in steady state and the main

production and destruction reactions from the pathway analysis it would be possible to get a more in-depth picture of the reaction dynamics of atomic oxygen. This would be done by comparing the trend seen in the decay of atomic oxygen to what would be expected from a particle balance equation for atomic oxygen using the main production and destruction reactions from the pathway analysis.

This kind of experiment could also be performed for carbon monoxide. The addition of carbon monoxide to the plasma would be much easier than the addition of atomic oxygen due to carbon monoxide been available in bottles and therefore could easily be added to the plasma admixture and the pathway analysis has shown CO to be very stable in these plasmas due to the high bond energy of the molecule. By adding a small amount of CO over a small finite time, as with the atomic oxygen case, again the decay of the CO density could be measured using TALIF. Since CO is shown to be stable in the plasma it would be expected that the decay in density would come mostly from the diffusion of the added gas out of the laser profile. But this would also occur in the atomic oxygen case and it is important to understand the timescale over which this occurs.

These dynamic experiments could also be performed in the model. It is possible in the global model to introduce small finite spikes in power at a certain time in the simulation as well the introduction of new species to the admixture at a certain time. Therefore the decay of the species of interest could also be observed in the model and compared to the TALIF experiments to be used as a further point of validation of the model to determine if atomic oxygen is indeed been recycled. If the decay trends observed are the same between the model and the TALIF experiments then more quantitative evidence of atomic oxygen recycling would be obtained and provide more validation of the pathway analysis results presented in this thesis.

Appendix A

List of Species

List of Species	
Neutral Species	Ar, He, CO_2, CO, O_2, O, O_3, C
Excited Species	$CO_2(v_a\text{-}v_d)$, $CO_2(v_1\text{-}v_{21})$, O_2v, COv, O*, O_2*, Ar*, Ar**, Ar_2*, He*, He_2*
Charged Species	e^-, CO_2^+, Ar^+, Ar_2^+, He^+, He_2^+, O_2^+, O_2^-, O_4^+, O_4^-, O^+, O^-, C^+, CO^+, O_3^-

Appendix B

Chemical Reaction Set

No.	Reaction	A[1] ($cm^3 s^{-1}$)	B	C[2] (K)	Ref
	Charged Particle Reactions				
(1)	$e^- + Ar \rightarrow Ar + e^-$	$\sigma(\epsilon)$			[125]
(2)	$e^- + Ar \rightarrow Ar^* + e^-$	$\sigma(\epsilon)$			[125]
(3)	$e^- + Ar \rightarrow Ar^{**} + e^-$	$\sigma(\epsilon)$			[125]
(4)	$e^- + Ar \rightarrow Ar^* + e^-$	$\sigma(\epsilon)$			[125]
(5)	$e^- + Ar \rightarrow Ar^+ + e^- + e^-$	$\sigma(\epsilon)$			[125]
(6)	$e^- + Ar^* \rightarrow Ar + e^-$	$\sigma(\epsilon)$			[125]
(7)	$e^- + Ar^* \rightarrow Ar^{**} + e^-$	$\sigma(\epsilon)$			[125]
(8)	$e^- + Ar^* \rightarrow Ar^+ + e^- + e^-$	$\sigma(\epsilon)$			[125]
(9)	$e^- + Ar^+ \rightarrow Ar^+ + e^-$	$\sigma(\epsilon)$			[125]
(10)	$e^- + Ar^+ \rightarrow Ar$	$\sigma(\epsilon)$			[125]
(11)	$e^- + Ar^{**} \rightarrow Ar + e^-$	$\sigma(\epsilon)$			[125]
(12)	$e^- + Ar^{**} \rightarrow Ar^* + e^-$	$\sigma(\epsilon)$			[125]
(13)	$e^- + Ar^{**} \rightarrow Ar^+ + e^- + e^-$	$\sigma(\epsilon)$			[125]
(14)	$e^- + Ar_2^+ \rightarrow Ar_2^+ + e^-$	$\sigma(\epsilon)$			[125]
(15)	$e^- + Ar_2^+ \rightarrow Ar^* + Ar$	$\sigma(\epsilon)$			[125]
(16)	$e^- + He \rightarrow He + e^-$	$\sigma(\epsilon)$			[126]
(17)	$e^- + He \rightarrow He^* + e^-$	$\sigma(\epsilon)$			[126]
(18)	$e^- + He \rightarrow He^+ + e^- + e^-$	$\sigma(\epsilon)$			[126]
(19)	$e^- + He^* \rightarrow He^* + e^-$	$\sigma(\epsilon)$			[126]
(20)	$e^- + He^* \rightarrow He^+ + e^- + e^-$	$\sigma(\epsilon)$			[126]
(21)	$e^- + He^* \rightarrow He + e^-$	$\sigma(\epsilon)$			[126]
(22)	$e^- + He^+ \rightarrow He^+ + e^-$	$\sigma(\epsilon)$			[126]

(23)	$e^- + He^+ \rightarrow He^* + e^-$	$\sigma(\epsilon)$	[126]
(24)	$e^- + He_2^+ \rightarrow He_2^+ + e^-$	$\sigma(\epsilon)$	[88]
(25)	$e^- + He_2^+ \rightarrow He + He^*$	$\sigma(\epsilon)$	[88]
(26)	$e^- + CO_2 \rightarrow CO_2 + e^-$	$\sigma(\epsilon)$	[107]
(27)	$e^- + CO_{2V_i} \rightarrow CO_{2V_j} + e^-$	$\sigma(\epsilon)$	[64]
(28)	$e^- + CO_2 \rightarrow CO + O^-$	$\sigma(\epsilon)$	[107]
(29)	$e^- + CO_2 \rightarrow CO_2^+ + e^- + e^-$	$\sigma(\epsilon)$	[107]
(30)	$e^- + CO_2 \rightarrow CO + O^* + e^-$	$\sigma(\epsilon)$	[107]
(31)	$e^- + CO_2^+ \rightarrow CO_2^+ + e^-$	$\sigma(\epsilon)$	[107]
(32)	$e^- + CO_2^+ \rightarrow CO + O$	$\sigma(\epsilon)$	[107]
(33)	$e^- + CO \rightarrow CO + e^-$	$\sigma(\epsilon)$	[152]
(34)	$e^- + CO \rightarrow CO_v + e^-$	$\sigma(\epsilon)$	[123]
(35)	$e^- + CO \rightarrow C + O + e^-$	$\sigma(\epsilon)$	[123]
(36)	$e^- + CO \rightarrow CO_v + e^-$	$\sigma(\epsilon)$	[123]
(37)	$e^- + CO \rightarrow CO^+ + e^- + e^-$	$\sigma(\epsilon)$	[123]
(38)	$e^- + CO \rightarrow CO^+ + e^- + e^-$	$\sigma(\epsilon)$	[123]
(39)	$e^- + CO \rightarrow C^+ + O + e^- + e^-$	$\sigma(\epsilon)$	[123]
(40)	$e^- + CO \rightarrow C + O^+ + e^- + e^-$	$\sigma(\epsilon)$	[123]
(41)	$e^- + O_2 \rightarrow O_2 + e^-$	$\sigma(\epsilon)$	[115]
(42)	$e^- + O_2 \rightarrow O^- + O$	$\sigma(\epsilon)$	[115]
(43)	$e^- + O_2 \rightarrow O_2 * + e^-$	$\sigma(\epsilon)$	[115]
(44)	$e^- + O_2 \rightarrow O + O + e^-$	$\sigma(\epsilon)$	[115]
(45)	$e^- + O_2 \rightarrow O_2^* + e^-$	$\sigma(\epsilon)$	[115]
(46)	$e^- + O_2 \rightarrow O_2^+ + e^- + e^-$	$\sigma(\epsilon)$	[115]
(47)	$e^- + O_2 \rightarrow O + O + e^-$	$\sigma(\epsilon)$	[115]
(48)	$e^- + O_2 \rightarrow O + O^+ + e^- + e^-$	$\sigma(\epsilon)$	[115]
(49)	$e^- + O_2^+ \rightarrow O_2^+ + e^-$	$\sigma(\epsilon)$	[115]
(50)	$e^- + O^- \rightarrow O^- + e^-$	$\sigma(\epsilon)$	[153]
(51)	$e^- + O \rightarrow O + e^-$	$\sigma(\epsilon)$	[153]
(52)	$e^- + O \rightarrow O^* + e^-$	$\sigma(\epsilon)$	[153]
(53)	$e^- + O \rightarrow O + e^-$	$\sigma(\epsilon)$	[153]
(54)	$e^- + O \rightarrow O^+ + e^- + e^-$	$\sigma(\epsilon)$	[153]
(55)	$e^- + O_2 \rightarrow O_{2v} + e^-$	$\sigma(\epsilon)$	[115]
(56)	$e^- + O_2^* \rightarrow O_2^* + e^-$	$\sigma(\epsilon)$	[115]
(57)	$e^- + O_2^* \rightarrow O^- + O$	$\sigma(\epsilon)$	[115]
(58)	$e^- + O_2^* \rightarrow O_2 + e^-$	$\sigma(\epsilon)$	[115]

(59)	$e^- + O_2^* \rightarrow O + O + e^-$	$\sigma(\epsilon)$			[115]
(60)	$e^- + O_2^* \rightarrow O_2^* + e^-$	$\sigma(\epsilon)$			[115]
(61)	$e^- + O_2^* \rightarrow O_2^+ + e^- + e^-$	$\sigma(\epsilon)$			[115]
(62)	$e^- + O_2^* \rightarrow O + O + e^-$	$\sigma(\epsilon)$			[115]
(63)	$e^- + O^* \rightarrow O^* + e^-$	$\sigma(\epsilon)$			[115]
(64)	$e^- + O^* \rightarrow O + e^-$	$\sigma(\epsilon)$			[115]
(65)	$e^- + O^* \rightarrow O^+ + e^- + e^-$	$\sigma(\epsilon)$			[115]
(66)	$e^- + O_3 \rightarrow O_3 + e^-$	$\sigma(\epsilon)$			[118]
(67)	$e^- + O_3 \rightarrow O^- + O_2$	$\sigma(\epsilon)$			[119]
(68)	$e^- + O_3 \rightarrow O_2^- + O$	$\sigma(\epsilon)$			[119]
(69)	$e^- + O_3^- \rightarrow O_3^- + e^-$	$\sigma(\epsilon)$			[119]
(70)	$e^- + O_{2v} \rightarrow O_{2v} + e^-$	$\sigma(\epsilon)$			[115]
(71)	$e^- + O_{2v} \rightarrow O^- + O$	$\sigma(\epsilon)$			[115]
(72)	$e^- + O_{2v} \rightarrow O_2 + e^-$	$\sigma(\epsilon)$			[115]
(73)	$e^- + O_{2v} \rightarrow O_2^* + e^-$	$\sigma(\epsilon)$			[115]
(74)	$e^- + O_{2v} \rightarrow O + O + e^-$	$\sigma(\epsilon)$			[115]
(75)	$e^- + O_{2v} \rightarrow O_2^* + e^-$	$\sigma(\epsilon)$			[115]
(76)	$e^- + O_{2v} \rightarrow O_2^+ + e^- + e^-$	$\sigma(\epsilon)$			[115]
(77)	$e^- + O_{2v} \rightarrow O + O + e^-$	$\sigma(\epsilon)$			[115]
(78)	$e^- + O_{2v} \rightarrow O^+ + O + e^- + e^-$	$\sigma(\epsilon)$			[115]
(79)	$Ar^+ + e^- + e^- \rightarrow AR^* + e^-$	5.0×10^{-27}	-4.5	0	[88]
(80)	$Ar^+ + e^- \rightarrow Ar^*$	4.0×10^{-13}	-0.5	0	[88]
(81)	$Ar^+ + Ar \rightarrow Ar + Ar^+$	5.66×10^{-10}	0.5	0	[88]
(82)	$Ar^+ + e^- + e^- \rightarrow Ar + e^-$	7.0×10^{-27}	0	0	[154]
(83)	$Ar^+ + e^- + e^- \rightarrow Ar^{**} + e^-$	7.18×10^{-27}	-4.5	0	[155]
(84)	$Ar^+ + e^- + Ar \rightarrow Ar^{**} + Ar$	3.0×10^{-28}	0	0	[155]
(85)	$Ar^+ + Ar + Ar \rightarrow Ar_2^+ + Ar$	2.5×10^{-31}	0	0	[156]
(86)	$Ar_2^+ + e^- \rightarrow Ar^{**} + Ar$	1.9×10^{-07}	-0.55	0	[157]
(87)	$Ar_2^+ + e^- \rightarrow Ar^+ + Ar + e^-$	1.36×10^{-06}	-1.0	2.094	[158]
(88)	$Ar_2^+ + e^- \rightarrow Ar + Ar$	2.738×10^{-05}	-0.67	0	[154]
(89)	$Ar^* + Ar^* \rightarrow Ar^+ + Ar + e^-$	1.00×10^{-10}	0	0	[157]
(90)	$Ar^* + Ar^* \rightarrow Ar_2^+ + e^-$	6.30×10^{-10}	-0.5	0	[155]
(91)	$Ar^* + Ar^{**} \rightarrow Ar^+ + Ar + e^-$	1.20×10^{-09}	0	0	[88]
(92)	$Ar^{**} + Ar^{**} \rightarrow Ar^+ + Ar + e^-$	5.00×10^{-10}	0	0	[157]
(93)	$Ar^{**} + Ar \rightarrow Ar_2^+ + e^-$	2.00×10^{-9}	0	0	[154]
(94)	$O + O + Ar \rightarrow O_2 + Ar$	9.26×10^{-34}	-1.0	0	[120]

(95)	$Ar^* + O_2 \rightarrow Ar + O_2$	1.12×10^{-09}	0	0	[87]
(96)	$Ar^* + O \rightarrow Ar + O$	8.10×10^{-12}	0	0	[87]
(97)	$Ar^* + O_2 \rightarrow Ar + O + O$	5.80×10^{-11}	0	0	[87]
(98)	$Ar^+ + O_2 \rightarrow O_2^+ + Ar$	5.00×10^{-11}	0	0	[159]
(99)	$Ar^+ + O \rightarrow O^+ + Ar$	6.40×10^{-12}	0	0	[159]
(100)	$Ar^+ + O^- \rightarrow Ar + O$	2.70×10^{-07}	0	0	[159]
(101)	$Ar + O^+ \rightarrow O + Ar^+$	2.10×10^{-11}	0	0	[159]
(102)	$Ar + O_2^+ \rightarrow O_2 + Ar^+$	2.10×10^{-11}	0	0	[159]
(103)	$Ar_2^+ + O_2 \rightarrow Ar + Ar + O_2^+$	1.00×10^{-10}	0	0	[160]
(104)	$O_2^- + Ar^+ \rightarrow O_2 + Ar$	1.00×10^{-07}	0	0	[161]
(105)	$O_2^- + Ar_2^+ \rightarrow O_2 + Ar + Ar$	1.00×10^{-07}	0	0	[161]
(106)	$O^- + Ar_2^+ \rightarrow O + Ar + Ar$	1.00×10^{-07}	0	0	[161]
(107)	$O_3^- + Ar^+ \rightarrow O_3 + Ar$	1.00×10^{-07}	0	0	[161]
(108)	$O_3^- + Ar_2^+ \rightarrow O_3 + Ar + Ar$	1.00×10^{-07}	0	0	[161]
(109)	$O_2^- + CO_2^+ \rightarrow CO_2 + O_2$	5.00×10^{-07}	-0.5	0	[162]
(110)	$Ar^+ + O_3 \rightarrow O_2^+ + Ar + O$	4.00×10^{-11}	0.5	0	[162]
(111)	$Ar^+ + CO_2 \rightarrow CO_2^+ + Ar$	5.00×10^{-10}	0.5	0	[162]
(112)	$Ar^+ + CO \rightarrow CO^+ + Ar$	4.00×10^{-11}	0.5	0	[162]
(113)	$Ar_2^+ + CO_2 \rightarrow CO_2^+ + Ar + Ar$	1.10×10^{-09}	0	0	[163]
(114)	$Ar_2^+ + CO \rightarrow CO^+ + Ar + Ar$	8.50×10^{-10}	0	0	[163]
(115)	$He^+ + O^* \rightarrow O^+ + He$	5.00×10^{-11}	0.5	0	[83]
(116)	$He^+ + O_2^* \rightarrow O_2^+ + He$	3.30×10^{-11}	0.5	0	[83]
(117)	$He^+ + O_2^* \rightarrow O^+ + O + He$	1.07×10^{-09}	0.5	0	[83]
(118)	$He^+ + O \rightarrow O^+ + He$	5.00×10^{-11}	0.5	0	[83]
(119)	$He^+ + O_2 \rightarrow O_2^+ + He$	3.30×10^{-11}	0.5	0	[83]
(120)	$He^+ + O_3 \rightarrow O^+ + O_2 + He$	1.07×10^{-09}	0.5	0	[83]
(121)	$He^+ + O_2 \rightarrow O^+ + O + He$	1.07×10^{-09}	0.5	0	[83]
(122)	$O_3^- + He^+ \rightarrow O_3 + He$	2.00×10^{-07}	1.0	0	[83]
(123)	$O_2^- + He^+ \rightarrow O_2 + He$	2.00×10^{-07}	1.0	0	[83]
(124)	$He^+ + He + He \rightarrow He + He_2^+$	6.60×10^{-32}	0	0	[86]
(125)	$O_2^+ + He + O_2 \rightarrow He + O_4^+$	3.90×10^{-30}	-3.2	0	[86]
(126)	$O_4^+ + He^* \rightarrow O_2^+ + O_2 + He$	1.00×10^{-10}	0	0	[86]
(127)	$O_2^+ + O_4^- \rightarrow O_2 + O_2 + O_2 + He$	1.00×10^{-31}	-2.5	0	[86]
(128)	$O_4^+ + O^- + He \rightarrow O + O_2 + O_2 + He$	1.00×10^{-31}	-2.5	0	[86]
(129)	$O_4^+ + O_2^- + He \rightarrow O_2 + O_2 + O_2 + He$	1.00×10^{-31}	-2.5	0	[86]
(130)	$O_4^+ + O_3^- + He \rightarrow O_3 + O_2 + O_2 + He$	1.00×10^{-31}	-2.5	0	[86]

(131) $O_4^+ + O_4^- + He \rightarrow O_2 + O_2 + O_2 + O_2 + He$	1.00×10^{-31}	-2.5	0	[86]
(132) $O_4^- + He^* \rightarrow O_2 + O_2 + He + e^-$	3.00×10^{-10}	0	0	[86]
(133) $O_2^- + O_2 + O_2 \rightarrow O_2 + O_4^-$	3.50×10^{-31}	-1.0	0	[86]
(134) $O_2^+ + O_2 + O_2 \rightarrow O_4^+ + O_2$	3.90×10^{-30}	-3.2	0	[86]
(135) $O_4^+ + O^* \rightarrow O_2^+ + O + O_2$	1.00×10^{-10}	0	0	[64]
(136) $O_2^+ + O_2 + M \rightarrow M + O_4^+$	3.90×10^{-42}	0	0	[64]
(137) $O_4^- + O^* \rightarrow O + O_2 + O_2 + e^-$	1.00×10^{-10}	0	0	[64]
(138) $O_4^- + O_2* \rightarrow O_2 + O_2 + O_2 + e^-$	1.00×10^{-10}	0	0	[64]
(139) $O_4^- + e^- + e^- \rightarrow O_2 + O_2 + e^-$	9.80×10^{-15}	0	0	[64]
(140) $O_4^- + O_2^+ \rightarrow O_2 + O_2 + O_2$	1.00×10^{-07}	0	0	[161]
(141) $O_4^- + O_4^+ \rightarrow O_2 + O_2 + O_2 + O_2$	1.00×10^{-07}	0	0	[161]
(142) $O_4^+ + O_2 \rightarrow O_2^+ + O_2 + O_2$	3.30×10^{-06}	-4.0	5030	[164]
(143) $O_4^+ + O_2^* \rightarrow O_2^+ + O_2 + O_2$	1.00×10^{-10}	0	0	[164]
(144) $O_4^+ + O \rightarrow O_2^+ + O_3$	3.00×10^{-10}	0	0	[164]
(145) $O_4^+ \rightarrow O_2^+ + O_2$	7.36×10^{-10}	-0.5	0	[165]
(146) $O_4^+ + e^- \rightarrow O_2 + O_2$	2.20×10^{-07}	0	0	[88]
(147) $O^+ + O_2 \rightarrow O_2^+ + O$	2.00×10^{-11}	-0.4	0	[165]
(148) $e^- + O_2 + O_2 \rightarrow O_2^- + O_2$	3.00×10^{-31}	-1.0	1300	[164]
(149) $e^- + O + O_2 \rightarrow O_2 + O^-$	1.00×10^{-31}	0	0	[164]
(150) $e^- + O + O_2 \rightarrow O_2^- + O$	1.00×10^{-31}	0	0	[164]
(151) $e^- + O_3 + O_2 \rightarrow O_3^- + O_2$	3.00×10^{-29}	-1.0	1300	[164]
(152) $O_2^- + O_2 \rightarrow O_2 + O_2 + e^-$	2.70×10^{-10}	0.5	5590	[164]
(153) $O_2^- + O_2^* \rightarrow O_2 + O_2 + e^-$	2.00×10^{-10}	0	0	[164]
(154) $O^- + O_2^* \rightarrow O_3 + e^-$	3.00×10^{-10}	0	0	[164]
(155) $O_2^- + O \rightarrow O_3 + e^-$	1.50×10^{-10}	0	0	[164]
(156) $O_3^- + O \rightarrow O_2 + O_2 + e^-$	3.00×10^{-10}	0	0	[164]
(157) $O^- + O_2 \rightarrow O_3 + e^-$	5.00×10^{-15}	0	0	[164]
(158) $O_2^- + O \rightarrow O^- + O_2$	3.30×10^{-10}	0	0	[164]
(159) $O_2^- + O_3 \rightarrow O_2 + O_3^-$	4.00×10^{-10}	0	0	[164]
(160) $O^- + O_2^* \rightarrow O_2^- + O$	1.00×10^{-10}	0	0	[164]
(161) $O^- + O_3 \rightarrow O_3^- + O$	5.30×10^{-10}	0	0	[164]
(162) $O_3^- + O \rightarrow O_2^- + O_2$	3.20×10^{-10}	0	0	[164]
(163) $O^- + O_2^+ \rightarrow O_2 + O$	2.60×10^{-08}	0.44	0	[164]
(164) $O^- + O_2^+ \rightarrow O + O + O$	2.00×10^{-07}	-0.5	0	[164]
(165) $O^- + O^+ \rightarrow O + O$	2.70×10^{-07}	-0.5	0	[164]
(166) $O^- + O \rightarrow O_2 + e^-$	3.00×10^{-10}	-0.5	0	[164]

(167) $O^- + O_2 \rightarrow O_2 + O + e^-$	6.90×10^{-10}	0	0	[164]
(168) $O_2^- + O^+ \rightarrow O + O_2$	1.00×10^{-07}	0	0	[166]
(169) $O_2^- + O_2^+ \rightarrow O_2 + O_2$	1.00×10^{-07}	0	0	[166]
(170) $O_3^- + O^+ \rightarrow O_3 + O$	1.00×10^{-07}	0	0	[166]
(171) $O_3^- + O_2^+ \rightarrow O_3 + O_2$	1.00×10^{-07}	0	0	[166]
(172) $O_2^+ + O_3^- \rightarrow O_2 + O_3$	2.00×10^{-07}	-1.0	0	[64]
(173) $O_3^- + Ar^+ \rightarrow O_3 + Ar$	2.00×10^{-07}	1.0	0	[163]
(174) $O_3^- + O_2 \rightarrow O_3 + O_2 + e^-$	2.30×10^{-11}	0	0	[163]
(175) $e^- + O_2 + M \rightarrow O_2^- + M$	2.00×10^{-31}	0	0	[162]
(176) $e^- + O_2^+ \rightarrow O^* + O$	2.00×10^{-07}	-0.5	0	[162]
(177) $e^- + O_3 \rightarrow e^- + O_2 + O^*$	1.00×10^{-09}	0.5	0	[162]
(178) $e^- + e^- + O^+ \rightarrow e^- + O^*$	5.00×10^{-27}	0	0	[162]
(179) $e^- + e^- + C^+ \rightarrow C + e^-$	5.00×10^{-27}	0	0	[162]
(180) $CO_2^+ + O_2 \rightarrow O_2^+ + CO_2$	5.60×10^{-11}	0.5	0	[64]
(181) $CO_2^+ + O \rightarrow O^+ + CO_2$	9.62×10^{-11}	0.5	0	[64]
(182) $CO_2^+ + O \rightarrow O_2^+ + CO$	1.64×10^{-10}	0.5	0	[64]
(183) $CO_2^+ + CO \rightarrow CO_2 + CO^+$	1.90×10^{-12}	0.5	0	[162]
(184) $CO^+ + CO_2 \rightarrow CO_2^+ + CO$	1.10×10^{-09}	0.5	0	[64]
(185) $CO^+ + O_2 \rightarrow CO + O_2^+$	1.40×10^{-10}	0.5	0	[64]
(186) $CO^+ + O \rightarrow CO + O^+$	1.40×10^{-10}	0.5	0	[167]
(187) $CO^+ + O_2^- \rightarrow CO + O_2$	2.00×10^{-07}	-0.5	0	[162]
(188) $O^+ + CO_2 \rightarrow CO_2^+ + O$	1.00×10^{-09}	0.5	0	[162]
(189) $O^- + O_2 \rightarrow O_2^- + O$	1.50×10^{-12}	0.5	0	[162]
(190) $O^- + CO \rightarrow CO_2 + e^-$	5.50×10^{-10}	0.5	0	[64]
(191) $O^- + O^+ + M \rightarrow O_2 + M$	1.20×10^{-25}	-1.5	0	[162]
(192) $O^- + CO_2^+ \rightarrow CO_2 + O$	3.00×10^{-06}	-0.5	0	[162]
(193) $O^- + CO^+ \rightarrow O + CO$	2.00×10^{-07}	-0.5	0	[162]
(194) $C^+ + O^- \rightarrow C + O$	5.00×10^{-08}	-0.5	0	[162]
(195) $C^+ + O_2^- \rightarrow C + O_2$	5.00×10^{-08}	-0.5	0	[162]
(196) $O^+ + CO_2 \rightarrow CO + O_2^+$	9.40×10^{-10}	0	0	[168]
(197) $O^+ + CO_2 \rightarrow O + CO_2^+$	4.50×10^{-10}	0	0	[64]
(198) $C^+ + CO_2 \rightarrow CO + CO^+$	1.10×10^{-09}	0	0	[64]
(199) $O^+ + CO \rightarrow O + CO^+$	4.90×10^{-12}	0.5	4580	[64]
(200) $C^+ + CO \rightarrow C + CO^+$	5.00×10^{-13}	0	0	[64]
(201) $CO^+ + C \rightarrow C^+ + CO$	1.10×10^{-10}	0	0	[64]
(202) $O_2^+ + C \rightarrow CO^+ + O$	5.20×10^{-11}	0	0	[64]

(203) $e^- + C \rightarrow e^- + C$	3.83×10^{-13}	0	0	[24]
(204) $e^- + C \rightarrow e^- + e^- + C^+$	1.40×10^{-14}	0	0	[24]
(205) $O_2^+ + C \rightarrow C^+ + O_2$	5.20×10^{-11}	0	0	[64]
(206) $CO_2^+ + O \rightarrow CO + O_2^+$	1.64×10^{-10}	0	0	[64]
(207) $CO_2^+ + O \rightarrow O^+ + CO_2$	9.62×10^{-11}	0	0	[64]
(208) $CO_2^+ + O_2 \rightarrow CO_2 + O_2^+$	5.30×10^{-11}	0	0	[64]
(209) $CO^+ + O \rightarrow CO + O^+$	1.40×10^{-10}	0	0	[64]
(210) $CO^+ + O_2 \rightarrow CO + O_2^+$	1.20×10^{-10}	0	0	[64]
(211) $C^+ + O_2 \rightarrow CO + O^+$	6.20×10^{-10}	0	0	[64]
(212) $C^+ + O_2 \rightarrow CO^+ + O$	3.80×10^{-10}	0	0	[64]
(213) $O^+ + O_2 \rightarrow O + O_2^+$	1.90×10^{-11}	-0.5	0	[64]
(214) $O^- + O_2 + M \rightarrow O_3^- + M$	3.00×10^{-28}	-1	0	[64]
(215) $O^- + O_3 \rightarrow O + O_3^-$	8.00×10^{-10}	0	0	[64]
(216) $O^- + O_3 \rightarrow O_2 + O_2 + e^-$	3.00×10^{-10}	0	0	[64]
(217) $O_3^- + O_3 \rightarrow O_2 + O_2 + O_2 + e^-$	3.00×10^{-10}	0	0	[64]
(218) $O^+ + O_3 \rightarrow O_2^+ + O_2$	1.00×10^{-10}	0	0	[64]
(219) $O^+ + O + M \rightarrow O_2^+ + M$	1.00×10^{-29}	0	0	[64]
(220) $O_3^- + O \rightarrow O_3 + O^-$	1.00×10^{-13}	0	0	[64]
(221) $O_2^- + O^+ + M \rightarrow O_3 + M$	2.00×10^{-25}	0	0	[64]
(222) $O_2^- + O^+ \rightarrow O + O_2$	2.70×10^{-07}	0	0	[64]
(223) $O_2^- + O_2^+ \rightarrow O_2 + O + O$	4.20×10^{-07}	0	0	[64]
(224) $O_2^- + O_2^+ + M \rightarrow O_2 + O_2 + M$	2.00×10^{-25}	0	0	[64]
(225) $O^- + O_2^+ + M \rightarrow O_3 + M$	2.00×10^{-25}	0	0	[64]
(226) $O^- + M \rightarrow O + M + e^-$	4.00×10^{-12}	0	0	[64]
(227) $e^- + CO_2^+ \rightarrow C + O_2$	3.94×10^{-07}	-0.4	0	[64]
(228) $e^- + CO^+ \rightarrow C + O$	3.68×10^{-08}	-0.55	0	[64]
(229) $e^- + O_3 + M \rightarrow O_3^- + M$	5.00×10^{-31}	-0.5	0	[64]
(230) $e^- + O + M \rightarrow O^- + M$	1.00×10^{-31}	0	0	[64]
(231) $e^- + O_2^+ + M \rightarrow O_2 + M$	1.00×10^{-26}	0	0	[64]
(232) $e^- + O^+ + M \rightarrow O + M$	1.00×10^{-26}	0	0	[64]
(233) $e^- + CO \rightarrow e^- + e^- + CO^+$	1.44×10^{-16}	0.0	0	[24]
(234) $e^- + CO_{2v_i} \rightarrow e^- + e^- + CO^+ + O$	9.10×10^{-13}	0.5	12.94 (eV)	[163]
(235) $e^- + CO_{2v_i} \rightarrow e^- + e^- + C^+ + O_2$	9.10×10^{-13}	0.5	12.94 (eV)	[163]
(236) $e^- + CO_{2v_i} \rightarrow e^- + e^- + O^+ + CO$	9.10×10^{-13}	0.5	12.94 (eV)	[163]
(237) $e^- + CO_{2v_i} \rightarrow e^- + e^- + O_2^+ + C$	4.55×10^{-13}	0.5	12.94 (eV)	[163]
(238) $e^- + CO \rightarrow e^- + C + O$	1.00×10^{-12}	0	0	[163]

(239)	$e^- + CO_v \rightarrow e^- + C + O$	1.00×10^{-12}	0	0	[163]
(240)	$e^- + CO_2 \rightarrow O^- + CO$	5.00×10^{-13}	1.5	0	[163]
(241)	$e^- + CO \rightarrow O^- + C$	8.00×10^{-15}	1	0	[163]
(242)	$e^- + O_3 \rightarrow e^- + e^- + O_2^+ + O$	3.20×10^{-11}	0.5	12.94 (eV)	[163]
	Neutral Particle Reactions				
(243)	$O + O_3 \rightarrow O_2 + O_2$	3.10×10^{-14}	0.75	1575	[65]
(244)	$O_3 + CO \rightarrow CO_2 + O_2$	4.00×10^{-25}	0	0	[64]
(245)	$CO_2 + C \rightarrow CO + CO$	1.00×10^{-15}	0	0	[64]
(246)	$O + C + M \rightarrow CO + M$	2.14×10^{-29}	-3.08	2114	[64]
(247)	$O^* + O_3 \rightarrow O_2 + O_2$	5.04×10^{-10}	0.5	0	[169]
(248)	$O^* + CO \rightarrow CO + O$	4.70×10^{-11}	0	62.54	[170]
(249)	$O^* + CO \rightarrow CO_2$	8.00×10^{-11}	0	0	[169]
(250)	$O_{2v} + M \rightarrow O_2 + M$	1.00×10^{-12}	0.5	0	[171]
(251)	$O_2^* + CO_2 \rightarrow CO_2 + O_2$	3.01×10^{-19}	0	0	[172]
(252)	$O_2^* + O_2 \rightarrow O + O_3$	2.95×10^{-21}	0.5	0	[173]
(253)	$O^* + O \rightarrow O + O$	2.54×10^{-12}	0	0	[174]
(254)	$O^* + O_2^* \rightarrow O + O_2$	1.00×10^{11}	0.5	0	[175]
(255)	$O^* + CO_2 \rightarrow O + CO_2$	2.50×10^{-10}	0.5	0	[169]
(256)	$O^* + CO_2 \rightarrow O_2 + CO$	2.01×10^{-10}	0	0	[110]
(257)	$O_3 + M \rightarrow O_2 + O + M$	3.32×10^{-09}	0	11700	[122]
(258)	$O_2 + M \rightarrow O + O + M$	5.17×10^{-10}	0	58410	[109]
(259)	$C + O_2 \rightarrow CO + O$	2.60×10^{-11}	0.5	0	[176]
(260)	$O + O + M \rightarrow O_2 + M$	5.21×10^{-35}	0	900	[109]
(261)	$O^* + O_3 \rightarrow O_2 + O + O$	1.20×10^{-10}	0.5	0	[177]
(262)	$O + O_2 + M \rightarrow O_3 + M$	6.90×10^{-34}	0	0	[121]
(263)	$CO_v + M \rightarrow CO + M$	1.00×10^{-12}	0.5	0	[171]
(264)	$CO + O_3 \rightarrow O_2 + CO_2$	4.00×10^{-25}	0.5	0	[105]
(265)	$CO + O + M \rightarrow CO_2 + M$	1.70×10^{-33}	0	1510	[109]
(266)	$CO + O_2 \rightarrow CO_2 + O$	4.20×10^{-12}	0	24000	[109]
(267)	$Ar^* + CO \rightarrow C + O + Ar$	1.40×10^{-11}	0.5	0	[129]
(268)	$Ar^* + CO_2 \rightarrow Ar + CO + O$	5.30×10^{-10}	0.5	0	[129]
(269)	$He^* + CO_2 \rightarrow He + CO + O^+ + e^-$	4.80×10^{-10}	0	0	[98]
(270)	$He^* + CO_2 \rightarrow He + CO^+ + O + e^-$	6.00×10^{-10}	0	0	[98]
(271)	$He^* + CO_2 \rightarrow He + CO_2^+ + e^-$	6.00×10^{-10}	0	0	[98]
(272)	$He^* + O_2 \rightarrow O_2^+ + He + e^-$	2.54×10^{-10}	0.5	0	[83]
(273)	$He^* + O_3 \rightarrow O_2^+ + O + He + e^-$	2.54×10^{-10}	0.5	0	[83]

(274)	$He^* + O \rightarrow O^+ + He + e^-$	2.54×10^{-10}	0.5	0	[83]
(275)	$He^* + O^* \rightarrow O^+ + He + e^-$	2.54×10^{-10}	0.5	0	[83]
(276)	$He^* + He^* \rightarrow He + He^+ + e^-$	4.50×10^{-10}	0	0	[178]
(277)	$He^* + He_2^* \rightarrow He + He + He^+ + e^-$	5.00×10^{-10}	0	0	[178]
(278)	$He^* + He^* \rightarrow He_2^+ + e^-$	1.05×10^{-09}	0	0	[178]
(279)	$He^* + He^* \rightarrow He^+ + He + e^-$	4.50×10^{-08}	0	0	[178]
(280)	$He^* + He_2^* \rightarrow He_2^+ + He + e^-$	1.28×10^{-10}	0	0	[178]
(281)	$He^* + He_2^* \rightarrow He^+ + He + He + e^-$	2.25×10^{-09}	0	0	[178]
(282)	$He_2^* + He_2^* \rightarrow He_2^+ + He + He + e^-$	1.28×10^{-10}	0	0	[178]
(283)	$He_2^* + He_2^* \rightarrow He^+ + He + He + He + e^-$	2.25×10^{-09}	0	0	[178]
(284)	$He_2^* + CO \rightarrow CO^+ + He + He + e^-$	5.21×10^{-10}	0	0	[98]
(285)	$He_2^* + CO_2 \rightarrow CO_2^+ + He + He + e^-$	9.66×10^{-10}	0	0	[98]
(286)	$Ar_2^* + e^- \rightarrow Ar + Ar + e^-$	1.00×10^{-09}	0	0	[179]
(287)	$Ar^{**} + Ar + M \rightarrow Ar_2^* + M$	3.00×10^{-33}	0.5	0	[180]
(288)	$Ar^{**} + O_2 \rightarrow O^* + O + Ar$	2.10×10^{-10}	0.5	0	[129]
(289)	$Ar^{**} + O_3 \rightarrow O^* + O_2 + Ar$	2.10×10^{-10}	0.5	0	[129]
(290)	$Ar^* + O_3 \rightarrow O^* + O_2 + Ar$	2.10×10^{-10}	0.5	0	[129]
(291)	$Ar^* + O_2 \rightarrow O^* + O + Ar$	2.10×10^{-10}	0.5	0	[129]
(292)	$He^* + He + He \rightarrow He_2^* + He$	2.00×10^{-40}	0	0	[83]
(293)	$He + O^* \rightarrow He + O$	1.00×10^{-13}	0	0	[86]
(294)	$He + O_3 \rightarrow He + O + O_2$	1.56×10^{-09}	0	11400	[86]
(295)	$He + He + He^* \rightarrow He + He_2^*$	1.50×10^{-34}	0	0	[86]
(296)	$O_2^* + He \rightarrow O_2 + He$	8.00×10^{-21}	0.5	0	[83]
(297)	$O + O + He \rightarrow O_2^* + He$	9.88×10^{-41}	-0.63	0	[83]
(298)	$O_3 + O_3 \rightarrow O + O_2 + O_3$	1.60×10^{-15}	0	11400	[64]
(299)	$O_3 + O \rightarrow O + O + O_2$	9.40×10^{-17}	0	11400	[64]
(300)	$O^* + O_2 \rightarrow O + O_2^+$	3.20×10^{-11}	0	67	[181]
(301)	$O_2^* + O \rightarrow O_2 + O$	2.00×10^{-16}	0	0	[181]
(302)	$O_2^* + O_2 \rightarrow O_2 + O_2$	3.00×10^{-18}	0	200	[181]
(303)	$O_2^* + O_3 \rightarrow O_2 + O_2 + O$	5.20×10^{-11}	0	2840	[181]
(304)	$O_2^* + O_2^* \rightarrow O_2 + O_2$	1.80×10^{-16}	0	560	[181]
(305)	$CO_{2V_i} + Ar \rightarrow CO + O + Ar$	1.49×10^{-11}	-0.58	65000	[108]
(306)	$CO_{2V_i} + He \rightarrow CO + O + He$	1.49×10^{-11}	-0.58	65000	[108]
(307)	$CO_{2V_i} + O \rightarrow CO + O_2$	2.80×10^{-11}	0	26500	[109]
(308)	$CO_{2V_i} + O_2 \rightarrow CO + O + O_2$	3.72×10^{-10}	0	60451	[61]
(309)	$CO_{2V_i} + CO_2 \rightarrow CO + O + CO_2$	3.72×10^{-10}	0	60451	[61]

(310)	$CO_{2V_i} + CO \rightarrow CO + O + CO$	3.72×10^{-10}	0	60451	[61]
	CO_2 Vibrational Reactions				
(311)	$CO_{2V_x} + Ar \rightarrow CO_{2V_{x-1}} + Ar$	1.38×10^{-14}	0	0	[111]
(312)	$CO_{2V_i} + Ar \rightarrow CO_{2V_{i-1}} + Ar$	9.08×10^{-17}	0	0	[111]
(313)	$CO_{2V_x} + He \rightarrow CO_{2V_{x-1}} + He$	1.10×10^{-13}	0	0	[111]
(314)	$CO_{2V_i} + He \rightarrow CO_{2V_{i-1}} + He$	1.10×10^{-15}	0	0	[111]
(315)	$CO_{2V_x} + M \rightarrow CO_2 + M$	7.14×10^{-08}	$exp(-177T_g^{-1/3}+451T_g^{-2/3})$		[65]
(316)	$CO_{2V_i} + M \rightarrow CO_{2V_{i-1}} + M$	1.43×10^{-05}	$exp(-252T_g^{-1/3}+685T_g^{-2/3})$		[65]
(317)	$CO_{2V_i} + CO_2 \rightarrow CO_{2V_{i-1}} + CO_{2V_x}$	2.13×10^{-05}	$exp(-242T_g^{-1/3}+633T_g^{-2/3})$		[65]
(318)	$CO_{2V_i} + CO_{2V_j} \rightarrow CO_{2V_{i-1}} + CO_{2V_{j+1}}$	1.80×10^{-11}	$exp(24.7T_g^{-1/3} -65.7T_g^{-2/3})$		[65]

Rate coefficients in the form $A(\frac{T}{300})^B \exp^{(\frac{-C}{T})}$ for heavy particle collisions, unless otherwise stated,
and $A(T_e^B)e^{(\frac{-C}{T_e})}$ for electron impact collisions.
1 $cm^6 s^{-1}$ for three body collisions.
2 eV for electron impact reactions, as stated in the table.
V_i corresponds to the asymmetric (1-21) CO_2 vibrational states and V_x the symmetric (a-d).

Bibliography

[1] International Energy Agency. *Technology Roadmap Carbon Capture and Storage*. International Energy Agency, 2013.

[2] Rosa M. Cuéllar-Franca and Adisa Azapagic. Carbon capture, storage and utilisation technologies: A critical analysis and comparison of their life cycle environmental impacts. *Journal of CO_2 Utilization*, 9:82 – 102, 2015.

[3] P. Styring, H. de Coninck, and K. Armstrong. *Carbon Capture and Utilisation in the Green Economy*. The Centre for Low Carbon Futures 2011, 2011.

[4] A. Hunt, E. Sin, R. Marriott, and J. Clark. Generation, capture and utilization of industrial carbon dioxide. *ChemSusChem*, 3:306–322, 2010.

[5] G. A. Olah, A. Goeppert, and G. K. S. Prakash. Chemical Recycling of Carbon Dioxide to Methanol and Dimethyl Ether: From Greenhouse Gas to Renewable, Environmentally Carbon Neutral Fuels and Synthetic Hydrocarbons. *The Journal of Organic Chemistry*, 74:487–498, 2009.

[6] Z. Jiang, T. Xiao, V. L. Kuznetsiv, and P. P. Edwards. Turing carbon dioxide into fuel. *Philos. Trans. R. Soc. A*, 368:3343–3364, 2010.

[7] K. M. K. Yu et al. Recent Advances in CO_2 Capture and Utilization. *ChemSusChem*, 1:893–899, 2008.

[8] O. Joo et al. Carbon Dioxide Hydrogenation to Form Methanol via a Reverse-Water-Gas-Shift Reaction (the CAMERE Process). *Industrial and Engineering Chemistry Research*, 38:1808–1812, 1999.

[9] S. C. Roy, O. K. Varghese, M. Paulose, and C. A. Grimes. Toward Solar Fuels: Photocatalytic Conversion of Carbon Dioxide to Hydrocarbons. *ACS Nano*, 4:1259–1278, 2010.

[10] G. Centi, E. A. Quadrelli, and S. Perathoner. Catalysis for CO_2 conversion: a key technology for rapid introduction of renewable energy in the value chain of chemical industries. *Energy Environmental Science*, 6:1711, 2013.

[11] G.P. Torrence, J.D. Hendricks, D.D. Dickinson, and A. Aguilo. Addition of hydrogen to carbon monoxide feed gas in producing acetic acid by carbonylation of methanol, 1992. CA Patent 1,299,195.

[12] T. Morimoto et al. CO-Transfer Carbonylation Reactions. A Catalytic Pauson-Khand-Type Reaction of Enyes with Aldehydes as a Source of Carbon Monoxide. *J. Am. Chem. Soc.*, 15:3806–3807, 2002.

[13] J. Guo et al. Dry reforming of methane over nickel catalysts supported on magnesium aluminate spinels. *Applied Catalysis A*, 273:75–82, 2004.

[14] J. A. Herron et al. A general frramework for the assessment of solar fuel technologies. *Energy and Environmental*, 8:126–157, 2015.

[15] R. Snoeckx et al. CO_2 conversion in a dielectric bariier discharge plasma: N_2 in the mix as a helping hand or problematic impurity? *Energy Environ. Sci.*, 9:999–1011, 2016.

[16] Moon Soo Bak, and Seong-Kyun Im, and Cappelli, M. Nanosecond-Pulsed Discharge Plasma Splitting of Carbon Dioxide. *IEEE Transactions on Plasma Science*, 43:1002–1007, 2015.

[17] F. Brehmer et al. CO and byproduct formation during CO_2 reduction in dielecric barrier discharges. *J. Appl. Phys.*, 116:123303, 2014.

[18] S. Heijkers et al. CO_2 Conversion in a Microwave Plasma Reactor in the Presence of N_2: Elucidating the Role of Vibrational Levels. *J. Phys. Chem.*, 119:12815–12828, 2015.

[19] F Brehmer et al. Gas temperature in transient CO plasma measured by Raman scattering. *Journal of Physics D: Applied Physics*, 48(15):155201, 2015.

[20] T. Silva et al. Optical Characterization of a Microwave Pulsed Discharge used for Dissociation of CO_2. *Plasma Sources Sci. Technol.*, 23:025009, 2014.

[21] O. Taylan and H. Berberoglu. Dissociation of carbon dioxide using a microhollow cathode discharge plasma reactor: effects of applied voltage, flow rate and concentration. *Plasma Sources Sci. Technol.*, 24:015006, 2015.

[22] Spencer, L. and Gallimore, A. CO_2 dissociation in an atmospheric pressure plasma/catalyst system: a study of efficiency. *Plasma Sources Sci. Technol.*, 22:015019, 2013.

[23] F. F. Chen. *Introduction to plasma physics and controlled fusion.* Plenum Press, 1984.

[24] G. J. M. Hagelaar and L. C. Pitchford. Solving the Boltzmann equation to obtain electron transport coefficients and rate coefficients for fluid models. *Plasma Sci. Sources and Tech.*, 14:722–733, 2005.

[25] International Telecommunications Union. *Radio Regulations volume 1.* ITU Publications, 2012.

[26] Guerra, V., S, P. A., and Loureiro, J. Kinetic modeling of low-pressure nitrogen discharges and post-discharges. *Eur. Phys. J. Appl. Phys.*, 28(2):125–152, 2004.

[27] V. Laporta, R. Celiberto, and J. Tennyson. Dissociative electron attachment and electron-impact resonant dissociation of vibrationally excited o_2 molecules. *Phys. Rev. A*, 91:012701, Jan 2015.

[28] V. Laporta, R. Celiberto, and J. Tennyson. Resonant vibrational-excitation cross sections and rate constants for low-energy electron scattering by molecular oxygen. *Plasma Sources Science and Technology*, 22:025001, 2013.

[29] A. Laricchiuta, R. Celiberto, and M. Capitelli. Electron impact cross-sections for electronic excitation of vibrationally excited O_2 to $B^3\ \Sigma_u^-$ state. *Chemical Physics Letters*, 329:526–532, 2000.

[30] F. Paschen. Ueber die zum funkenübergang in luft, wasserstoff und kohlensäure bei verschiedenen drucken erforderliche potentialdifferenz. *Annalen der Physik*, 273:69, 1889.

[31] R. Massarczyk, P. Chu, C. Dugger, S. Elliott, K. Rielage, and W. Xu. Paschen's law studies in cold gases. *Journal of Instrumentation*, 12:P06019, 2017.

[32] J. J. Shi and M. G. Kong. Evolution of discharge structure in capacitive radio-frequency atmospheric microplasmas. *Physical Review Letters*, 96:105009, 2006.

[33] S. Gordon and B. J. McBride. *Computer Program for Calculation of Complex Chemical Equilibrium Compositions and Applications I. Analysis.* NASA, 1994.

[34] B. J. McBride and S. Gordon. *Computer Program for Calculation of Complex Chemical Equilibrium Compositions and Applications II. User's Manual and Program Description.* NASA, 1996.

[35] Yu. P. Butylkin, L. S. Polak, and Slovetsky. High energy chemistry. *Sov. Phys.*, 12:526, 1978.

[36] Niek den Harder, Dirk C. M. van den Bekerom, Richard S. Al, Martijn F. Graswinckel, Jose M. Palomares, Floran J. J. Peeters, Srinath Ponduri, Teofil Minea, Waldo A. Bongers, Mauritius C. M. van de Sanden, and Gerard J. van Rooij. Homogeneous CO_2 conversion by microwave plasma: Wave propagation and diagnostics. *Plasma Processes and Polymers*, 14(6):1600120, 2017.

[37] Spencer, L. and Gallimore, A. Efficiency of CO_2 Dissociation in a Radio-Frequency Discharge. *Plasma Chem. Plasma Process.*, 31:79–89, 2011.

[38] A. Lebouvier et al. Assessment of Carbon Dioxide Dissociation as a New Route for Syngas Production : A Comparative Review and Potential of Plasma- Based Technologies. *Energy & Fuels*, 27:2712–2722, 2013.

[39] Mori, S., Yamamoto, A. and Suzuki, M. Characterization of a capillary plasma reactor for carbon dioxide decomposition. *Plasma Sources Sci. Technol.*, 15:609–613, 2006.

[40] G Horváth, J D Skalný, and N J Mason. FTIR study of decomposition of carbon dioxide in dc corona discharges. *Journal of Physics D: Applied Physics*, 41(22):225207, 2008.

[41] R. Snoeckx et al. Plasma-based dry reforming: improving the conversion and energy efficiency in a dielectric barrier discharge. *The Royal Society of Chemistry*, 5:29799–29808, 2015.

[42] R. Li. Influence of dielectric barrier materials to the behavior of dielectric barrier discharge plasma for CO_2 decomposition. *Solid State Ionics*, 172:235–238, 2004.

[43] R. Li, Q. Tang, S. Yin, and T. Sato. Plasma catalysis for CO_2 decomposition by using different dielectric materials. *Fuel processing technology*, 87:617–622, 2006.

[44] Q. Yu, M. Kong, T. Liu, J. Fei, and X. Zheng. Characteristics of the decomposition of CO_2 in a dielectric packed-bed plasma reactor. *Plasma Chemistry and Plasma Processing*, 32:153–163, 2012.

[45] S. Wang, Y. Zhang, X. Liu, and X. Wang. Enhancement of CO_2 conversion rate and conversion efficiency by homogeneous discharges. *Plasma Chem Plasma Process*, 32:979–989, 2012.

[46] D. Mei, X. Zhu, Y. He, J. Yan, and X. Tu. Plasma assited conversion of CO_2 in a dielectric barrier discharge reactor: understanding the effect of packing materials. *Plasma Sources Science and Technology*, 24:015011, 2014.

[47] M. Lindon and E. Scime. CO_2 dissociation using the versatile atmospheric dielectric barrier discharge experiment (VADER). *Front. Phys.*, 2:55, 2014.

[48] D. Yap, J. Tatibout, and C. Batiot-Dupeyrat. Carbon dioxide dissociation to carbon monoxide by non-thermal plasma. *Journal of CO_2 Utilization*, 12:5461, 2015.

[49] S. Ponduri, M. Becker, S. Welzel, M. van de Sanden, D. Loffhagen, and R. Engeln. Fluid modelling of CO_2 dissociation in a dielectric barrier discharge. *Journal of Applied Physics*, 119:093301, 2016.

[50] Sabine Paulussen, Bert Verheyde, Xin Tu, Christophe De Bie, Tom Martens, Dragana Petrovic, Annemie Bogaerts, and Bert Sels. Conversion of carbon dioxide to value-added chemicals in atmospheric pressure dielectric barrier discharges. *Plasma Sources Science and Technology*, 19(3):034015, 2010.

[51] M. Ramakers, I. Michielsen, R. Aerts, V. Meynen, and A. Bogaerts. Effect of Argon or Helium on the CO_2 Conversion in a Dielectric Barrier Discharge. *Plasma Processes and Polymers*, 12(8):755–763, 2015.

[52] G. Zheng, J. Jiang, Y. Wu, R. Zhang, and H. Hou. The Mutual Conversion of CO_2 and CO in Dielectric Barrier Discharge (DBD). *Plasma Chemistry and Plasma Processing*, 23(1):59–68, 2003.

[53] A. Ozkan et al. The influence of power and frequency on the filamentary behavior of a flowing DBD - application to the splitting of CO_2. *Plasma Sources Sci. Technol.*, 25:025013, 2016.

[54] A. Vesel, M. Mozetic, A. Drenik, and M. Balat-Pichelin. Dissociation of CO_2 molecules in microwave plasma. *Chemical Physics*, 382:127–131, 2011.

[55] G. J. van Rooij, D. C. M. van den Bekerom, N. den Harder, T. Minea, G. Berden, W. A. Bongers, R. Engeln, M. F. Graswinckel, E. Zoethout, and M. C. M. van de Sanden. Taming microwave plasma to beat thermodynamics in co2 dissociation. *Faraday Discuss.*, 183:233–248, 2015.

[56] W. Bongers et al. Plasma-driven dissociation of CO_2 for fuel synthesis. *Plasma Processes and Polymers*, 14:1600126, 2017.

[57] T. Silva et al. Understanding CO_2 decomposition in microwave plasma by means of optical diagnostics. *Plasma Processes and Polymers*, 14:1600103, 2017.

[58] R. I. Asisov et al. Non-equilibrium plasma-chemical process of CO_2 decomposition in a supersonic microwave discharge. *Proc. of the USSR Academy of Sciences*, 271:94, 1983.

[59] V. D. Rusanov, A. A. Fridman, and G. V. Sholin. The physics of a chemically active plasma with nonequilibrium vibrational excitation of molecules. *Sov. Phys. Uspekhi*, 24:447, 1981.

[60] L. Pietanza et al. Vibrational excitation and dissociation mechanisms of CO_2 under non-equilibrium discharge and post-discharge conditions. *Plasma Sources Sci. Technol.*, 24:042002, 2015.

[61] A. Fridman. *Plasma Chemistry*. Cambridge University Press, 2008.

[62] L. Pietanza et al. Time-dependent coupling of electron energy distribution function, vibrational kinetics of the asymmetric mode of CO_2 and dissociation, ionization and electronic excitation kinetics under discharge and post-discharge conditions. *Plasma Phys. Control. Fusion*, 59:014035, 2017.

[63] I. Suzuki. General anharmonic force constants of carbon dioxide. *Jounral of Molecular Spectroscopy*, 25:479–500, 1968.

[64] Kozák, T. and Bogaerts, A. Splitting of CO_2 by vibrational excitation in non-equilibrium plasmas: a reaction kinetics model. *Plasma Sources Science and Technology*, 23:045004, 2014.

[65] Kozak, T. and Bogaerts, A. Evaluation of the energy efficiency of CO_2 conversion in microwave discharges using a reaction kinetics model. *Plasma Sources Sci. Technol.*, 24:015024, 2015.

[66] M. Capitelli, G. Colonna, G. DAmmando, and L. D. Pietanza. Self-consistent time dependent vibrational and free electron kinetics for CO_2 dissociation and ionization in cold plasmas. *Plasma Sources Science and Technology*, 26:055009, 2017.

[67] A. A. Offenberger and D. J. Rose. Roles of Helium and Nitrogen in CO_2 Laser Excitation. *Jounral of Applied Physics*, 41:3908, 1970.

[68] W. J. Wiegand and Nighan W. L. Plasma chemistry of CO_2-N_2-He discharges. *Applied Physics Letters*, 22:583, 1973.

[69] N. Britun, T. Godfroid, and R. Snyders. Time resolved study of pulsed ar-n_2 and ar-n_2-h_2 microwave surfaguide discharges using optical emission spectroscopy. *Plasma Sources Sci. Technol.*, 21:035007, 2012.

[70] L. Brown and A. Bell. Kinetics of the oxidation of carbon monoxide and the decomposition of carbon dioxide in a radiofrequency electric discharge. i. experimental results. *Industrial and Engineering Chemistry Fundamentals*, 13:203–210, 1974.

[71] L. Brown and A. Bell. Kinetics of the oxidation of carbon monoxide and the decomposition of carbon dioxide in a radiofrequency electric discharge. ii. theoretical interpretation. *Industrial and Engineering Chemistry Fundamentals*, 13:210–218, 1974.

[72] P. Capezzuto, R. Cramarossa, and E. Molinari. Contribution of vibrational excitation to the rate of carbon dioxide dissociation in electrical discharges. *Journal of Physical Chemistry*, 80:882–888, 1976.

[73] S. Savinov, L. Hwaung, H. Song, and B. Na. Decomposition of methane and carbon dioxide in a radio-frequency discharge. *Industrial and Engineering Chemistry Fundamentals*, 38:2540–2547, 1999.

[74] A. Ozkan, T. Dufour, G. Arnoult, P. De Keyzer, A. Bogaerts, and F. Reniers. $CO_2 2CH_4$ conversion and syngas formation at atmospheric pressure using a multi-electrode dielectric barrier discharge. *Journal of CO_2 Utilization*, 9:74 – 81, 2015.

[75] A. Yamamoto, S. Mori, and M. Suzuki. Scale-up or numbering-up of a micro plasma reactor for the carbon dioxide decomposition. *Thin Solid Films*, 515:4296 – 4300, 2007.

[76] J. Golda, J. Held, B. Redeker, M. Konkowski, P. Beijer, A. Sobota, G. Kroesen, N. St J Braithwaite, S. Reuter, M. M. Turner, T. Gans, D. OConnell, and V. Schulz von der Gathen. Concepts and characteristics of the COST Reference Microplasma Jet. *Journal of Physics D: Applied Physics*, 49:084003, 2016.

[77] V. Schulz-von der Gathen, L. Schaper, N. Knake, S. Reuter, K. Niemi, T. Gans, and J. Winter. Spatially resolved diagnostics on a microscale atmospheric pressure plasma jet. *J. Phys. D: Appl. Phys.*, 41:194004, 2008.

[78] V. Schulz-von der Gathen, V. Buck, T. Gans, N. Knake, K. Niemi, L. Reuter, L. Schaper, and J. Winter. Optical diagnostics of micro discharge jets. *Contributions to Plasma Physics*, 47:510, 2007.

[79] J. Winter, R. Brandenburg, and K. D. Weltman. Atmospheric pressure plasma jets: an overview of devices and new directions. *Plasma Sources Science and Technology*, 24:064001, 2015.

[80] Godyak, V. A. and Piejak, R. B. In situ simultaneous radio frequency discharge power measurements. *J. Vac. Sci. Technol. A*, 8:3833, 1990.

[81] S. Hofmann et al. Power dissipation, gas temperatures and electron densities of cold atmospheric pressure helium and argon rf plasma jets. *Plasma Sources Sci. Technol.*, 20:065010, 2011.

[82] D. Marinov and N. St J Braithwaite. Power coupling and electrical characterization of a radio-frequency micro atmospheric pressure plasma jet. *Plasma Sources Science and Technology*, 23:062005, 2014.

[83] Stafford, S. and Kushner, M. O_2 production in He/O_2 mixtures in flowing low pressure plasmas. *Journal of Applied Physics*, 96(5):2451–2465, 2004.

[84] Hurlbatt A., Gibson A. R., Schröter S., Bredin J., Foote A. P. S., Grondein P., O'Connell D., and Gans T. Concepts, Capabilities, and Limitations of Global Models: A Review. *Plasma Processes and Polymers*, 14:1600138, 2016.

[85] D. D. Monahan and M. M. Turner. Global models of electronegative discharges: critical evaluation and practical recommendations. *Plasma Sources Science and Technology*, 17:045003, 2008.

[86] T. Murakami, K. Niemi, T. Gans, D. O'Connell, and W. G. Graham. Chemical kinetics and reactive species in atmospheric pressure helium-oxygen plasmas with humid-air impurities. *Plasma Sources Sci. Technol.*, 22:015003, 2013.

[87] C. Lee and M. A. Lieberman. Global model of Ar, O_2, Cl_2, and Ar/O_2 high-density plasma discharges. *Journal of Vacuum Science and Technology A*, 13:368, 1995.

[88] J. J. Munro and J. Tennyson. Global Plasma Simulations using Dynamically Generated Chemical Models. *J. Vac. Sci. Technol. A*, 26:865, 2008.

[89] J. P. Dedrick, S. Schröter, K. Niemi, A. Wijaikhum, E. Wagenaars, N. de Oliveira, L. Nahon, J.P. Booth, D. O'Connell, and T. Gans. Controlled production of atomic oxygen and nitrogen in a pulsed radio-frequency atmospheric-pressure plasma. *Journal of Physics D: Applied Physics*, 50:1–8, 2017.

[90] T. Murakami, K. Niemi, T. Gans, D. O'Connell, and W. G. Graham. Afterglow chemistry of atmospheric-pressure heliumoxygen plasmas with humid air impurity. *Plasma sources science and technology*, 23:025005, 2014.

[91] J. Waskoenig, K. Niemi, N. Kanke, L. M. Graham, S. Reuter, and V. Schulz-von der Gathen T. Gans. Atomic oxygen formation in a radio-frequency driven micro-atmospheric pressure plasma jet. *Plasma sources science and technology*, 19:045018, 2010.

[92] J. Waskoenig, K. Niemi, N. Kanke, L. M. Graham, S. Reuter, V. Schulz-von der Gathen, and T. Gans. Diagnostic-based modeling on a micro-scale atmospheric-pressure plasma jet. *Pure Appl. Chem.*, 82:1209–1222, 2010.

[93] P. N. Brown, G. D. Byrne, and A.C. Hindmarsh. Vode: A variable-coefficient ode solver. *SIAM J. Sci. Stat. Comput.*, 10:1038–1051, 1989.

[94] S. Schröter, A. R. Gibson, M . J. Kushner, T. Gans, and D. O'Connell. Numerical study of the influence of surface reaction probabilities on reactive species in an rf atmospheric pressure plasma containing humidity. *Plasma Physics and Controlled Fusion*, 60:1–10, 2018.

[95] A. Markosyan et al. PumpKin: A tool to find principal pathways in plasma chemcial models. *Computer Physics Communications*, 185:2697–2702, 2014.

[96] A. Wijaikhum, D. Schröder, S. Schröter, A. R. Gibson, K. Niemi, J. F., A. Greb, V. Schulz-von der Gathen, D. O'Connell, and T. Gans. Absolute ozone densities in a radio-frequency driven atmospheric pressure plasma using two-beam uv-led absorption spectroscopy and numerical simulations. *Plasma Sources Science and Technology*, 26:1–27, 2017.

[97] M. Grofulovi, L. ALves, and V. Guerra. Electron-neutral scattering cross sections for CO_2: a complete and consistent set and an assessment of dissociation. *J. Phys. D: Appl. Phys.*, 49:395207, 2016.

[98] M. Tsuji et al. Decomposition of CO_2 into CO and O in a Microwave-Excited Discharge Flow of CO_2/He or CO_2/Ar mixtures. *The Chemical Society of Japan Chemistry Letters*, 30:22–23, 2001.

[99] Y.P. Raizer. *Gas Discharge Physics*. Springer, 1997.

[100] W. G. Huo and Z. F. Ding. Alpha to Gamma Mode Transitions in Pulse-Modulated Radio Frequency Atmospheric Pressure Glow Discharges. *IEEE Transactions on Plasma Science*, 44:2282 – 2287, 2016.

[101] J. J. Shi and M. Kong. Mode characteristics of radio-frequency atmospheric glow discharges. *IEEE Transactions on Plasma Science*, 33:624, 2005.

[102] S Kechkar, P Swift, S Kelly, S Kumar, S Daniels, and M Turner. Investigation of the electron kinetics in o 2 capacitively coupled plasma with the use of a langmuir probe. *Plasma Sources Science and Technology*, 26(6):065009, 2017.

[103] M. S. Moss, K. Yanallah, R. W. K. Allen, and F. Pontiga. An investigation of CO_2 splitting using nanosecond pulsed corona discharge: effect of argon addition on CO_2 conversion and energy efficiency. *Plasma Sources Science and Technology*, 26:035009, 2017.

[104] A.A. Azooz, S. Cakir, and D.A. Bleej. Plasma parameters in 40MHz Argon discharge. *Results in Physics*, 5:85–91, 2015.

[105] L. M. Arin and P. Warneck. Reaction of ozone with carbon monoxide. *J. Phys. Chem.*, 76:1514–1516, 1972.

[106] M. M. Turner. Uncertainty and sensitivity analysis in complex plasma chemistry models. *Plasma Sources Science and Technology*, 25:015003, 2015.

[107] J. J. Lowke, A. V. Phelps, and B. W. Irwin. Predicted electron transport coefficients and operating characteristics of co_2-n_2-he laser mixtures. *J. Appl. Phys.*, 44:4664–4671, 1973.

[108] W. E. Kaskan and W. G. Browne. *Kinetics of the $H_2/CO/O_2$ System.* General Electric CO., 1964.

[109] W. Tsang and R. F. Hampson. Chemical Kinetic Data Base for Combustion Chemistry. Part I. Methane and Related Compounds. *Jounral of Physical and Chemical Reference Data*, 15:1087, 1986.

[110] R. F. Heidner and D. Husain. Kinetic Investigation of Electronically Excited Oxygen Atoms, $O(2^1D_2)$, by Time-Resolved Attenuation of Atomic Resonance Radiation in the Vacuum Ultra-Violet. Part2. Collisional quenching by the Atmospheric Gases N_2, O_2, CO, CO_2, H_2O and O_3. *J. Chem. Soc. Faraday Trans. 2*, 69, 1973.

[111] M. Huetz-Aubert and R. Tripodi. Rate Equations for the Vibrational Relaxation of CO_2-N_2 or CO_2- Noble Gas Mixtures- Application to Comparison of Spectrophone Data with Results from Other Experimental Techniques. *The Journal of Chemical Physics*, 55:5724–5734, 1971.

[112] D.C. Clary. Ab initio computation of vibrational relaxation rate coefficients for the collision of CO_2 with helium and neon atoms. *Chemical Physics*, 65:247–257, 1982.

[113] G. Kamimoto and H. Matsui. Vibrational relaxation of carbon dioxide in argon. *The Journal of Chemical Physics*, 53:3990–3993, 197.

[114] R. Levine and R. Bernstein. *Thermodynamic approach to collision processes. Dynamics of Molecular Collisions*. New York Springer, 1976.

[115] S.J. Buckman and A.V. Phelps. *Tabulations of Collision Cross Sections and Calculated Transport and Reaction Coefficients for Electrons in H_2 and D_2*. Jila Information Center Report No. 27, 1985.

[116] A. Bogaerts, T. Kozak, K. van Laer, and R. Snoeckx. Plasma-based conversion of CO_2: current status and future challenges. *Faraday Discussions*, 183:217–232, 2015.

[117] K. Kutszegi Corvin and S. J. B. Corrigan. Dissociation of Carbon Dioxide in the Positive Column of a Glow Discharge. *The Journal of Chemical Physics*, 50(6):2570–2574, 1969.

[118] H. Jacobs et al. Reaction Kinetics and Chemical Quasi-Equilibria of the Ozone Synthesis in Oxygen DC Discharges. *Contributions to Plasma Physics*, 36:471–486, 1996.

[119] S. Matejcik et al. Electron Attachment to molecules and clusters of atmospheric relevence: oxygen and ozone. *Plasma Sources Sci. Technol.*, 6:140–146, 1997.

[120] M. J. Kirkpatrick, B. Dodet, and E. Odic. Atmospheric Pressure Humid Argon DBD Plasma for the Application of Sterilization - Measurement and Simulation of Hydrogen, Oxygen and Hydrogen Peroxide Formation. *International Journal of Plasma Environment Science and Technology*, 1:96–101, 2007.

[121] O. Klais, P. C. Anderson, and M. J. Kurylo. A reinvestigation of the temperature dependence of the rate constant for the reaction O + O_2 + M -> O_3 + M (for M=O_2, N_2 and Ar) by the flash photolysis resonance fluoresence technique. *International Journal of Chemical Kinetics*, 12:469–490, 1980.

[122] S. Toby and E. Ullrich. Reaction of carbon monoxide with ozone: Kinetics and chemiluminescence. *Int. J. Chem. Kinet.*, 12:535–546, 1980.

[123] W. Liu and G. A. Victor. Electron Energy Deposition in Carbon Monoxide Gas. *The Astrophysical Journal*, 435:909–919, 1994.

[124] O'Neill, C. Waskoenig, J. and Gans, T. Tailoring electron energy distribution functions through energy confinement in dual radio-frequency driven atmospheric pressure plasmas. *Applied Physics Letters*, 101:154107, 2012.

[125] K. Tachibana. Excitation of the $1s_5$,$1s_4$,$1s_3$, and $1s_2$ levels of argon by low-energy electrons. *Physical Review A*, 34:1007, 1986.

[126] L. Vriens. Calculation of Absolute Ionization Cross Sections of He, He*, He^+, Ne, Ne*, He, He*, Hg, and Hg*. *Physics Letters*, 8:260–261, 1964.

[127] S. G. Kukolich. Demonstration of the ramsauer - townsend effect in a xenon thyratron. *American Journal of Physics*, 36:701–701, 1968.

[128] Michał Gryziński. Ramsauer Effect as a Result of the Dynamic Structure of the Atomic Shell. *Phys. Rev. Lett.*, 24:45–47, 1970.

[129] J. E. Velazio, J. H. Kolts, and D. W. Setser. Rate constants and quenching mechanisms for the metastable states of argon, krypton and xenon. *J. Chem. Phys.*, 69:4357–4373, 1978.

[130] D. O'Connell, T. Gans, E. Semmler, and P. Awakowicz. The role of the relative voltage and phase for frequency coupling in a dual-frequency capacitively coupled plasma. *Applied Physics Letters*, 93:081502, 2008.

[131] M. M. Turner and P. Chabert. Collisionless heating in capacitive discharges enhanced by dual-frequency excitation. *Physical Review Letters*, 96:205001, 2006.

[132] E. Kawamura, M. A. Lieberman, and A. J. Lichtenberg. Stochastic heating in single and dual frequency capacitive discharges. *Physics of Plasmas*, 13:053506, 2006.

[133] K. Niemi, C. O'Neill, L. J. Cox, J. Waskoenig, W. B. Hyland, S. J. McMahon, S. Reuter, F. J. Currell, W. G. Graham, D. O'Connell, and T. Gans. Cold atmospheric pressure plasma jets: Interaction with plasmid DNA and tailored electron heating using dual-frequency excitation. *AIP Conference Proceedings*, 1438:23–28, 2012.

[134] N. Knake, K. Niemi, S. Reuter, V. Schulz-von der Gathen, and J. Winter. Absolute atomic oxygen density profiles in the discharge core of a microscale atmospheric pressure plasma jet. *Applied Physics Letters*, 93:131503, 2008.

[135] N. Knake, S. Reuter, K. Niemi, V. Schulz-von der Gathen, and J. Winter. Absoulte atomic oxygen density distributions in the effluent of a microscale atmospheric pressure plasma jet. *Journal of Physics D: Applied Physics*, 41:194006, 2008.

[136] K. Niemi, Schulz von der Gathen, and H. Döbele. Absolute atomic oxygen density measurements by two-photon absorption laser-induced fluoresence spectroscopy in an RF-excited atmospheric pressure plasma jet. *Plasma Sources Science and Technology*, 14:375, 2005.

[137] K. Niemi, D. O'Connell, N. de Oliveira, D. Joyeux, L. Nahon, J.P. Booth, and T. Gans. Absolute atomic oxygen and nitrogen densities in radio-frequency driven atmospheric pressure cold plasmas: Synchrotron vacuum ultra-violet high-resolution Fourier-transform absorption measurements. *Applied Physics Letters*, 103:034102, 2013.

[138] S. Schröter, M. Foucher, K. Niemi, J. P. Dedrick, N. de Oliveira, D. Joyeux, L. Nahon, E. Wagenaars, T. Gans, J.P. Booth, and D. O'Connell. *Atomic oxygen and hydroxyl density measurements in an atmospheric pressure RF-plasma with water admixtures using UV and synchrotron VUV absorption spectroscopy.* 2015.

[139] A. Goehlich, T. Kawetzki, and H. F. Döbele. On absolute calibration with xenon of laser diagnostic methods based on two-photon absorption. *Journal of Chemcial Physics*, 108:9362, 1998.

[140] R. Loudon. *The Quantum Theory of Light.* Oxford University Press, 3rd Edition edition, 2000.

[141] J. Bittner, K. Kohse-Höinghaus, U. Meier, S. Kelm, and Just Th. Dtermination of absolute H atom concentrations in low-pressure flames by two-photon laser-excited fluorescence. *Combustion and Flame*, 71:41–50, 1988.

[142] V. Alekseev and D. W. Setser. Quenching Rate Constants and Product Assignments for Reactions of Xe($7p[3/2]_2$,$7p[5/2]_2$ and $6p'[3/2]_2$) Atoms with Rare Gases, CO, H_2, N_2O, CH_4 and Halogen-Containing Molecules. *Journal of Phyical Chemistry*, 100:5766–5780, 1996.

[143] T. B. Settersten, A. Dreizler, and R. L. Farrow. Temperature- and species-dependent quenching of CO B probed by two-photon laser-induced fluorescence using a picosecond laser. *Journal of Chemical Physics*, 117:3173–3179, 2002.

[144] H. F. Döbele, T. Mosbach, K. Niemi, and V. Schulz-von der Gathen. Laser-induced fluorescence measurements of absolute atomic densities: concepts and limitations. *Plasma Sources Science and Technology*, 14:S31, 2005.

[145] Andrew Thomas West. *Optical and Electrical Diagnosis of Atmospheric Pressure Plasma Jets*. PhD thesis, The University of York, 2016.

[146] J. Bittner, K. Kohse-höinghaus, U. Meier, and Th. Just. Quenching of two-photon-excited H(3s, 3d) and O(3p 3p2,1,0) atoms by rare gases and small molecules. *Chemical Physics Letters*, 143:571 – 576, 1988.

[147] S. Linow, A. Dreizler, J. Janicka, and E. P. Hassel. Comparison of two-photon excitation schemes for CO detection in flames. *Applied Physics B*, 71:689–696, 2000.

[148] V. Laporta, J. Tennyson, and R. Celiberto. Carbon monoxide dissoicative attachment and resonant dissociation by electron-impact. *Plasma Sources Science and Technology*, 25:01LT04, 2016.

[149] V. Laporta, C. M. Cassidy, J. Tennyson, and R. Celiberto. Electron-impact resonant vibration excitation cross sections and rate coefficients for carbon monoxide. *Plasma Sources Science and Technology*, 21:045005, 2012.

[150] Aerts, R., and Snoeckx, R. and Bogaerts, A.e. In-Situ Chemical Trapping of Oxygen in the Splitting of Carbon Dioxide by Plasma. *Plasma Process. Polym.*, 11:985–992, 2014.

[151] W. Han, F. Jin, and Q. Zhou. Ligand-Free Palladium-Catalyzed Hydroxycarbonylation of Aryl Halides under Ambient Conditions: Synthesis of Aromatic Carboxylic Acids and Aromatic Esters. *Synthesis*, 47:1861–1868, 2015.

[152] A. Jain and D. W. Norcross. Slow-electron collisions with co molecules in an exact-exchange plus parameter-free polarization model. *Physical Review A*, 45:1644–1656, 1992.

[153] Y. Itikawa and Ichimura A. Cross Sections for Collisions of Electrons and Photons with Atomic Oxygen. *J. Phys. Chem. Ref. data*, 19:637, 1990.

[154] A. Bogaerts and R. Gijbels. Role of Ar^{2+} and Ar_2^+ in a direct current argon glow discharge: A numerical description. *Journal of Applied Physics*, 86:4124, 1999.

[155] N. Kang et al. Modeling and experimental study of pulse modulated ICP discharge: production of ar highly excited states. *Plasma Sources Sci. Technol.*, 20:035002, 2011.

[156] M. Moravej et al. Properties of an atmospheric pressure radio-frequency argon and nitrogen plasma. *Plasma Sources Sci. Technol.*, 15:204–210, 2006.

[157] D. J. Eckstrom et al. Characteristics of electron-beam-excited Kr_2^* at low pressures as a vacuum ultraviolet source. *Journal of Applied Physics*, 64:1691, 1988.

[158] A. Bultel et al. Influence of Ar_2^+ in an argon collisional-radiative model. *Physical Review E*, 65:046406, 2002.

[159] Bogaerts A. Effects of oxygen addition to argon glow discharges: A hybrid Monte Carlo-fluid modelling investigation. *Spectrochimica Acta Part B: Atomic Spectroscopy*, 64:1266–1279, 2009.

[160] Raksit A. B. Reactions of Ar_2^+ Ions with Neutral Molecules. *International Journal of Mass Spectrometry and Ion Processes*, 66:109–119, 1985.

[161] A. P. Hickman. Approximate Scaling Formula for Ion-Ion Mutual Neutralization Rates. *Plasma Sources Sci. Technol.*, 70:4872–4878, 1979.

[162] Laura Frances Spencer. *The Study of CO_2 Conversion in a Microwave Plasma/Catalyst System.* PhD thesis, The University of Michigan, 2012.

[163] Beuthe, T. and Chang, J. Chemical Kinetic Modelling of Non-Equilibrium Ar-CO_2 Thermal Plasmas. *Jpn. J. Appl. Phys.*, 36:4997–5002, 1997.

[164] I. A. Kossyi et al. Kinetic scheme of the non-equilibrium discharge in nitrogen-oxygen mixtures. *Plasma Sources Sci. Technol.*, 1:207–220, 1992.

[165] L. W. Sieck, J. T. Herron, and D. S. Green. Chemical Kinetics Database and Predictive Schemes for Humid Air Plasma Chemistry. Part I: Positive Ion-Molecule Reactions. *Plasma Chemistry and Plasma Processing*, 20:235–258, 2000.

[166] A.P. Hickman. Approximate scaling formula for ion-ion mutual neutralization rates. *J. Chem. Phys.*, 70:4872–4878, 1978.

[167] W. Lindinger et al. Temperature dependence of some ionospheric ion-neutral reactions from 300-900 K. *Journal of Geophysical Research*, 79:4753–4756, 1974.

[168] D. Smith, Adams N. G., and Miller T. M. A laboratory study of the reaction of N^+, N_2^+, N_3^+, N_4^+, O^+, O_2^+ and NO^+ ions with several molecules at 300 K. *J. Chem. Phys.*, 69:308–318, 1978.

[169] J. C. Tully. Reactions of $O(^1D)$ with atmospheric molecules. *Journal of Chemical Physics*, 62:1893–1898, 1975.

[170] J. A. Davidson et al. Temperature dependence of the deactivation of $O(^1D)$ by CO from 113-333 K. *J. CHem. Phys.*, 69:1216–1217, 1978.

[171] E. E. Nikitin, A. I. Osipov, and Umansky C. Y. *Reviews of Plasma Chemistry.* Consultants Bureau New York London, 1994.

[172] I. A. McLaren, N. W. Morris, and R.P. Wayne. Is CO_2 a good quencher of $O_2(^1ig)$? A kinetic reappraisal. *J. Photochem.*, 16:311–319, 1981.

[173] R. K. Datta and K. N. Rao. Kinetics of reactions of singlet molecular oxygen $(^1\delta g)$ with organic compounds. *Indian Journal of Chemistry*, 18:102–105, 1979.

[174] J. H. A. Sobral et al. Determination of the quenching rate of the $O(^1D)$ by $O(^3P)$ from rocket-borne optical (630nm) and electron density data. *J. Geophys. Res.*, 98:7791–7798, 1993.

[175] V. M. Doroshenko, N. N. Kudryaster, and V. V. Smetanin. Quenching mechanisms for electronically excited species in partially dissociated air. *High Energy Chem.*, 26:227–230, 1992.

[176] D. Husian and A. N. Young. Kinetic investigation of ground state carbon atoms $c(2^3p_j)$. *J. Chem. Soc., Faraday Trans. 2*, 71:525–531, 1975.

[177] W. B. Demore et al. Chemical kinetics and photochemical data for use in stratospheric modeling evaluation number 12. *JPL Publication*, 97:1–266, 1997.

[178] K. Niemi et al. The role of helium metastables states in radio-frequency driven helium-oxygen atmospheric pressure plasma hets: measurement and numerical simulation. *Plasma Sources Sci. Technol.*, 20:055005, 2011.

[179] D. C. Lorents. The physics of electron beam excited rare gases at high densities. *Physica C*, 82:19–26, 1976.

[180] C. A. Brau. *Rare gas halide lasers in Excimer lasers*. Springer-Verlag, 1979.

[181] J. T. Herron and D. S. Green. Chemical Kinetics Database and Predictive Schemes for Nonthermal Humid Air Plasma Chemistry. Part II Neutral Species Reactions. *Plasma Chem. Plasma Proc.*, 21:459–481, 2001.